Strain adaption in epitaxial Fe-Rh nanostructures

Dehnungsanpassung in epitaktischen Fe-Rh Nanostrukturen
Zur Erlangung des akademischen Grades Doktor-Ingenieur (Dr.-Ing.)
genehmigte Dissertation von Dipl.-Ing. Ralf Witte aus Ludwigsburg
Tag der Einreichung: 20. Juni 2016, Tag der Prüfung: 27. Juli 2016
Darmstadt 2016 — D 17

1. Gutachten: Prof. Dr.-Ing. Horst Hahn
2. Gutachten: Prof. Dr. Heiko Wende

TECHNISCHE UNIVERSITÄT DARMSTADT

Fachbereich
Material- und Geowissenschaften
Gemeinschaftslabor Nanomaterialien

Strain adaption in epitaxial Fe-Rh nanostructures
Dehnungsanpassung in epitaktischen Fe-Rh Nanostrukturen

Genehmigte Dissertation von Dipl.-Ing. Ralf Witte aus Ludwigsburg

1. Gutachten: Prof. Dr.-Ing. Horst Hahn
2. Gutachten: Prof. Dr. Heiko Wende

Tag der Einreichung: 20. Juni 2016
Tag der Prüfung: 27. Juli 2016

Darmstadt 2016 — D 17

Bitte zitieren Sie dieses Dokument als:
URN: urn:nbn:de:tuda-tuprints-57951
URL: http://tuprints.ulb.tu-darmstadt.de/5795

Dieses Dokument wird bereitgestellt von tuprints,
E-Publishing-Service der TU Darmstadt
http://tuprints.ulb.tu-darmstadt.de
tuprints@ulb.tu-darmstadt.de

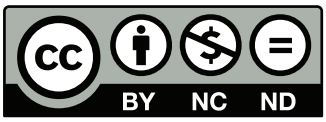

Die Veröffentlichung steht unter folgender Creative Commons Lizenz:
Namensnennung – Keine kommerzielle Nutzung – Keine Bearbeitung 4.0 International
http://creativecommons.org/licenses/by-nc-nd/4.0/

Erklärung zur Dissertation

Hiermit versichere ich, die vorliegende Dissertation ohne Hilfe Dritter nur mit den angegebenen Quellen und Hilfsmitteln angefertigt zu haben. Alle Stellen, die aus Quellen entnommen wurden, sind als solche kenntlich gemacht. Diese Arbeit hat in gleicher oder ähnlicher Form noch keiner Prüfungsbehörde vorgelegen.

Darmstadt, den 20. Juni 2016

(Ralf Witte)

Abstract / Zusammenfassung

Abstract

Nanostructured magnetic materials continuously attract tremendous interest in both science and technology and their applications are found, for example, in the area of magnetic data storage. One versatile, and technologically mature, route to design and tailor modern magnetic materials is the growth of thin films as epitaxial heterostructures. The precise control of the associated epitaxial strain, in other words an elastic deformation, can profoundly alter the intrinsic magnetic properties of the coherently grown layers. However, going beyond the elastic regime, strain may also create lattice instabilities, reshaping the material's energy landscape, and possibly promoting novel, metastable phases and/or the spontaneous formation of magnetic nanostructures.

In this thesis, the iron-rhodium (Fe-Rh) binary alloy system is identified as a promising candidate for epitaxial strain-tailoring due to the presence of both, fragile and competing magnetic exchange interactions and inherent lattice instabilities. The close entanglement of these properties may lead to unprecedented strain adaption mechanisms accompanied by beneficially modified magnetic characteristics.

Indeed, in the course of this work, it was discovered that epitaxial layers of chemically disordered equiatomic FeRh grown on tungsten (W) buffer layers show a novel strain adaption behavior. Essentially, the strain triggers a lattice instability, which in turn drives the film from a tetragonal into an orthorhombic structure, featuring a 90° domain pattern, reminiscent of adaptive martensites. The structural changes have a profound impact on magnetism, suppressing ferromagnetic (FM) order and eventually resulting in a spin glass (SG) configuration at low temperatures. A study of the thickness dependence evidenced a gradual evolution from a tetragonally distorted lattice to the adaptive orthorhombic structure in films with increasing thickness, representing a coherent release of epitaxial stress and hence decrease of the system's elastic energy. Then, the compositional limit of the lattice instability was explored. Beyond a Fe content of 72 at.-% it is no longer possible to accommodate the strain by adoption of the orthorhombic phase. Instead a fully relaxed, body centered cubic (bcc) phase is found, which shows its expected FM ground state.

The influence of the epitaxial misfit was investigated by using tungsten-vanadium (W-V) alloy buffer layers. Here, a distinct dependence of the final structure on the growth temperature was revealed. FeRh films grown at ambient temperatures on buffer layers with decreasing mismatch (compared to pure W) develop a structure similar to the orthorhombic phase, which features an extra directional tilting in order to match to the W-V lattice constant. However, at elevated growth temperatures the films spontaneously segregate on the lateral scale, into two different phases: the orthorhombic and a partially ordered body centered tetragonal (bct) phase, reducing the elastic energy in each individual phase. Most importantly, these two phases are in different magnetic states, the first being paramagnetic (PM) and the second FM. The resulting nano-scale arrangement of the PM and FM phase can be described as a strain-induced self-assembled magnetic nanostructure. Hence, the newly found lattice instability is directly placed into an application related context, potentially allowing the *bottom-up* down-scaling of the magnetic bit size in FeRh based data storage media.

The findings of this work extend the concepts of strain-induced or strain-engineered magnetic nanostructures from the purely nano-twinned structures to a two-phase-adaption mechanism. On a more general note, the presented studies highlight the fascinating properties of hitherto unknown metastable phases in the Fe-Rh system, which may motivate similar studies in related binary or ternary alloy systems, likewise offering advantageous prerequisites.

Zusammenfassung

Nanostrukturierte magnetische Materialien sind von großem Interesse sowohl für die wissenschaftliche Forschung als auch für die technologische Entwicklung von neuen magnetischen Datenspeichern. Eine vielseitige und technologisch ausgereifte Methode zum Maßschneidern moderner magnetischer Funktionsmaterialien, ist die Herstellung von Dünnschichten in Form von epitaktischen Heterostrukturen. Durch die präzise Kontrolle der epitaktischen Dehnung, also der elastischen Deformation in den Schichten, können die intrinsischen magnetischen Eigenschaften der kohärent gewachsenen Schicht direkt beeinflusst werden. Jenseits des elastischen Verhaltens kann die Deformation eine Instabilität des Kristallgitters verursachen und damit die Energielandschaft des Materials verändern. Dies kann zum Auftreten von neuen, metastabilen Phasen führen und/oder die spontane Bildung von magnetischen Nanostrukturen verursachen.

In der vorliegenden Dissertation wird das binäre Legierungssystem Eisen-Rhodium (Fe-Rh) untersucht und als vielversprechendes Materialsystem für das Maßschneidern der magnetischen Eigenschaften mittels epitaktischer Dehnung vorgestellt. Das

System weist zugleich konkurrierende magnetische Austauschwechselwirkungen und inhärente Gitterinstabilitäten auf. Das gemeinsame Auftreten dieser beiden Eigenschaften ermöglicht neuartige Mechanismen der Dehnungsanpassung, die gleichzeitig das magnetische Materialverhalten vorteilhaft beeinflussen können.

In dieser Arbeit wird ein bisher so nicht beschriebenes Dehnungsanpassungsverhalten in FeRh Legierung beobachtet, welches durch epitaktisches Aufwachsen von chemisch ungeordneten FeRh Schichten auf Wolfram (W) Zwischenschichten ausgelöst wird. Die epitaktische Dehnung verursacht eine Gitterinstabilität, so dass sich die tetragonal verzerrte Struktur der Schicht in eine orthorhombische umwandelt. Die resultierende Mikrostruktur der Schicht besteht aus in 90° zueinander orientierten kristallinen Domänen, vergleichbar den adaptiven Martensit Strukturen. Interessanterweise wird durch die Strukturänderung die ferromagnetische (FM) Ordnung des Materials zu Gunsten einer bei tiefen Temperaturen auftretenden Spin Glas (SG) Phase vollständig unterdrückt. Die Untersuchung der Schichtdickenabhängigkeit des Anpassungsmechanismus zeigt eine kohärente, schrittweise Veränderung von der tetragonal verzerrten Struktur in dünnen, hinzu der vollausgeprägten orthorhombischen Martensit Struktur in dickeren Schichten. Durch diese Vorgänge können die Spannungen im Material relaxieren und die gespeicherte elastische Energie kann verringert werden. Die chemische Zusammensetzung der Fe-Rh Legierungen beeinflusst das Auftreten der Gitterinstabilität, jenseits eines Fe Gehalts von 72 at.-% kann die epitaktische Dehnung nicht mehr durch die Bildung der orthorhombischen Phase aufgenommen werden. Stattdessen wird eine kubisch raumzentrierte (krz) Phase gebildet, die das erwartete FM Verhalten zeigt.

Der Einfluss der epitaktischen Gitterfehlanpassung wurde mit Hilfe von Wolfram-Vanadium (W-V) Zwischenschichten untersucht. Dabei wurde eine ausgeprägte Abhängigkeit zwischen der gebildeten Struktur und der Wachstumstemperatur beobachtet. FeRh Filme, die bei Raumtemperatur auf Zwischenschichten mit sukzessiv abnehmender Fehlanpassung (im Vergleich zu reinem W) abgeschieden werden, wachsen in der orthorhombischen Struktur auf. Diese weist allerdings eine zusätzliche richtungsabhängige Verkippung auf, die die Anpassung an die W-V Gitterkonstante letztendlich ermöglicht. Bei erhöhten Wachstumstemperaturen findet jedoch spontan eine laterale Separation in zwei unterschiedliche Phasen statt: Die orthorhombische Phase und eine tetragonal raumzentrierte Phase mit partieller chemischer Ordnung. Durch diese Aufspaltung kann das System die elastische Energie in jeder einzelnen Phase reduzieren. Interessanterweise liegen die beiden strukturell unterschiedlichen Phasen auch in verschiedenen magnetischen Zuständen vor: Die erste verhält sich paramagnetisch (PM), während die zweite FM ist. Diese nano-skalige Anordnung der PM und FM Phase kann als eine dehnungs-induzierte magnetische Nanostruktur beschrieben werden, welche sich spontan durch Selbstassemblierung bildet. Dieser

Mechanismus erlaubt es, die neuentdeckte Gitterinstabilität unmittelbar in einen anwendungsorientierten Zusammenhang zu stellen, da auf diese Weise die Dimension der magnetischen Bits in FeRh basierten magnetischen Datenspeichern reduziert werden kann.

Insgesamt erweitern die Ergebnisse dieser Dissertation die bekannten Konzepte zur dehnungs-induzierten und -kontrollierten Bildung von magnetischen Nanostrukturen von den rein nano-verzwillingten Strukturen zu dem hier beschriebenen zweiphasigen System. Die faszinierenden Eigenschaften von bis dato unbekannten metastabilen Phasen im Fe-Rh System weisen den Weg, vergleichbare Untersuchungen in anderen vielversprechenden binären oder ternären Legierungssystemen durchzuführen.

Index

Contents

List of Figures

List of Tables

Definition of acronyms and symbols

Acronyms

AFM Atomic Force Microscopy

AF antiferromagnetic

bcc body centered cubic

bct body centered tetragonal

CPA Coherent Potential Approximation

CEMS Conversion Electron Mössbauer Spectroscopy

DFT Density Functional Theory

DOS Density of States

e-beam electron beam

EDX Energy-Dispersive X-ray Spectroscopy

FC Field Cooling

fcc face centered cubic

FFT Fast Fourier Transform

FIB Focused Ion Beam

FM ferromagnetic

FWHM Full Width at Half Maximum

hcp hexagonal close packed

HRTEM High-Resolution Transmission Electron Microscopy

HRXRD High-Resolution X-ray Diffraction

INT Institute of Nanotechnology

KIT Karlsruhe Institute of Technology

KKR Korringa-Kohn-Rostoker

LEED Low Energy Electron Diffraction

MBE Molecular Beam Epitaxy

MFA Mean Field Approximation

ML monolayer

PM paramagnetic

QCM Quartz Crystal Microbalance

RBS Rutherford Backscattering Spectroscopy

RHEED Reflection High Energy Electron Diffraction

RMS Root Mean Square

RSM Reciprocal Space Map

RT room temperature

SEM Scanning Electron Microscopy

SG spin glass

SQS Special Quasirandom Structure

SQUID Superconductive Quantum Interference Device

STEM Scanning Transmission Electron Microscopy

STM Scanning Tunneling Microscopy

TMP Turbo Molecular Pump

u.c. unit cell

UHV Ultra-High Vacuum

XRD X-ray diffraction

XRR X-ray Reflectometry

ZFC Zero-Field Cooling

Symbols

a, c	crystal lattice constants of a cubic or tetragonal Fe-Rh alloy
a', b', c'	crystal lattice constants of an orthorhombic Fe-Rh alloy
a_{WV}, c_{WV}	crystal lattice constants of a cubic or tetragonal W or W-V alloy
B_{HF}	magnetic hyperfine field
χ	eucentric tilt angle
CS	center shift
f	epitaxial misfit
ϵ	strain
EFG	electric field gradient
E_{F}	Fermi energy
γ_{IF}	interface energy
h, k, l	Miller indices
δ	isomer shift
J	exchange interaction parameter
J_{ij}	pair exchange interaction parameter
ΔE_{Q}	quadrupole splitting
F	structure factor
G	shear modulus
H	magnetic field
Γ	Lorentzian line width
m_{tot}	total magnetic moment
M	magnetization

μ	magnetic moment
μ_0	vacuum permeability
μ_B	Bohr magneton
ν	Poisson's ratio
ω	incident angle
ϕ	azimuth angle
p_{work}	working pressure
σ	Gaussian standard deviation
t	thickness
T	temperature
θ	Bragg angle
T_C	Curie temperature
T_f	spin freezing temperature
U_{el}	elastic energy
V_{zz}	principal component of the electric field gradient (EFG)
x	Fe content in Fe_xRh_{1-x} alloys
y	4c Wyckoff parameter of the $Cmcm$ phase
z	V content in $W_{1-z}V_z$ alloys

1 Introduction

1.1 Motivation

The Fe-Rh binary alloy system started to attract scientific interest in 1938 after Fallots [1, 2] discovery of a first order magnetic transition from an antiferromagnetic (AF) ground state to ferromagnetic (FM) order close to room temperature, observed in an equiatomic intermetallic alloy with ordered CsCl structure (B2 Phase). Since then, this material and especially the AF-FM transition has been studied for fundamental scientific aspects but also in various application contexts. Proposed applications range from electric field control of magnetic order [3], to heat assisted magnetic recording devices [4–6] or a room temperature AF memristor [7, 8]. Recently, FeRh has been considered as one of the best magnetocaloric materials [9–11].

However, since the AF-FM transition is only observed in a narrow composition range in the B2-ordered alloys, the disordered and metastable phases in the remaining parts of the phase diagram have not been studied in comparable depth. Yet, these materials offer interesting fundamental properties which may, if beneficially deployed, lead to functional applications. This is briefly motivated in the following paragraphs on the basis of an analysis of the relevant literature.

The existing experimental studies, which deal with the disordered and metastable Fe-Rh phases, are based nearly exclusively on the synthesis of bulk specimens using bulk methods such as rapid quenching [12, 13] or mechanical deformation induced disordering by e.g. ball-milling [14–17]. However, there are some examples showing that the application of thin film deposition techniques may allow to stabilize metastable phases [18] in composition ranges for which rapid quenching techniques fail due to the high temperatures of the structural transitions [12]. Recently, low temperature deposition of FeRh on single crystalline substrates was even found to result in epitaxial (single crystalline), chemically disordered films featuring a metastable structure [19, 20].

The epitaxial growth of thin films of the disordered Fe-Rh alloys is an effective tool to control an important intrinsic parameter of the material, namely its strain-state. This is achieved by using different single crystalline buffer layers which determine the in-plane lattice constants of the coherently overgrown functional film

and thereby define its strain-state. The profound implications of this approach may be illustrated by findings in the related Fe-Pd system: Here it was shown that, owing to a martensitic transformation from a face centered cubic (fcc) to a body centered cubic (bcc) structure, the epitaxial strain can be varied in a large range all along the Bain transformation-path [21], resulting in an effective strain-control of the magnetic properties [22]. Moreover, straining the material beyond the stable lattice constant range leads to the formation of strain-induced nano-twinned structures. This was proposed as a novel synthesis route to self-assembled magnetic nanostructures [23]. Such fascinating strain-induced phenomena may be also expected in the Fe-Rh system, a claim supported by the presence of several types of lattice instabilities and martensitic transformations in different Fe-Rh alloys [13, 24–28].

The magnetic properties of the Fe-Rh alloys are governed by the presence of competing AF and FM exchange interactions, which are the driving force behind the AF-FM transition in B2-FeRh [29, 30], but which are also responsible for the frustrated magnetic configurations in some of the disordered alloys [14–17].

The sensitivity of these competing magnetic exchange interactions to the local crystallographic geometry and interatomic distances [29] may give rise to large variations of the magnetic properties along with the strain-controlled structural changes. In other words, the inherent fragility of the magnetic exchange coupling entangled with possible strain-induced structural transitions, precisely engineered by mismatched heteroepitaxy, may open new pathways to tailor and promote yet unknown magneto-structural transitions in Fe-Rh alloys.

1.2 Objective, scope and outline of this thesis

Objective

The research performed within this doctoral work and presented in the dissertation at hand, aims at identifying, describing and understanding novel and potentially application relevant phenomena related to magneto-structural instabilities in Fe-Rh alloys, by exploring the parameter triangle of strain, composition and chemical order in epitaxial Fe-Rh thin films.

Scope

Epitaxial Fe_xRh_{1-x} thin films were deposited on different metallic buffer layers of W and W-V alloys, prepared by magnetron-sputtering on MgO(001) single crystalline substrates, enabling a continuous variation of the desired in-plane lattice parameter.

The Fe_xRh_{1-x} films were deposited in a dedicated Molecular Beam Epitaxy (MBE) chamber (designed within the course of this project) equipped with Mini-electron beam (e-beam) evaporators, which allowed for the deposition of ^{57}Fe enriched films and consequently enabled an investigation with Mössbauer spectroscopy.

Initially, a strain-induced lattice instability was observed in equiatomic, chemically disordered FeRh films grown on W buffer layers, leading to the growth of an adaptive orthorhombic structure. The structural changes were accompanied by a distinct suppression of FM order, eventually resulting in a highly frustrated and disordered magnetic ground state at low temperatures. This strain-induced magneto-structural transition was unraveled in a combined study using first principle calculations, extensive diffraction and local spectroscopy experiments. In the following the lattice instability was further studied by investigating the effects of the epitaxial interface and the composition on the final structures.

Finally, the influence of the in-plane lattice parameters was studied by means of a series of FeRh films grown on W-V buffer layers. These experiments showed a distinct dependency on the growth temperature. Therefore they were carried out at ambient and elevated temperature. The latter series of samples provided evidence for the formation of an epitaxial strain-induced and strain-controlled self-assembled magnetic nanostructure.

Outline

Chapter 2 introduces the scientific background of the study. The necessary terms, definitions and concepts of strained epitaxial growth are presented and an introduction to the Fe-Rh binary alloy system, as well as a review of the relevant literature concerning the properties and synthesis of Fe-Rh alloys is given.

Chapter 3 provides information about the applied characterization methods and experimental details. In the second part of this chapter the deposition techniques used for the growth of the bilayer structures are presented. Moreover it contains experimental results describing the structure and quality of the W and W-V buffer layers, in order to exclusively focus on the properties of the Fe-Rh layers in the following chapters.

Chapter 4 presents the discovery of the strain-induced lattice instability in FeRh/W bilayers. The understanding of this phenomenon constitutes the basis on which the subsequent experiments were performed.

In Chap. 5 the variation of the structure as a function of FeRh film thickness is investigated. The observed continuous evolution allowed to draw further conclusions on the strain-adaption character of the observed structural transition.

Chapter 6 discusses the results of a study of the composition dependence, which proved the large compositional occurrence range of the lattice instability and relates the observed behavior to the equilibrium phase diagram.

The influence of the predetermined in-plane lattice parameter is studied in depth in Chap. 7, which unraveled a distinct metastability of the structures leading to a strong impact of the growth temperature. First equiatomic FeRh films grown at ambient temperatures on W-V buffer layers are presented. Then films deposited at elevated growth temperatures are discussed, which eventually present a novel strain-adaption mechanism involving strain-induced phase-separation into two, magnetically different, phases.

The results and findings of the presented research are concluded in Chap. 8 and promising directions for future research are proposed.

2 Scientific Background

In the following the scientific background of this thesis is introduced. At first the general terms and definitions necessary to describe strained epitaxial growth are provided. Then it is commented on concepts to achieve strained film growth and epitaxial strain-induced nanostructures. In the second section the Fe-Rh material system is introduced and the published literature, relevant to the findings of the present thesis, are referenced and discussed. Finally a brief rationale is given for the initial choice of chemically disordered Fe-Rh for studies in form of strained epitaxial thin films.

2.1 Strain-tailoring of magnetic thin films

Strain-tailoring in general aims at controlling the functional properties of a material by its strain state. Two obvious requirements have to be fulfilled for that purpose:

Firstly, a well defined strain state ϵ needs to be created in the material. Fabrication of epitaxial heterostructures or bilayers is widely considered as a versatile approach to achieve highly controllable strain values. Here the crystalline lattice of a functional material is coherently grown onto a single crystalline substrate or buffer layer. When the two different materials have different lattice constants so the lattice of the overgrown functional layer gets deformed or strained due to the mismatch between the two crystal lattices. The capability of a material to accommodate high epitaxial strain values will be referred to as strain-ability.

Secondly, the functional property to be tailored must be responsive to the variation of interatomic distances and the distortion of the lattice, hence a certain strain-sensitivity mechanism must be present. In the case of magnetic properties, various mechanisms exist, ranging from the interatomic distance or atomic volume dependence of the exchange interaction parameter (J), expressed in the well-known Bethe-Slater curve [31], over e.g. angular dependencies observed in more directional coupling magnetic materials, to the changes expected when the symmetry of a crystal lattice is altered. Among the characteristic magnetic parameters that have been shown to be susceptible to a change of the strain state are

the magnetic moment (μ) [22, 32, 33], the Curie temperature (T_C) [22, 33] and the magneto-crystalline anisotropy [22, 34–36][1].

2.1.1 Strained heteroepitaxy: Definition of terms

The following considerations loosely follow the textbook *Epitaxy Physical Principles and Technical Implementation* [37].

An important quantity in the context of strained heteroepitaxy is the epitaxial misfit (f) between the bulk (in-plane) lattice constants a_S of the substrate and $a_{L,0}$ of the layer, which is commonly defined as:

$$f = \frac{a_S - a_{L,0}}{a_{L,0}}. \tag{2.1}$$

The index 0 indicates that the bulk, unstrained lattice constant is meant[2]. Hence, a positive (negative) f refers to a situation where the film lattice constant is smaller (larger) than the one of the underlying substrate. This value basically provides no information about the situation in the final heterostructures, which is rather described by the epitaxial strain ϵ, given by:

$$\epsilon = \frac{a_L - a_{L,0}}{a_{L,0}}. \tag{2.2}$$

Here the actual lattice constant of the layer a_L (in the heterostructure) is compared to its bulk value. From these definitions it is clear that in the case where the crystalline lattice of the layer perfectly follows the substrate lattice, thus $a_L = a_S$, epitaxial strain and misfit are identical. Under such conditions epitaxial growth is called *fully strained* or *pseudomorphic*. In this scenario the control over the strain state and thus the related functional property is the most straightforward.

However, growing a material under considerable strain leads to a significant contribution of the elastic energy (U_{el}) to the total energy of the film (per area). U_{el} can be expressed, assuming a semi-infinite substrate and an epitaxial layer of thickness (t) with its elastic constants, the Poisson's ratio (ν) and shear modulus (G), as follows [38, 39]:

[1] The given literature citations do not display a comprehensive choice but are rather meant as examples.

[2] For a situation where the substrate is much thicker than the layer the index 0 is omitted in the case of the substrate lattice constant, as no change of the latter is expected.

$$U_{\mathrm{el}} = 2\,G\,\frac{1+\nu}{1-\nu}\,t\,\epsilon^2. \tag{2.3}$$

Here the strain ϵ is simplified to be identical in the two perpendicular interfacial directions. Hence, U_{el} scales linearly with the thickness t and quadratic with the strain (ϵ). In case of fully strained grown body centered cubic (bcc) Fe on a W(100) surface for example, with about +10% epitaxial misfit, this energetic contribution is in the range of about 200 meV/atom [40]. Therefore, the elastic energy term U_{el} naturally becomes increasingly unfavorable with cumulative thickness. Consequently, a critical thickness can be defined [38], above which the introduction of misfit dislocations into the lattice, despite their respective stress field and local distortions, which results of course also in an increase of the total energy, is more favorable than the situation of the highly strained lattice. During the subsequent growth, misfit dislocations are introduced into the film structure in a so-called dislocation network with a regular spacing, depending on f and the actual strain ϵ in the layer. Analytic expressions have been derived for the resulting critical thickness, taking into account the defect energy contribution originating from the introduced dislocation networks [38, 39], which are not presented here. However, this critical thickness may range from few monolayers (MLs), as in the case of Fe on W(100) [41] to as much as several nm.

If the strain in the film is completely relaxed via the introduction of misfit dislocations, the opposite extreme $\epsilon = 0$ can be reached, which is referred to as *fully relaxed* growth. From the point of view of strain-tailoring it is obvious that the latter situation would not allow to influence the functional property at all, as it would be entirely defined by the bulk-like structure of the film. The objective is thus to grow films in a fully strained way, or at least strained enough to affect the functional property of interest.

Several operational approaches can be derived from the above considerations, such as constraining the grown heterostructures to ultra-thin films below the critical thickness or the application of material combinations with rather small misfits, but with a high sensitivity of the functional property to the strain, such that already small strains have significant impact as for example in semiconductors [42] or some magnetic [32, 43] or supraconducting [44] oxides.

2.1.2 Highly strained films: Lattice instabilities and adaptive nanostructures

However, the above described concepts usually fail if one is aiming at comparably thick films >10 nm and at the same time large strains are required for achieving an appreciable impact on the functional property. Therefore, an innovative approach

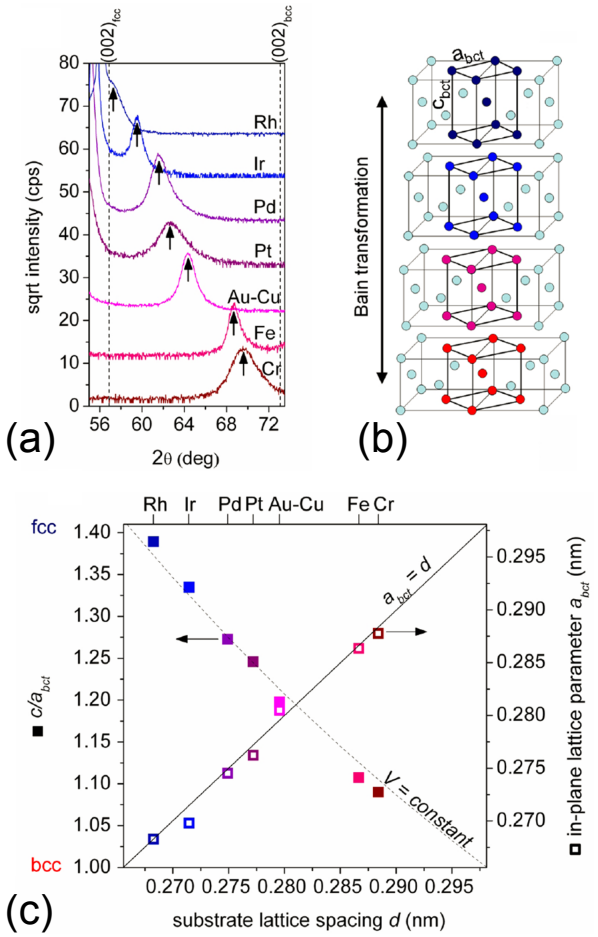

Figure 2.1.: Structural properties of strained $Fe_{70}Pd_{30}$ thin films. (a) XRD patterns. (b) Visualization of the Bain transformation. (c) In-plane lattice parameter and c/a ratio of the strained $Fe_{70}Pd_{30}$ thin films. (*Reprinted with permission from* [22]. ©2009, American Physical Society).

has been proposed and reported, in order to solve the shortcomings of the existing methods going beyond traditional strain-relaxation schemes, eventually resulting in nanostructured materials.

This approach utilizes the last parameter in equation Eq. 2.3 that has not been considered yet, namely the elastic properties of the material. Based on the work of van der Merwe [39], Buschbeck *et al.* have recently shown that the use of soft materials, or materials with intrinsic lattice instabilities may be beneficially applied to achieve highly strained films [22]. Typical materials having lattice instabilities are martensite forming materials. In their work they used the magnetic shape memory alloy $Fe_{70}Pd_{30}$, which possess a martensitic instability between a face centered cubic (fcc) phase and the bcc phase. The transformation path between these two structures is the well-known Bain transformation or Bain path [21].

In order to realize different strain states along the Bain path, $Fe_{70}Pd_{30}$ thin films were deposited on several different metallic buffer layers, having each a different lattice constant. In that way strained structures all along the Bain path were synthesized. Fig. 2.1 presents the results of that study, featuring the structural investigation with X-ray diffraction (XRD). For illustration the Bain transformation is also shown in (b). It is basically represented by an in-plane expansion of the lattice, while at the same time the out-of-plane lattice parameter shrinks. This is evidenced in part (c) of Fig. 2.1, where the evolution of the lattice parameters is shown to follow the perfect behavior corresponding to a constant volume along the transition.

Besides proving the feasibility of the concept, it was also shown that the structural transition results in a significant variation of the magnetic properties and that the relatively flat energy-landscape, characteristic of a martensitic instability, is responsible for the structural behavior. This is depicted in Fig. 2.2(a), where the energy-landscape is presented as a function of c/a. Moreover, the magnetic anisotropy constants (K) are drastically changing along the path, as well as the T_C which varies by 25%.

In an extension of the above described study, Kauffmann-Weiss *et al.* [23] have shown that $Fe_{70}Pd_{30}$ thin films can be even strained beyond the Bain path, thus beyond their stable lattice constant regime. They showed that in these samples the $Fe_{70}Pd_{30}$ structure relaxes in a so-called adaptive nano-twinned structure, hence the excessive misfit is stored in a twin-structure on the nanoscale. This formation of a self-organized nanostructure effectively reduces the accumulated elastic energy U_{el} at the cost of the introduced twin-boundary energy. The occurrence of such a behavior is intimately linked to a relatively low twin boundary energy compared to the defect energy of competing relaxation mechanisms as e.g. misfit dislocations. This has been demonstrated by Density Functional Theory (DFT) calculations, which identify a metastable energetic minimum in relaxed $Fe_{70}Pd_{30}$ structures at a c/a ratio[3] of ≈ 1.1, related to the spontaneous twinning of the structure in the

[3] Here the definition refers to fcc as ground state, hence $c/a = 1$ for fcc.

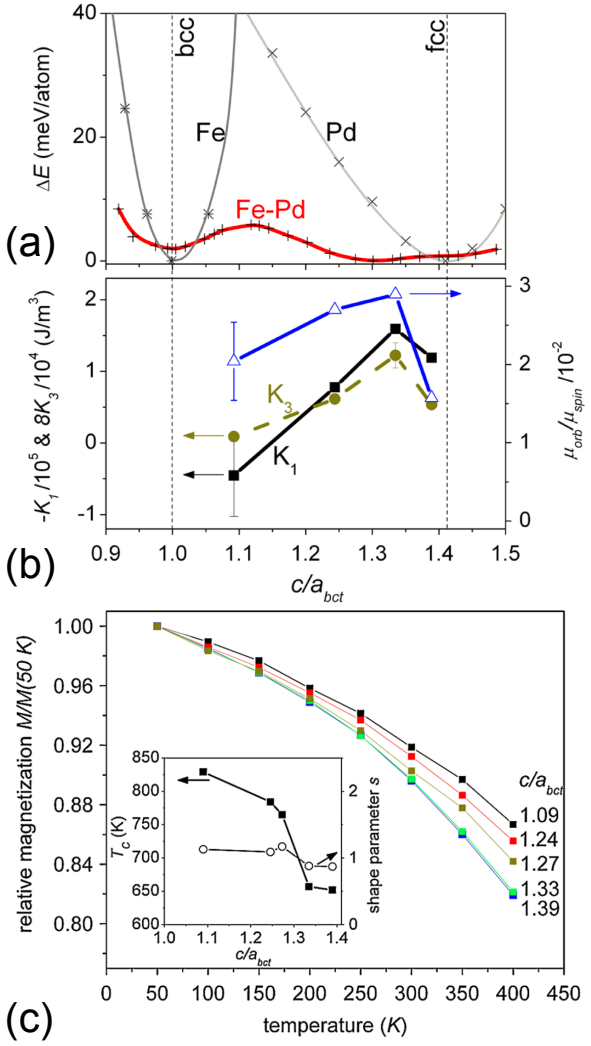

Figure 2.2.: Energy-landscape and magnetic properties of strained $Fe_{70}Pd_{30}$ thin films. (a) Energy-landscape along the Bain path. (b) Magneto-crystalline anisotropy constants. (c) T_C change along the Bain path. (*Reprinted with permission from* [22]. ©2009, American Physical Society).

simulation cell. This is illustrated in Fig. 2.3 showing the (a) c/a variation of the experimental thin films and (b) the calculated energy-landscape for the ideal and relaxed structures, while the inset displays the obtained twin structure in a top-view of the thin film geometry. The study also provides experimental evidence for the twinning predicted by theory, which is not discussed here.

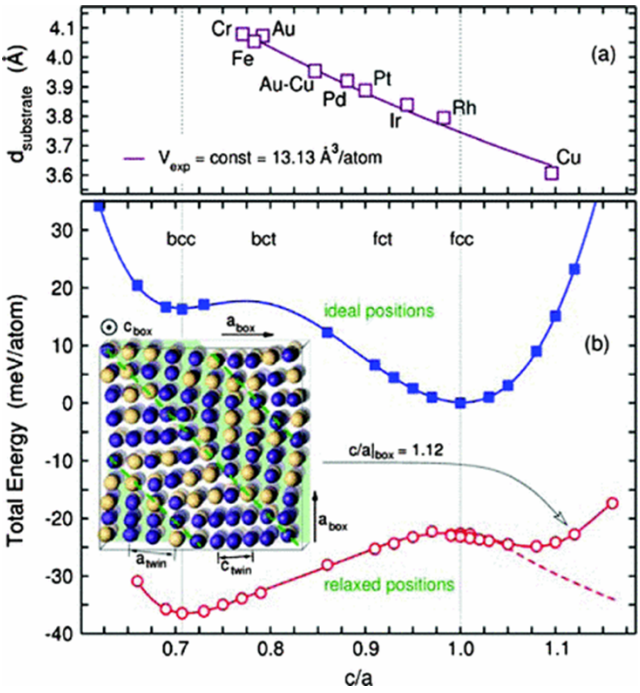

Figure 2.3.: Energy-landscape strained and nano-twinned $Fe_{70}Pd_{30}$ thin films. (a) Experimental lattice constants of the $Fe_{70}Pd_{30}$ thin films. (b) Total energy of the structures as a function of their c/a ratio for the ideal lattice positions and for a structurally relaxed configuration. The latter leads to a metastable state at $c/a > 1$ due to a spontaneous twinning of the structure, which is illustrated by the atomic arrangement in the super cell presented in the inset. (*Reprinted with permission from* [23]. ©2011, American Physical Society).

Interestingly, the observed nano-structured twin pattern resembles those observed in the magnetic shape memory alloy Ni_2MnGa, which is referred to as an adaptive martensite structure [45, 46]. Here the adaption happens at the interface between the austenite and martensite phase, the so-called habit plane, which in a way represents

also an epitaxial interface. In the case of the strained films the substrate-film interface may be thus described as an artificial habit plane.

Furthermore, the authors argue that their approach may be used to obtain novel self-organized magnetic nanostructures, hence strain-tailoring may not only lead to a certain desired variation of a functional property but it may also enable to create *bottom-up* nanostructures. This concept will be referred to later in this thesis within Chaps. 4 and 7.

An interesting alternative approach to the use of different buffer layers, introducing large strains into an epitaxial thin film, was proposed by Arabi-Hashemi *et al.* [47], who irradiated epitaxial Fe_7Pd_3 films with high energy ions. The structural defects created by ion bombardment induce large local stress fields, which in turns trigger the fcc→bcc martensite transformation. Tailoring of the structural state all along the transformation path was realized by adjusting the irradiation dose accordingly.

Although the following chapters of this thesis focus exclusively on the properties of epitaxial Fe-Rh films, which are strained by applying the first concept of buffer layer assisted growth. The ion irradiation approach was mentioned as it lead to a follow-up work and joint publication [48] with a contribution of the author of this thesis. It was shown with spectroscopic methods, namely Conversion Electron Mössbauer Spectroscopy (CEMS), that ion-irradiation induced chemical disorder can be ruled out as possible cause for the transformation, in support of the local stress field explanation.

2.2 The Fe-Rh binary alloy system: From equilibrium structures to lattice instabilities

The previous section has illustrated the need for a material system, which displays both strain-sensitivity of the functional property, and the occurrence of lattice instabilities, in other words featuring sufficient strain-ability, for achieving large strain-induced effects in films beyond the ML regime. In the following the Fe-Rh alloy system will be introduced and its suitability for generation of considerable strain-induced effects and tailoring of its magnetic properties will be reviewed.

2.2.1 Fe-Rh binary alloy phase diagram

The Fe-Rh binary phase diagram is depicted in Fig. 2.4. Close to the elemental endpoints the alloys form a solid solution or chemically disordered alloy with the crystal structure of the respective main component. The Fe-rich alloys crystallize in a disordered bcc structure, the A2 or α phase, while the Rh-rich alloys form a fcc structure referred to as A1 or γ phase.

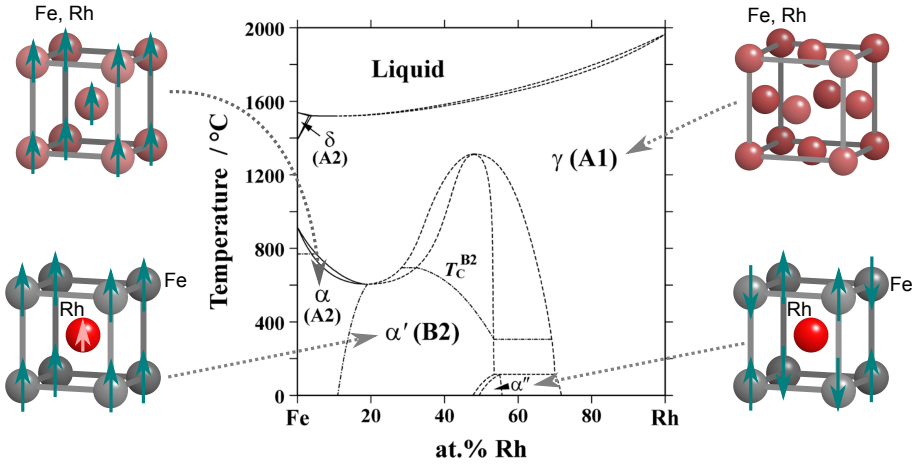

Figure 2.4.: Fe-Rh binary alloy phase diagram. The atomic ball models illustrate the different crystallographic structures, with the arrows indicating the spin configuration of the magnetic phases. (*Reprinted with permission from* [49]. ©2011, Springer).

The third structural phase, the chemically ordered B2 structure can be described as a bcc lattice, where the body centered sites and the corner sites are occupied with one kind of element respectively. This ordered arrangement is also known as CsCl structure and it is depicted as atomic ball model in the figure. Two structural peculiarities are especially interesting here, before the magnetic ones are discussed. First the broad concentration range of the B2-phase, which reaches from the equiatomic composition down to about 15 at.-% Rh, points towards a high ordering tendency of the alloy, despite the fact that the non-equiatomic B2 structures must include a high concentration of structural defects, namely anti-site defects [13]. However, the purely disordered A2 phase is only observed at rather high Fe concentrations, while the order-disorder transition from B2 to A2 is strongly suppressed and instead the A1 phase forms at higher temperatures.

The three equilibrium phases behave quite differently with respect to their magnetic properties. The A2 phase is ferromagnetic (FM), just as elemental Fe, while the A1 phase is described as paramagnetic (PM), with a possible low temperature spin glass (SG) phase, which will be discussed more extensively below.

However, the magnetic characteristics for which the Fe-Rh system became known, was reported in 1938 by Fallot [1, 2] and since then it has motivated various fundamental and applied studies. The B2 phase close to the equiatomic composition, in a narrow compositional range shows a magnetic phase transition from a low

temperature antiferromagnetic (AF) to a high temperature FM phase. The magnetic transition happens close to ambient temperature and is accompanied by only a small increase in unit cell volume. The antiferromagnetically ordered B2 phase, also called the α'' is very sensitive to the composition and the degree of chemical ordering. The presence of a certain fraction of antisite defects, 4% is sufficient, to entirely suppress the subtle AF order. For that reason the B2 phase is FM in the major part of its stable phase field, which is also referred to as α'-phase.

2.2.2 Competing magnetic exchange interactions and the AF-FM transition

The AF-FM transition in near-equiatomic alloys results from the competition of opposing magnetic exchange interactions, favoring one or the other kind of magnetic ordering at the given temperature. This has been discussed in two recent theoretical studies by Kudrnovsky *et al.* [29] and by Sandratskii and Mavropoulos [30], using first principle calculations.

Figure 2.5 shows the calculated, interatomic distance dependent value of the magnetic exchange interactions $J^{Q,Q'}$ (obtained in a Heisenberg model [50]) between different pairs Q, Q'=Fe, Rh, for the (a) B2-ordered phase and for the (b) disordered A2 FeRh structure [29]. First the results for the B2 structure are discussed, which show two characteristic features important for the occurrence of the AF-FM transition. The $J^{\mathrm{Fe,Fe}}$ are small and more importantly those which have a significant value are negative, hence indicating AF coupling between the Fe pairs, e.g. the Fe-Fe along the [100] direction ($d/a = 1$) as well as along the [111] (body diagonal, $d/a = \sqrt{3}$, green arrows indicate AF coupling between Fe-Fe pairs), while the $J^{\mathrm{Fe,Rh}}$ are only of short-range nature but distinctly positive, hence FM, such as along $[\frac{1}{2},\frac{1}{2},\frac{1}{2}]$ (half body diagonal $d/a = \sqrt{3}/2$, blue arrow indicates FM coupling between Fe-Rh). These results reveal the competition between $J^{\mathrm{Fe,Rh}}$ and $J^{\mathrm{Fe,Fe}}$ coupling, and thus the competition between the two magnetic ground states, AF and FM, given that the opposing couplings cannot be satisfied at the same time in any possible spin configuration.

Sandratskii and Mavropoulos have shown that the FM Fe-Rh interaction mostly originates from the strong hybridization of the Fe- and Rh-*d*-states, which in turn also results in the spin-polarization of the Rh *d*-electrons [30] and thus leads to the induced Rh magnetic moment $\mu_{\mathrm{Rh}} \approx 1\mu_{\mathrm{B}}$. Furthermore, they found that the hybridization induced FM Fe-Rh interaction is rather insensitive to a volume expansion, while the AF Fe-Fe interactions are decisively volume dependent, leading eventually to a compensation at a certain volume. Thus the strong volume dependency of the AF-FM transition temperature, which was identified in several pressure-dependent

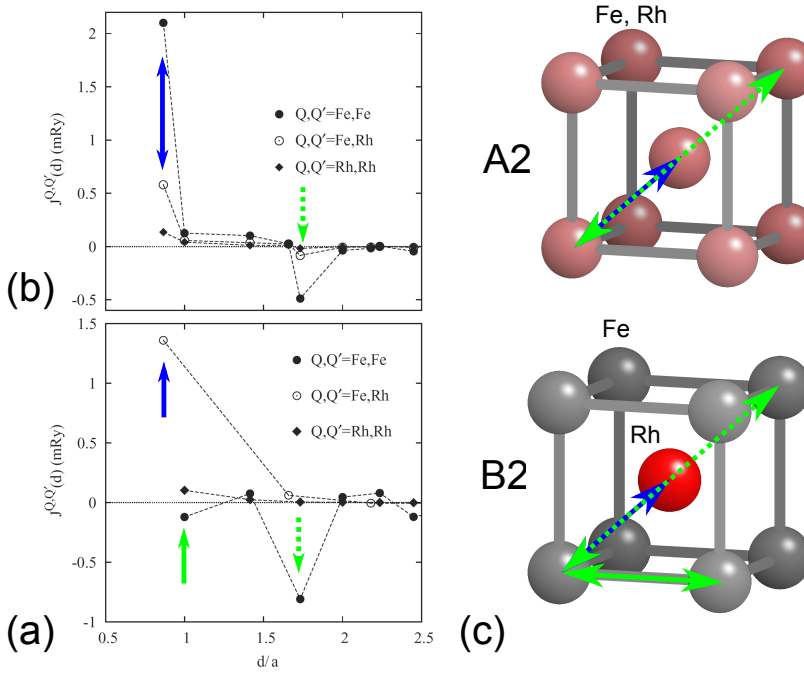

Figure 2.5.: Calculated exchange interaction $J^{Q,Q'}$, $Q, Q' = \text{Fe, Rh}$, as a function of the interatomic distance d (in units of the lattice constant a) for the ordered B2-FeRh alloy (a) and for the disordered A2 FM bcc-FeRh alloy (b). (c) Illustration of the different competing exchange couplings in the ordered and disordered structure. Blue arrows indicate FM, green ones indicate AF coupling pairs. (*Reprinted with permission from* [29]. ©2015, American Physical Society).

experimental studies [51–53], has its origin in the altered compensation temperature of the two competing exchange interaction mechanisms.

The strong volume dependence observed previously in the bulk in high pressure experiments, is also observed in thin film studies involving the growth of epitaxial FeRh films on differently mismatched substrates [54, 55] and on piezoelectric single-crystal substrates [3] allowing for reversibly changing the strain state of the film. For completeness, one study shall be mentioned, which found, in drastic contrast to all other studies, no change in the transition temperature in B2-FeRh films grown on W(001) single crystals [56]. This is a most surprising finding as the two crystalline lattices feature a mismatch of about +6% [57, 58]. Unfortunately,

due to the experimental procedure of the study involving *in situ* growth and characterization with synchrotron X-ray photo-electron-spectroscopy, no conclusive structural investigation was presented, which would allow to evaluate both strain state and degree of chemical ordering of the FeRh film. Moreover, the presented magnetic characterization builds on magnetic linear dichroism, which is not directly quantitative. Therefore, it is not entirely clear if the observed change in linear dichroism corresponds to a transition of the magnetic state of the entire film.

Yet another strong influence on the AF-FM transition is the degree of chemical ordering. A perfect, defect-free B2 ordering is of crucial importance for the occurrence of the AF phase, which is easily destroyed by just 4% anti-site defects (e.g. Fe atoms on Rh sites), driving the system into FM order [59, 60]. In a partially ordered or non-stoichiometric (Fe-rich) alloy additional strong FM interactions between Fe-Fe nearest neighbors appear along the $[\frac{1}{2}\frac{1}{2}\frac{1}{2}]$, which is depicted in Fig. 2.5(a) for an entirely disordered bcc structure. Such a strong FM contribution is not present in a perfect, equiatomic B2 structure, since in this case all Fe atoms are placed on a simple cubic lattice. These additional FM contributions overcome the ones from AF Fe-Fe pairs in [100] and [111] direction shown in Fig. 2.5(b) [29], eventually stabilizing FM in partially ordered B2-FeRh[4].

2.2.3 Metastable phases

So far the discussion has been limited to the equilibrium phases of the Fe-Rh binary alloy system. However, quite some evidence is given in the literature for the stabilization of metastable phases. As can be seen from the phase diagram Fig. 2.4, the A2-phase is only stable in Fe-rich alloys with more than 81 at.-% Fe, while at 75 at.-% it can be obtained in a martensitic transition by rapid quenching from the fcc field [61].

In alloys with even lower Fe content, towards the equiatomic composition, the A2 phase is completely suppressed by the strong B2-ordering tendency [57, 61]. Hence one must rely on calculations to describe its properties. Ohnuma *et al.* [62] derived the magnetic properties of the A2 phase in a wide composition range and predicts a FM state with an estimated T_C at the equiatomic composition of about 800 K, where Fe and Rh carry a magnetic moment of $\mu_{Fe} \approx 3\mu_B$ and $\mu_{Rh} \approx 1\mu_B$, respectively.

This robust FM behavior found in the study by Ohnuma *et al.* indicates that the FM Fe-Rh and Fe-Fe interactions between next nearest neighbors (see Fig. 2.5(b), with $d/a = \sqrt{3}/2$, blue arrow) dominate the magnetic properties of the cubic A2

[4] Partial order may arise from off-stoichiometry (Fe-rich side) but also from imperfect ordering in an equiatomic alloys.

phase despite the present AF coupling Fe-Fe pairs ($d/a = \sqrt{3}$, green arrow). Yet the presence of both kinds of opposing exchange interactions, FM and AF, in the same crystallographic direction is an indication of a possible frustration of the magnetic coupling. This is especially interesting when considering the abrupt drop of the FM $J^{Q,Q'}$ from the nearest neighbor to the next nearest neighbor distance. From this behavior a strong sensitivity of the degree of frustration of the magnetic system to the variation of the interatomic distances may be anticipated; thus in turn a distinct strain-sensitivity of the magnetic properties is expected.

Despite the results deduced from calculations, no experimental study has been presented, which unambiguously reveals the magnetic properties of the (equiatomic) A2 phase. The closest experiments were realized by deliberately disordering B2-ordered samples using high energy ion-irradiation [63, 64] or by suppressing the full development of the B2 order in thin film experiments at low growth temperatures [65]. In addition to the thermodynamic stabilization of the B2 over the A2 phase in equiatomic alloys, it was shown that the A1 phase with fcc symmetry is thermodynamically more stable than the A2 [62].

Hence, in contrast to the A2 phase, the high temperature fcc A1 phase can be prepared in a larger composition range. The latter was synthesized in a composition range from 25 - 40 at.-% Rh by rapid quenching from the melt [12, 13], and then again at compositions exceeding 60 at.-% Rh, where it is also the equilibrium structure. In the compositional range around the equiatomic composition, it is not possible to stabilize it by rapid quenching, due to the high temperature phase transition from B2→A1. Instead it can be prepared by severe deformation of the B2 structure using mechanical treatments, such as ball-milling [14–17], filing or cold-rolling [66]. High energy ion-bombardment also results, above a certain fluence threshold, in the formation of the A1 phase [25, 64, 67]. Moreover, the A1 phase is also obtained in thin film deposition experiments, when the deposition conditions, here the growth temperature, prevent adequate (surface) diffusion necessary to obtain B2 ordering [19, 20], which in some way resembles thermal quenching.

However, a thorough investigation of the magnetic properties of the A1 phase has been performed only on ball-milled specimens, which certainly complicates the interpretation of the results as the crystalline structure must be highly defective and due to the nano-size of the particles the surfaces of the particles play an important role [16]. Yet it has been concluded that the low temperature magnetic configuration is a spin glass (SG) state with a spin freezing temperature (T_f) of about 60 - 80 K [14–17], which is in some way expected given the structural disorder and the competing magnetic exchange interactions present in the system [68].

2.2.4 Lattice instabilities

The importance of lattice instabilities for the growth of highly strained films has been highlighted in the first part of this chapter. Hence, a thorough search of the published literature has been performed and indeed several different lattice instabilities and martensitic transformations have been observed under certain conditions:

In the ordered, equiatomic structure a mechanical deformation induced transformation from B2→$L1_0$ was observed [24]. The same transformation was achieved by using irradiation with high energy Au^{5+} ions, which led to the formation of the $L1_0$ structure due to irradiation damage induced stress fields [25]. Hence it seems to be an equivalent mechanism as in case of the irradiated Fe_7Pd_3 thin film [47, 48] (see Chap. 2.1.2 on page 12). Further deformation, as stated above, whether mechanical or ion-irradiation induced, leads to the formation of the A1 phase. The subsequent transformation from $L1_0$ →A1, though displaying an order-disorder transition, was shown to be reproduced by two coupled shears [69], hence also representing a lattice instability.

Moreover, it has been presented that also ternary alloying may introduce lattice instabilities. For example, in ordered $FeRh_{1-x}Pd_x$ alloys with different Pd contents, a transformation from a B2→$L1_0$ ($x = 0.1$) [26] and from B2 to an orthorhombic structure ($x = 0.62$) [27] was observed at low temperatures.

Also in the binary alloys in the composition range of 20 - 25 at.-% Rh a martensite transition fcc→bcc was obtained by quenching the disordered alloy from the fcc-field [13, 28], indicating a flat energy-landscape between the two structures.

2.2.5 Summary: Strain-ability and strain-sensitivity of disordered FeRh

In summary, the above discussed properties of the Fe-Rh binary system display promising evidence with respect to both, good strain-ability and strain-sensitivity of its magnetic properties. Especially the disordered structures offer a high metastability, which, along with highly frustrated, competing and interatomic distance-dependent magnetic exchange interactions, may allow for effective tailoring of their magnetic properties.

3 Materials and methods

In this chapter, the synthesis and main characterization methods used in this thesis are introduced and relevant experimental details are given. It begins with a brief description of the characterization techniques. The following sections deal with the thin film deposition methods and applied materials. It includes already some experimental results on the growth of the buffer layers. In this way, the main chapters are focused exclusively on the properties of the FeRh films.

3.1 Structural and microstructural characterization

Structural and microstructural investigations are of crucial importance, as the content of the thesis at hand is about the synthesis and characterization of highly strained materials. Two complementary techniques, High-Resolution X-ray Diffraction (HRXRD) and High-Resolution Transmission Electron Microscopy (HRTEM), were applied in order to obtain full understanding of the structural states present in the thin films. HRXRD was used, as standard and non-local technique, on every sample, while HRTEM, which requires laborious sample preparation techniques such as lamella preparation by Focused Ion Beam (FIB), was applied for the nanostructural investigation of selected samples.

3.1.1 High-Resolution X-ray Diffraction (HRXRD)

All HRXRD measurements presented in this thesis, were obtained using a Bruker *D8 Discover* diffractometer, featuring a four-circle goniometer (Euler cradle) necessary for single-crystal diffraction. A schematic drawing of such a diffractometer is presented in Fig. 3.1. It features the four different angles needed to align and investigate the epitaxial thin film samples: 2θ is the diffraction angle, hence the angle between incident and diffracted beam, ω denotes the angle between incident beam and the sample plane (for symmetric reflection $\omega = \theta$), ϕ describes the rotation around the sample plane normal, while χ represents eucentric tilting of the sample normal out of the diffraction plane.

The primary beam path consists of the X-ray tube with a copper anode emitting the characteristic radiation and Bremsstrahlung. Then the X-rays are shaped into a

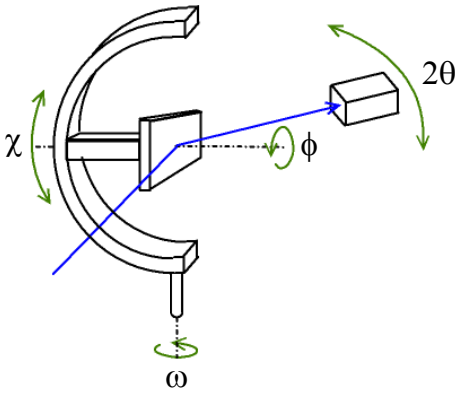

Figure 3.1.: Schematic drawing of a four-circle diffractometer. Figure adapted from [70].

parallel beam by a Göbel mirror, which removes K_β radiation as well. The beam is further shaped and monochromatized by a Ge(022) four-bounce channel-cut single crystal, resulting in Cu K_{α_1} radiation with a wavelength $\lambda = 0.154056\,\text{nm}$. In the center of the goniometer-cradle the thin film samples are positioned on a vacuum chuck. The secondary beam path consists of the BRUKER *Pathfinder* optics, which allows to choose between a secondary monochromator (for even higher resolution) and an anti-scattering slit. Per default the anti-scattering slit was used with 0.5° opening. The diffracted X-rays are finally detected by the NaI:Tl scintillation counter detector. An automatic absorber in the primary beam path, consisting of up to four thin Cu sheets, prevents the detector from receiving too high X-ray intensity, which could cause radiation damage. In the following, three different measurement modes are discussed.

X-ray Reflectometry (XRR) measurements were used to determine the thickness of each layer of the multilayer heterostructures. They were also used for calibrating the Quartz Crystal Microbalances (QCMs) of both the sputtering machine and the Molecular Beam Epitaxy (MBE) setup for each material. Prior to the measurement, the sample surface was aligned parallel to the primary beam and placed such, that it reduced the maximum intensity of the direct beam to half, which exactly corresponds to the center of the goniometer. In XRR, the small-angle part of the $\theta/2\theta$ range is scanned, where depending on the thickness and interface quality of the film interference fringes, so-called Kiessig Fringes, are observed [71]. The period of the interference in reciprocal space Δq can be traced back directly to the individual thickness t of each layer using $\Delta q_{\text{Kiessig}} = 2\pi/t$. With more elaborate models interfacial roughness can be introduced into the analysis using specialized

fitting software such as the *Leptos* package by BRUKER. The method is independent of the crystalline structure of the films, as the scattering contrast originates entirely from the difference in electron-density at the interface.

Regular wide-angle HRXRD scans were performed to determine out-of-plane lattice spacings, allowing first conclusions on the strain state of the material, and to identify structural phases. Here, the alignment procedure comprises, in addition to the steps for the correct positioning of the sample in the center of the goniometer, the adjustment of the diffraction geometry to the crystalline planes of the single crystal substrate involving 2θ, ω and χ as well. This is necessary as the substrates always have some miscut, meaning a slight angular difference between their surface and the corresponding crystal plane in this direction. In addition to the information on lattice constants and crystal symmetry obtained from the positions of the observed reflections, further information can be gathered from the presence of Laue-oscillations in the vicinity of the Bragg position. Laue-oscillations are a finite size effect, originating from the small thickness of the films. As shown by the Laue-equation Eq. 3.1, which calculates the scattering vector dependent intensity $I(q)$ for the case of a thin film with finite thickness, their periodicity depends only on the number of scattering planes N times the lattice constant c in scattering direction .

$$I(q) = \frac{\sin^2(\frac{N}{2}qc)}{\sin^2(\frac{1}{2}qc)} \qquad \text{with the scattering vector} \qquad q = \frac{2}{\lambda}\sin\theta \tag{3.1}$$

A distribution or an evolution with the thickness of the lattice constants in the film, as observed in the case of strain relaxation, via integration of misfit dislocations, would smear out the oscillations. Hence, the observation of Laue-oscillations constitutes evidence for a coherent growth of the crystalline lattice with a homogeneous c. Moreover, from the periodicity $\Delta q_{\text{Laue}} = 2\pi/Nc$ the thickness of the coherent part of the film can be obtained, which contains in comparison to the Kiessig-fringes seen in XRR additional information on the growth mode of the film and possible strain relaxation processes. The Laue-equation is derived using kinematical scattering theory. Thus, additional effects such as multiple-scattering or the influence of the substrate layer are not taken into account, which in a real experiment leads to asymmetric damping or systematic changes of position of the oscillations. By using a dynamical or semi-kinematical approach [72] it is possible to take these effect into account, which is beyond the needs of this thesis.

Even more insights into the strain state can be obtained by studying Reciprocal Space Maps (RSMs) of asymmetric reflections originating from crystal planes having an in-plane component. In that way, RSMs provide direct information on in-plane

lattice constants and possible strain-relaxation phenomena. For a typical reflection the instrument is aligned on a neighboring substrate reflection this time involving all four degrees of freedom 2θ, θ, χ and ϕ. The RSMs presented in the result chapters are all scaled in units of the in-plane and out-of-plane reciprocal scattering vectors $q_{||}$ and $q_{\perp}$, as the usual representation, which is in units of the reciprocal lattice of the substrate hkl, is not comprehensive due to the different in-plane orientations of the film and substrate structures (e.g. body centered cubic (bcc) refractory metals, such as W, grow 45° rotated on the MgO lattice [73, 74]).

In principle, one can distinguish between reflections measured in coplanar or non-coplanar geometry. The first means that the sample is parallel to the plane of the direct beam. In such a case for the measurement of an asymmetric reflection only the 2θ and ω drives are needed. Naturally this is only possible for reflections from crystal planes, which have an angle to the substrate surface that is smaller than half their Bragg-angle. These are usually planes with high out-of-plane indexes. Reflections coming from planes that do not fulfill this condition, can be observed by tilting the sample out of the plane of the direct beam by using the χ angle, which is the non-coplanar scattering geometry. The latter is less precise, due to the low resolution in χ (parts of the sample move out of the center of the goniometer and the beam imprint gets largely distorted on the sample). For that reason lattice parameters are determined from coplanar reflections only.

Moreover, as a lookahead on the results presented in Chap. 4, it will be shown that RSMs can be used to identify the space-group of the crystal structure of a film, just as in the case of regular single crystal diffraction. But of course due to the comparably small scattering volume, and thus small scattered intensity, it is extremely important to have a good starting point for the reflection search in reciprocal space. This goes beyond the usual application of RSMs, which is mostly focused on gathering information on lattice parameters, strain state, mosaicity or the substrate-film relation of a known crystal structure.

3.1.2 High-Resolution Transmission Electron Microscopy (HRTEM)

Selected samples were investigated using HRTEM, allowing to identify the local crystallographic structure and to investigate potential strain-relaxation mechanisms at the nanoscale[1].

Cross-section lamellae were prepared from the heterostructures using a FEI *Strata 400 S* instrument. The first step was performed using 30 kV Ga^+ ions while the final polishing steps were done at 5 kV and 2 kV, respectively. HRTEM investigation were

[1] HRTEM Investigations were performed by Dr. D. Wang, while the FIB lamellae were prepared by Dr. S. Schlabach, both members of Karlsruhe Institute of Technology (KIT).

carried out using a FEI *Titan 80-300* electron microscope, operated at an accelerating voltage of 300 kV, featuring a CEOS image spherical aberration corrector.

3.2 Surface topography characterization

Scanning probe techniques such as Atomic Force Microscopy (AFM) and Scanning Tunneling Microscopy (STM) were applied to study the surface topography and morphology of the bare substrates, of the magnetron-sputtered buffer layers and of the final heterostructures. In adaption to the requirements of the sample of interest either *in situ* (in Ultra-High Vacuum (UHV)) or *ex situ* AFM or STM measurements were performed. For STM, as an example, a sufficiently conducting sample is required, which prohibits the investigation of the bare MgO substrate. Therefore AFM was employed in the non-contact mode. Non-contact mode is advantageous in UHV and on non-conducting substrates as it avoids charge-build-up and electrostatic repulsion. In general, successful measurements in an AFM/STM require a compatible tip/sample surface pair, not always straightforward to achieve in an instrument operating under UHV conditions. Hence, in such cases the samples were investigated *ex situ* under atmospheric conditions.

In situ experiments were performed at room temperature (RT) using an OMICRON *VT STM*, which can be used in AFM and STM mode. *Ex situ* investigations were performed at RT using an VEECO/DIGITAL INSTRUMENTS *MultiMode AFM* in tapping mode.

3.3 Magnetic characterization

Magnetic characterization of the thin film samples has been performed using Superconductive Quantum Interference Device (SQUID) magnetometry, which is one of the most sensitive methods to measure magnetic moments. An introduction can be found in Ref. [75]. For the measurements presented in this thesis a QUANTUM DESIGN *MPMS XL5* SQUID magnetometer with a reciprocating sample option (RSO) was used.

An issue with the magnetic characterization of thin films samples arises from the magnetic contributions originating from the substrate. Although the diamagnetic susceptibilities of typical substrate materials are several orders of magnitude smaller than the non-linear susceptibility of a ferromagnetic (FM) material, they are well observable due to the about 10^6 times larger volume of the substrate compared to the actual film. This results in a linear dependence of the total magnetic moment (m_{tot}) in a magnetic field (H) dependent measurement and appears as a negative offset in

a measurement with constant applied field (e.g., Zero-Field Cooling (ZFC)-Field Cooling (FC) measurements).

One can correct for the diamagnetic contribution by fitting the linear field dependence and subtracting either this straight line or the absolute value corresponding to the diamagnetic signal in the applied H from the measured data. However, this works only well if one is able to fully saturate the magnetic material in the applied magnetic field H range. This may be true for a typical FM thin film material, while it is not straightforward for magnetic systems that are not easily saturated and/or having a small magnetic density, e.g. magnetically frustrated systems, spin glasss (SGs), non-collinear magnetic or superparamagnetic systems and in most cases antiferromagnetic (AF) materials. Hence, a H dependent contribution stemming from an unsaturated magnetic phase in the thin film is very difficult to identify.

Yet another complication arises from magnetic impurities in the substrate materials. Most metal-oxide[2] substrates and especially MgO suffer from ppm impurities of magnetic ions such as Fe [76]. This results in a strong non-linear contribution in H dependent measurements at low temperature (T), which are in the order of $1 \cdot 10^{-8}\,\mathrm{Am}^2$ (compared to about $1 \cdot 10^{-6}\,\mathrm{Am}^2$ for a 10 nm Fe film). In order to eliminate this spurious contribution, a pristine MgO substrate (from each fabrication batch) was measured and in the following subtracted from the data obtained on the actual thin films samples. This worked well for FC measurements in relatively small field H, while small differences between individual substrates are enhanced at lowest temperatures in field dependent measurements and larger fields. Therefore, $M(H)$ measurements are presented only above 30 K. Taking thus care of this issue was, together with the complementary investigations with element-specific spectroscopy introduced in Sec. 3.4, of crucial importance, considering that some of the samples showed a suppression of magnetic ordering down to low temperatures.

3.4 ^{57}Fe Mössbauer spectroscopy

^{57}Fe Mössbauer spectroscopy is an element-specific nuclear method probing the local electronic and magnetic environment of the ^{57}Fe nucleus[3]. It exploits the recoilless nuclear resonant absorption and fluorescence of γ-rays, observed for certain nuclear transitions. It was first shown and correctly explained by R. L. Mössbauer in his Nobel-prize winning work on ^{191}Ir published in 1958 [78, 79]. Afterwards the field grew rapidly, resulting already in late 1959 in the application as a local spectroscopic

[2] Semiconductor substrate materials, such as Si or GaAs, have much lower impurities levels due to the advanced semiconductor technology.

[3] While there exist also other Mössbauer isotopes, ^{57}Fe is by far the most studied [77].

method, with the first reports on the measurement of hyperfine interactions in Fe_2O_3 [80] and metallic Fe [81] in 1960.

The chemical, structural and magnetic surrounding of the site of a ^{57}Fe nucleus has direct consequences for the different hyperfine parameters and results in a certain spectroscopic fingerprint. Three hyperfine parameters are discussed in view of relevance to this thesis:

- The interaction of the nuclear monopole moment with its surrounding, or more precisely the product of the *nuclear* charge distribution with the *electronic* charge density at the nucleus, results in a shift of the energy levels of both the excited state and the ground state of the nucleus. This can lead to a relative shift of the resonant absorption line (with respect to the transition energy of the source). The resulting shift is known as the isomer shift (δ) or chemical shift and it originates from a change in the density of s electrons at the nucleus, due to various factors. For example a change of oxidation state, hence an altered shielding of s electrons by the surrounding d electrons gives a characteristic δ value as well as a composition or local structural change in an metallic alloy will affect the δ. There exist another source for a shift of the transition energy between source and absorber, namely the second order Doppler-shift (SOD), which is the result of source and absorber having different temperatures. Centroid shifts containing both, δ and SOD (obtained in temperature dependent measurements) from pure chemical δ, are referred to as center shift (CS).

- The atoms, ions and electrons surrounding the Mössbauer nucleus create an electric potential at the nucleus site, which can be transformed by twofold derivation into the electric field gradient (EFG). The interaction of the nuclear quadrupole moment (which describes the non-centrosymmetric distribution of the charges in the nucleus) with the EFG lifts the degeneracy of the excited state of the ^{57}Fe nucleus. For this reason a splitting of the absorption line into a *quadrupole doublet* is observed, which is characterized by its quadrupole splitting (ΔE_Q). It provides further information on the local symmetry of the ^{57}Fe site.

- Finally, the interaction of the nuclear spin with a magnetic field, the so-called nuclear magnetic interaction or Zeeman effect, results in a splitting of the nuclear state with spin I into $2I + 1$, nondegenerate, equally spaced (in energy) states. In the case of the ^{57}Fe nucleus, this leads to six allowed nuclear transitions and finally to a *magnetic* or *Zeeman sextet*. The observed magnitude of the splitting depends on the effective magnetic hyperfine field

(B_{HF}) at the nucleus site, which may have different origins, e.g., externally applied magnetic fields, but most importantly the spin-polarization of s electrons transferred from the spin-carrying unpaired d electrons (the so-called Fermi contact interaction [77]).

Here, it should be noticed that Mössbauer spectroscopy (as any other time-averaging method) has a characteristic time scale, which in most cases is actually the mean lifetime $\tau = 97.8 \cdot 10^{-9}$ s of the excited state. If the net B_{HF} or any other hyperfine parameter is not stable within this time window, only the time-averaged value is measured. So, for paramagnetic (PM) Fe compounds, although carrying a PM moment, no magnetic splitting is observed, while fluctuation frequencies close to the characteristic frequency of the transition result in a distinct broadening of the absorption line. Another source of line broadening is chemical disorder, hence a distribution of local environments.

As the natural abundance of the ^{57}Fe Mössbauer isotope is only about 2.2%, it was necessary to prepare thin films with isotopically enriched ^{57}Fe. The most commonly applied setup for Mössbauer measurements is the transmission geometry, used for typical bulk samples. However this is not applicable for thin films, on the one hand due to the substrate but on the other hand because of the vanishing optical thickness of the films. Hence, Conversion Electron Mössbauer Spectroscopy (CEMS) was applied. CEMS exploits the phenomenon, that the excited nuclear states, after the resonant absorption of a γ photon, decay under emission of either a γ photon (10% probability) or a so-called conversion electron (90% probability). Conversion refers here to the energy transfer from the nuclear transition into the electron system of the atom, resulting in the ejection of a core electron. The emitted conversion electrons, which exit the sample, can then be detected, solving the issues arising from the thin film geometry. CEMS counters are usually very similar to proportional counters except the source of the electrons is the sample and not the γ photons interacting with heavy inert gas elements.

CEMS spectra were measured at RT in a custom-built proportional gas-counter using a 94%He-6%CH_4 mixture. Low temperature spectra down to 80 K were measured with a similar detector placed in a bath-cryostat, here, due to the low temperatures pure He is used as detection gas. For the spectra measured below 80 K the proportional counter was replaced by a channeltron as electron detector, which is also working at liquid He temperatures[4]. The data have been analyzed using the *Normos* software package from Wissel by R. A. Brand. The δ or CS is given relative to metallic, bcc-Fe at RT throughout this thesis.

[4] Low temperature CEMS spectra were measured by U. v. Hörsten at the University Duisburg-Essen in the group of Prof. H. Wende.

3.5 Compositional analysis

Quantitative compositional analysis of thin films is not trivial. The most accurate results are usually obtained using Rutherford Backscattering Spectroscopy (RBS) [82]. RBS spectra were measured[5] using $^4He^+$ ions with an incident energy of 2 MeV from a van de Graff type high-voltage generator. The size of the beam spot, which is impinging in normal direction to the substrate surface is about 1 mm^2 size. The back-scattered $^4He^+$ ions are observed at an angle of 152°. The data were then fitted using the *SIMNRA* 6.06 software [83] and the analysis yields composition values with about 3 at.-% error.

Not all samples that are presented in this thesis could be investigated with this specialized technique, due to limited availability of this instrument at KIT. Instead Energy-Dispersive X-ray Spectroscopy (EDX) was employed for chemical analysis. EDX measurements were performed with a Zeiss *Leo 1530* scanning electron microscope, the characteristic X-ray emission was detected with a *X-Max*^{N} energy-dispersive detector from Oxford instruments. The data was analyzed with the *Aztec 3.0* software package. Despite the smaller statistical error computed by the software based on a general quantification standard, a conservative estimate for the composition uncertainty of ±5 at.-% is assumed, given the unfavorable layered thin-film geometry, the small thickness of the films and the lack of high quality standard measurements usually needed to take into account matrix effects.

3.6 Deposition methods and deposition materials

This section presents experimental details of the deposition techniques, instruments and materials used for sample preparation. Basic structural properties of the buffer layers, which then act as substrates for the Fe-Rh films, are also presented. A list of evaporation material and substrate suppliers can be found in the Appendix A.2.

3.6.1 Integrated Ultra-High Vacuum (UHV)-System

All thin film samples presented and discussed in this thesis have been prepared in the integrated Ultra-High Vacuum (UHV) System at the Institute of Nanotechnology (INT). It features several substrate preparation and deposition facilities as well as a multitude of characterization tools. Fig. 3.2 presents a top-view of the UHV-cluster, its two main parts are based on two different sample holder geometries. Since the sample preparation process comprised several individual steps in both parts of

[5] RBS spectra were measured at the Institute for Solid State Physics (KIT) by A. Beck.

the integrated system, it is necessary to use an adapter-holder during each sample preparation cycle. In Fig. 3.2 a typical sample path is depicted. Starting from the load lock the sample is transferred to the preparation chamber where the substrate can be heat treated in e.g. O_2 atmosphere or UHV. Then it is transferred to the CREATEC trolley system and the smaller OMICRON holder is placed onto an adapter. From there it can be transferred to the magnetron-sputter chamber at the end of the transfer line. After successful deposition of the buffer layer the sample is transferred back in UHV condition and after the re-transfer to the OMICRON system it can be coated in the Mini-MBE-system. Finally it can be removed from the system via the load-lock. An optional step would include the investigation of the buffer layer and/or the final multilayer with UHV-STM or AFM, as indicated by the dotted lines. So, for a typical sample in total at least seven individual transfer steps are necessary.

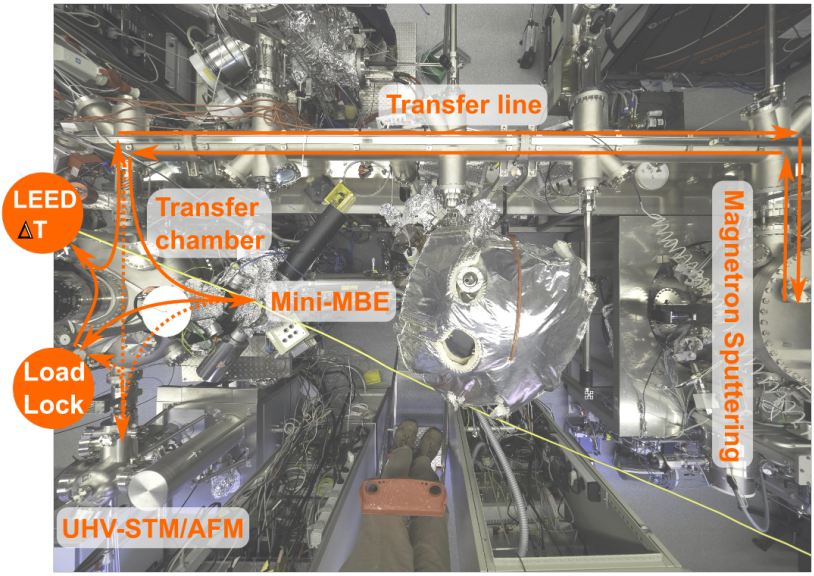

Figure 3.2.: Top-view of the UHV laboratory, the instruments applied within this thesis are marked and a typical sample path for the deposition of a Fe-Rh/W-V/MgO bilayer heterostructure is shown. Full lines indicate necessary transfers, dotted lines additional transfers, enabling e.g. a STM investigation.

3.6.2 MgO single crystalline substrates

Magnesium oxide (MgO) is a widely used substrate for thin film growth. It crystallizes in the NaCl structure with a lattice parameter of 4.212 Å. Epi-polished MgO(001) single crystal substrates ($5\times10\times0.5\,\mathrm{mm}^3$, SurfaceNET) were inserted as-bought into vacuum. In order to provide good and reproducible thermal contact, substrates were glued onto stainless steel sample holders using conductive silver glue, which is UHV-compatible after drying of the solvent. The substrates were annealed at 600 °C in an oxygen atmosphere of $2.5\cdot10^{-5}$ mbar prior to the deposition of the metal layers. This resulted in a clean single crystalline surface as evidenced by the obtained Low Energy Electron Diffraction (LEED) patterns presented in Fig. 3.3(a). *In situ* AFM investigations displayed in Fig. 3.3(b), evidence a flat surface relief due to the high-quality epi-polishing.

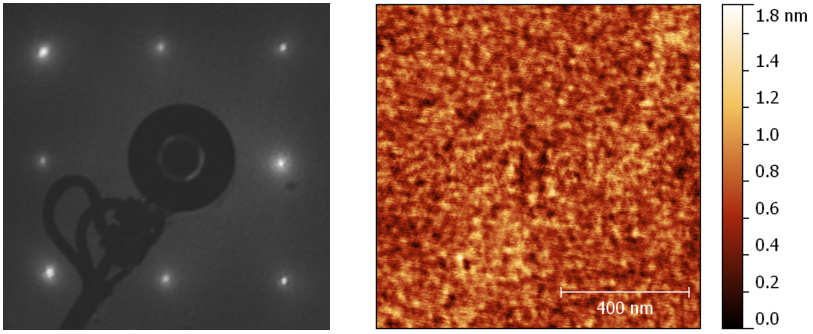

(a) (b)

Figure 3.3.: (a) LEED pattern of a cleaned MgO substrate, 143 eV electron energy. (b) AFM topographic image of a pristine MgO substrate, RMS roughness ≈ 0.3 nm.

3.6.3 Magnetron sputtering of W and W-V as buffer layers

Epitaxially grown W and W-V alloy films were employed as buffer layers for the growth of highly strained FeRh thin films. Using W-V alloy thin films allowed for the variation of epitaxial strain in the FeRh film in a controlled and predictable way by the change in the W-V lattice parameter with composition. Besides the desired rather high epitaxial misfit of 6% between the FeRh and W crystal structure (both have bcc structure), W is also beneficial because of its comparably high surface energy [84], which favors wetting and hence the smooth growth of FeRh on top.

Metallic buffer layers can be employed to tailor the strain state of a functional epitaxial thin film. This has been already shown with different elemental buffers (with naturally different lattice spacings) [22] but also the application of alloy buffer layers of fully miscible elements possessing the same crystal structure has been presented using Cr-V [85], Nb-V [86] and Cu-Au [87] alloys. Here the latter concept is applied and extended by depositing W-V alloy buffer layers. The W-V binary alloy system is known to largely follow Vegard's rule over the entire composition range [58] and it spans a lattice constant range from 3.03 to 3.165 Å, which corresponds to an epitaxial misfit $f \approx +1 - 6\%$ with respect to A2-FeRh.

Growth of W buffer layers

The W buffer layers were deposited on MgO(001) single crystals, which has been shown to result in 45° rotated epitaxial growth [73] on the oxygen sublattice. For the growth the large-distance magnetron sputtering system was applied, which already proved to be valuable for the epitaxial growth of complex oxides [43, 88]. The beneficial properties of this method could be also confirmed for the epitaxial growth of the metallic buffer layers. Therefore, only marginal deposition parameter optimization was needed. Even deposition at ambient temperature leads to epitaxial growth of the W layers. A slightly increased growth temperature improved the results in agreement with literature reports [74]. Fig. 3.4(a) presents a LEED pattern measured with 50 eV electron energy, the sharp, well defined first order diffraction spots evidence epitaxial growth and a single crystalline surface of the W film. A constant current STM image measured *in situ* directly after the deposition, shown in Fig. 3.4(b), presents a smooth surface with a low RMS roughness of 0.3 nm. HRXRD data, displayed in Fig. 3.4(c), show, in agreement with the LEED data, that only (002) planes diffract in the $\theta/2\theta$ measurement. The rocking curve presented in the inset yields a FWHM of 0.8°, which reflects the mosaicity of the W film. The latter is due to the relaxed growth of W, which is a result of the considerable epitaxial misfit of -6%. Together with the ϕ-scan of a (103) reflection in Fig. 3.4(d), which features 90° symmetry, this fully proves relaxed epitaxial growth of W on MgO(001). For comparison and coherency all W buffer layers of samples presented in the following chapters were grown under the same conditions, using 0.011 mbar back-pressure of Ar and a deposition T of 350 °C. The growth rate used was 0.022 nm/s employing a dc-sputter power of 100 W.

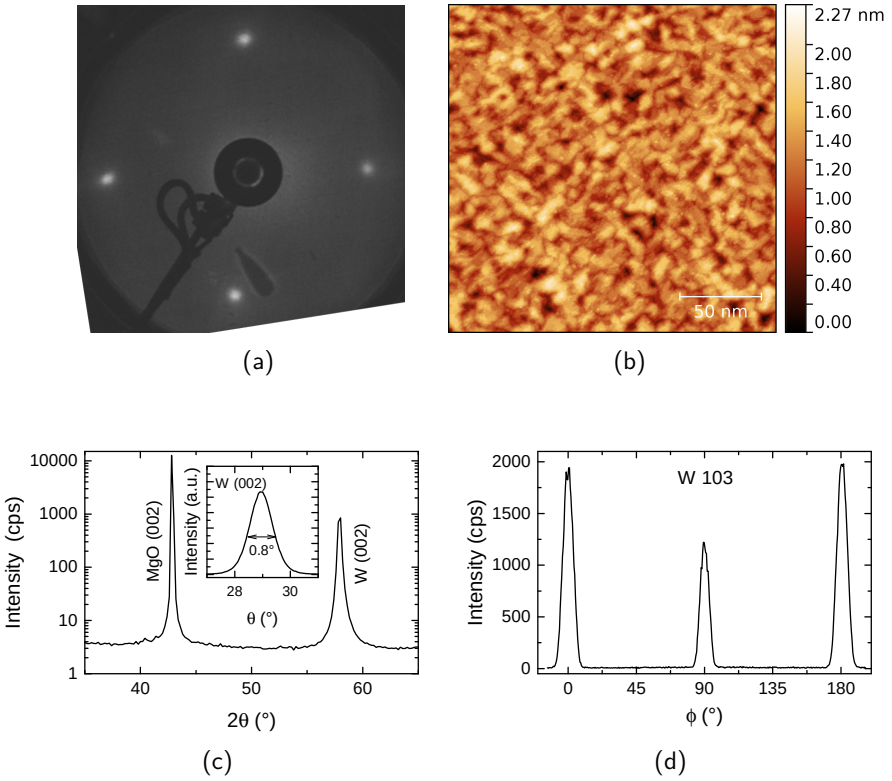

Figure 3.4.: Growth of W buffer layers: (a) W(001) LEED pattern, 50 eV electron energy, indicating epitaxial, single crystalline growth. (b) STM constant current micrograph of the W surface, RMS roughness 0.3 nm. (c) HRXRD pattern of the deposited W film, the inset shows a rocking curve of the (002) reflection, yielding 0.8° FWHM. (d) ϕ-scan of the W(103) reflection.

Growth of W-V buffer layers

W-V buffer layers were grown by using the same conditions (Ar pressure and growth temperature) as for the elemental W buffers, in order to keep the number of experimental parameters at convenient level. Hence, only the composition was varied by adjusting the dc-sputter power for each target, which yielded growth rates of 0.010 - 0.022 nm/s.

The $W_{1-z}V_z$ films grew again in a fully epitaxial way, while the lattice constants varied as expected with the V content z. This is illustrated in Fig. 3.5, where the

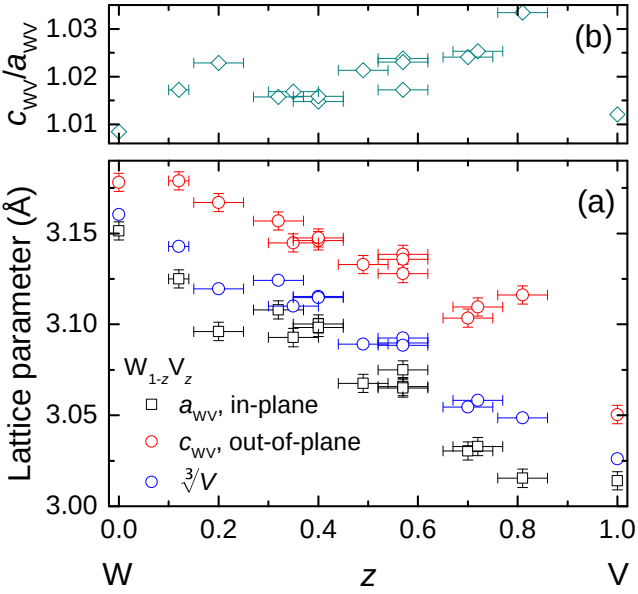

Figure 3.5.: Lattice parameters of W-V buffer layers: (a) In- and out-of-plane lattice parameters a_{WV} and c_{WV} as well as the volume averaged lattice parameter $\sqrt[3]{V}$ of $W_{1-z}V_z$ buffer layers as a function of the V-content z. (b) Tetragonal distortion c_{WV}/a_{WV} as a function of z.

variation of in-plane a_{WV} and out-of-plane c_{WV} lattice parameters, obtained from RSMs, are plotted as function of z. While both parameters decrease systematically with increasing z, it is noticeable that towards the V-rich side the two values deviate from each other more, which represents an increasing tetragonal distortion of the bcc structure, quantified by the tetragonal distortion c_{WV}/a_{WV} shown on top. The curve implies a higher strain-ability of V-rich alloys on MgO(001), which is expected given that the misfit f is decreases with higher z, while at the same time the film material becomes less stiff (the elastic constants of V are about half of those of W [89, 90]) effectively reducing the elastic energy (U_{el}). Then, towards pure V, the reduction of misfit is dominating so that the tetragonal distortion decreases again. Additionally, in Fig. 3.5(a) the volume averaged lattice parameter $\sqrt[3]{V} = \sqrt[3]{a_{WV}^2 c_{WV}}$ is given, which averages out the effect of different degrees of strained growth assuming a constant unit cell volume upon tetragonal distortion. The observed linear behavior proves that the alloy thin films follow Vegard's rule, which is well known for the bulk [58], but here it is shown for the first time for epitaxial thin films.

3.6.4 Molecular Beam epitaxy of Fe-Rh thin films

The Fe-Rh layers were deposited using a Mini-MBE system, featuring two electron beam (e-beam) *EGCO4* evaporators from Oxford applied research. The corresponding UHV chamber, which is presented in Fig. 3.6 was especially designed, assembled and commissioned within the framework of this thesis.

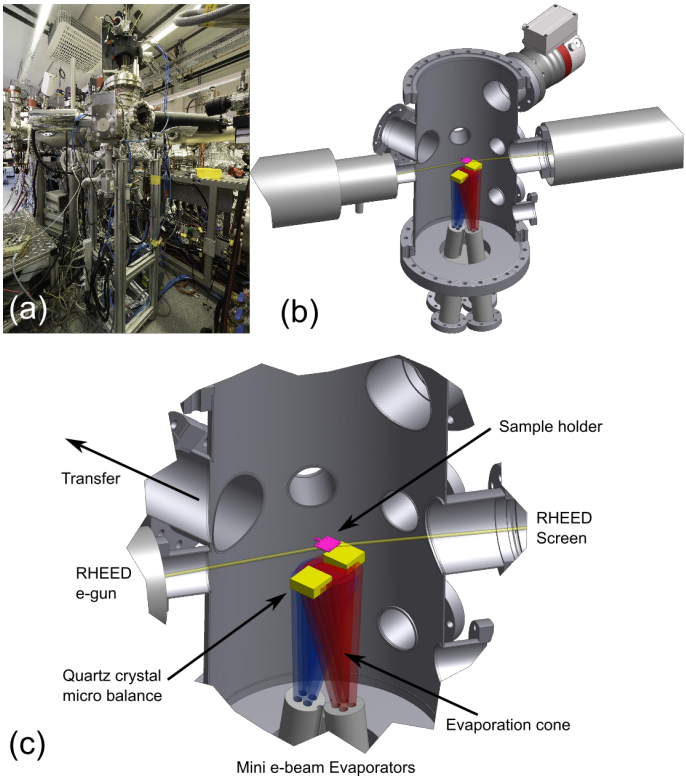

Figure 3.6.: (a) Evaporation chamber, (b) overview drawing providing a view into the chamber, and (c) detailed view of the geometry in the chamber.

Besides the two evaporators, which carry each four individually controllable evaporation sources, it features a Reflection High Energy Electron Diffraction (RHEED) system for *in situ* growth monitoring, as well as two QCMs for deposition control. Moreover, the sample temperature can be controlled with a halogen lamp, heating the sample holder from the backside. With this setup, substrate

temperatures of 800 °C can be reached. The temperature is controlled with a thermocouple located directly behind the sample holder. The base pressure of the chamber is $< 5 \cdot 10^{-11}$ mbar, achieved with two Turbo Molecular Pumps (TMPs) and an additional Ti-getter pump (not shown in the figure). The latter is used to evaporate Ti on a large part of the lower lying chamber walls, especially prior to a deposition experiment, allowing for low operation pressures of $< 9 \cdot 10^{-10}$ mbar.

The mini e-beam units evaporate the deposition material from either a rod or alternatively from a small crucible. This latter option allows the deposition of particularly costly evaporation materials, such as ^{57}Fe Mössbauer isotope. One drawback, related to the evaporators is that they do not allow for individual control of elemental deposition rates with the QCM due to the proximity of the individual source pockets as seen in the detail in Fig. 3.6(c). The QCMs measure only the integral deposited mass during co-evaporation from two sources. However, the evaporators feature an ion-flux control system, measuring the fraction of atoms that are ionized during e-beam evaporation. This ion-current, which is supposed to be proportional to the evaporation rate, can be used to maintain constant evaporation rates during an experiment. Unfortunately, due to possibly varying evaporation conditions in individual experiments (rod getting shorter, changing evaporation geometry, variation in back-pressure and hence different ionization probabilities), it is not possible to use the ion-flux as absolute control of the deposition rate.

In order to overcome this issue, two different deposition modes were used to adapt to the respective sample requirements.

I. For samples or sample series that required a comparably large film thickness but did not crucially depend on a precisely defined and perfectly reproducible film composition, co-evaporation from two sources was used. Given that it is not possible to monitor the growth rates with the QCM individually, the ion-current was used to control the flux of each source. Hence, the rate corresponding to the ion-current was calibrated prior to the deposition with the QCM, as indicated in the ion-current profile presented in Fig. 3.7(a) (region I and II). During the subsequent deposition the individual heating power was regulated by the feedback system on the corresponding ion-currents (III). This evaporation setting was usually stable for a typical deposition experiment duration of up to 60 - 90 min.

II. For samples or sample series, which instead sensitively depend on their respective composition, the use of co-evaporation is not favorable, due to the slight variations expected between individual experiments as explained above. Hence a layer-by-layer deposition method was employed, by alternating evaporation of Fe and Rh layers of one atomic monolayer (ML) thickness. This

procedure allows for precise compositional control and reproducibility of both thickness and composition. Interface alloying in Fe/Rh layers has been shown for even thicker individual layers [91] and lower deposition temperatures [92]. Together with the good wetting properties of Fe and Rh [93] homogeneous film growth and intermixing is eventually obtained. Fig. 3.7(b) displays an example of an ion-current evaporation profile. Due to the relatively laborious process it was mostly employed for film thicknesses $< 5\,\mathrm{nm}$.

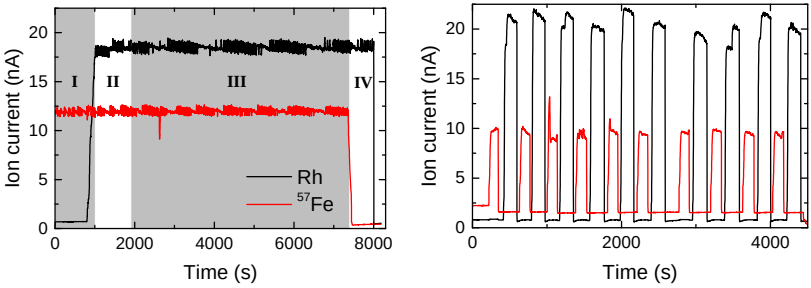

(a) Co-evaporation (b) Layer-by-layer evaporation

Figure 3.7.: (a) Ion-current profile for a co-evaporation experiment. I. calibration of the ion-current of the ^{57}Fe-source, II. calibration of the total ion-current of the ^{57}Fe and Rh-source, III. shutter open, sample deposition, IV. deposition of Rh protection layer. (b) Ion-current profile for a layer-by-layer deposited FeRh thin film.

As explained above the evaporation chamber is equipped with a RHEED system for *in situ* control of epitaxial growth, consisting of a STAIB INSTRUMENTS *EK-35-R* electron source and and a phosphorous screen for electron detection. The obtained pattern is then recorded using a CCD camera mounted on the screen flange. The system was mainly employed for qualitative monitoring of the growth process, while a quantitative analysis, including evaluation of RHEED intensity oscillations and in-plane lattice spacings, is not possible due to the sensitivity of the (primary and diffracted) electron-beam to magnetic stray-fields and the influence of stray-light coming from both the e-beam evaporators and the sample heating [94]. However, it has proven to be a very useful method providing real-time monitoring of thin film growth and surface morphology. Most importantly, epitaxial growth can be directly verified by the presence of either diffraction spots or streaks. The latter are the result of a stepped or terraced single crystalline surface, which results in a broadening of the diffraction spots in reciprocal space.

3.7 Density Functional Theory (DFT)

Density Functional Theory (DFT) calculations[6] were employed to investigate the impact of epitaxial strain and the accompanying structural changes on the magnetic properties and the electronic structure. This section will briefly explain the two computational approaches and comment on their possible outcome. More computational details can be found in reference [95].

A general problem when theoretically treating substitutionally disordered alloy systems arises from the very large super-cells needed to appropriately represent the random atomic distribution. Therefore, it has been proposed by Zunger *et al.* [96] to use a so-called Special Quasirandom Structure (SQS). SQSs are specially constructed super-cells, which mimic "the first few, physically most relevant radial correlation functions of a perfectly random structure" [96]. In this way, the super-cell size can be effectively reduced and the distribution of chemical environments eventually approximated. Moreover, in these calculations it is possible to allow individual relaxation of the atomic positions in the super-cell. These displacements may originate from structural instabilities, as has been observed in *e.g.* FePd alloys [97, 98], or can be the result of a local geometrical optimization due to differences in atomic size and orbital overlap [99].

Another approach applies the Coherent Potential Approximation (CPA), which allows to approximate the distribution of chemical environments with an effective coherent scattering potential. This self-consistent average scattering potential is then used to solve the electronic problem within the framework of the Korringa-Kohn-Rostoker (KKR) method. KKR-CPA yields good results in terms of electronic and magnetic properties of the disordered structures. It also allows to extract the magnetic exchange parameters in a Heisenberg model using the approach of Liechtenstein *et* al. [50], while it cannot, in contrast to the super-cell calculations, take into account a possible individual relaxation of atomic positions. In both methods spin-polarization of the electron density can be introduced, enabling the comparison of different magnetic configurations in energetic terms.

The two methods were applied according to their expected outcome, their limitations and computational overhead in order to shed light on the questions arising in the experimental branch of the study. The calculations allowed to solve, in a combined approach with extensive RSMs, the strain-induced FeRh martensite structure, which will be presented in detail in Chap. 4.

[6] DFT calculations were performed by PD Dr. M. E. Gruner (Theoretical Physics, University of Duisburg-Essen). The crystallographic structure of the relaxed atomic arrangements obtained in the super-cell calculations, described in Chap. 4, was solved in a joint effort with the author.

4 Epitaxial FeRh thin films on a W buffer layer: Unraveling a lattice instability

Selected parts of this chapter are also published in [95] within the framework of this thesis. The respective paragraphs – with minor conformations included – are indicated by a vertical gray bar at the inner page margin[1].

Chapter 2.2 introduced the Fe-Rh alloy system and highlighted its possible good strain-ability, as well as a pronounced strain-sensitivity of the magnetic properties to tensile strain, especially in the disordered alloys. The first goal was thus to grow chemically disordered , equiatomic FeRh films with large positive strain. For this reason, W buffer layers were chosen as substrate for the strained FeRh growth, offering an epitaxial misfit (f) $\approx +6\%$. The present chapter first deals with the basic experimental structural and magnetic characterization of the deposited epitaxial heterostructures. The findings of these investigations motivated a comprehensive and complementary study employing Density Functional Theory (DFT) calculations and extensive structural studies using Reciprocal Space Maps (RSMs) and High-Resolution Transmission Electron Microscopy (HRTEM). Eventually, the combined approach has unraveled a strain-induced structural instability in the material which underpins the observed structural changes and consequently accounts for the resulting altered magnetic properties.

4.1 Sample preparation details

First, the 50 nm thick W buffer layer was deposited as described in Chap. 3.6.3. Subsequently, an equiatomic ^{57}FeRh film, $\simeq$13 nm in thickness was deposited at room temperature (RT) by co-evaporation (deposition mode I.), as described in Chap. 3.6.4 on page 34. Finally, the layer stack was covered with a 1 nm thick Rh capping layer for oxidation protection.

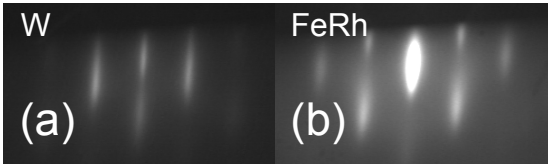

Figure 4.1.: (a) and (b): RHEED patterns for W(001) and FeRh surfaces respectively. The electron beam is aligned in [010] direction of the bcc lattice. The incident electron energy is 12 keV.

4.2 Thin film growth and characterization

Epitaxial growth was monitored using RHEED. Fig. 4.1(a) presents the RHEED pattern along the [010] azimuthal direction of the W(001) surface: the pattern is sharp and streaky, typical for a flat, single crystalline surface. During the deposition of the FeRh layer the pattern stays streaky indicating again epitaxial growth as shown by the final image in Fig. 4.1(b).

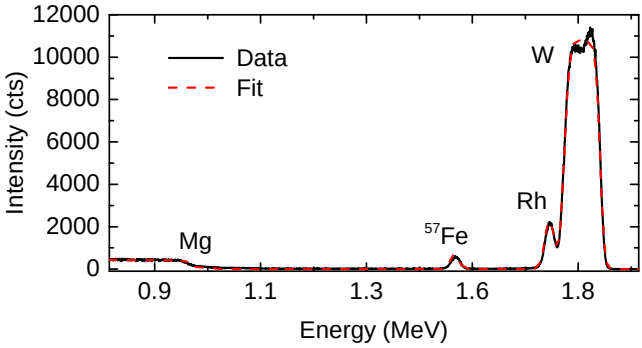

Figure 4.2.: RBS spectrum of the bilayer stack.

The composition of the FeRh layer was determined using Rutherford Backscattering Spectroscopy (RBS). The measured and fitted spectrum is shown in Fig. 4.2, yielding a composition of $Fe_{0.52}Rh_{0.48}$ (3 at.-% error), which confirms the accuracy of the calibration of the evaporation sources following the procedure described in Chap. 3.6.4 on page 34. The small spike and following drop of the backscattered intensity, visible at the edge of the W peak, is a sign of so-called channeling of the $^4He^+$ ions. Channeling is an effect of the single crystallinity of the material and

[1] *Reprinted with permission from* [95]. ©2016, American Physical Society.

hence it is only observed in epitaxially grown thin films [85, 100], where it is a sign of coherent growth and low mosaicity of the lattice[2].

The X-ray Reflectometry (XRR) pattern, displayed in Fig. 4.3(a), exhibits two interference oscillations with distinctly different periodicity, the shorter one originating from the thicker W layer, while the longer one reflects the thickness of the thinner FeRh film. As it is shown in the figure, the measured data can be fitted with a bilayer-stack model yielding 12.9 nm and 50 nm thicknesses for the FeRh and W layers respectively and 1.1 nm for the protective Rh layer[3].

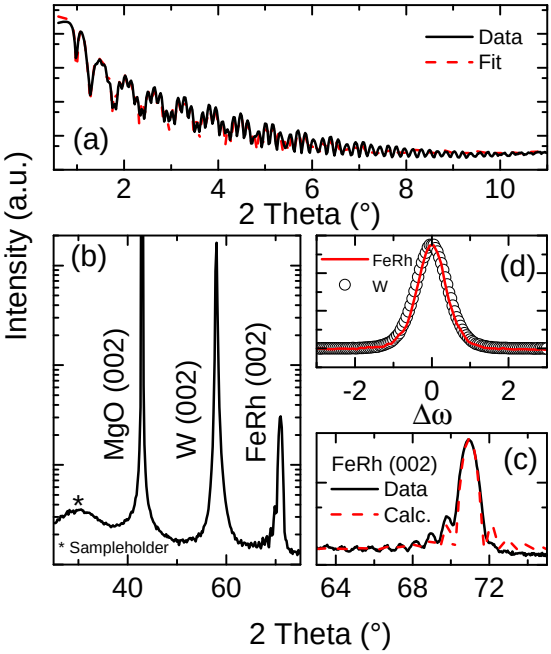

Figure 4.3: (a) XRR pattern of the bilayer stack with a fit as explained in the text. (b) HRXRD pattern showing reflections to MgO, W, and FeRh (002) planes respectively. (c) Detailed view of (002) FeRh showing Laue oscillations. The data can be approximated using the Laue-equation. (d) Comparative view of rocking curve measurements of the W and FeRh (002) reflection, showing perfectly following growth of the FeRh film on the W buffer layer.

The results of HRXRD are presented in Fig. 4.3(b). The diffraction pattern shows two reflections, in addition to the MgO(002) reflection, attributed to the (002) planes of W and of FeRh, respectively. The out-of-plane spacing of the W is 3.179(1) Å, close to the literature value of 3.165 Å [101], suggesting an almost fully

[2] The observed drop in the intensity associated with channeling usually is much larger. As it is not straightforward to align the sample correctly with respect to the beam, being that the applied setup does not allow for precise control of the sample orientation, this observation was rather fortunate and unexpected.

[3] The oscillation from the thin Rh layer are not evident, as the period is in the range of several ° and appears rather as a change in the slope.

relaxed growth of the W buffer layer on MgO(001), as has already been discussed in Chap. 3.6.3, in agreement with earlier reports [74].

The FeRh reflection reveals a lattice constant of 2.655(5) Å, implying a contraction of -11% compared to 2.989 Å for B2-FeRh in the antiferromagnetic (AF) state [57]. The reflection exhibits Laue oscillations (see Fig. 4.3(c)) due to the finite thickness of the layer. The oscillations can be approximated with the Laue equation (Eq. 3.1 on page 21), which does not take into account the multiple scattering effects coming from the multi-layer stack leading to the asymmetric damping of the oscillations [102]. Nevertheless, from adjusting the variables N and c, one obtains a coherently grown thickness of about 13.5 nm, in fair agreement with the XRR results. This proves fully coherent growth with an uniform lattice constant through the entire film, excluding gradual strain relaxation. The out-of-plane contraction with a $c/a \sim 0.84$, assuming strained, pseudomorphic growth of FeRh in a body centered tetragonal (bct) structure on fully relaxed W, is due to the large in-plane tensile, epitaxial strain (+6%). The rocking curves measured for the W and the FeRh reflection are shown in Fig. 4.3(d). The data of the FeRh film exactly follow the curve obtained from the W reflection. This observation proves, despite the rather strongly mosaic growth of W on Mgo, a perfectly oriented epitaxial growth of FeRh on W. Moreover, it is discernible that the FeRh alloy is in a disordered structure as manifested by the absence of the (001) superstructure reflection at ∼35°. The assumption of a bct structure, hence a tetragonally distorted body centered cubic (bcc) configuration, is justified by the fact that it is derived from the most closely related existing disordered structure, the A32 phase, whereas the face centered cubic (fcc) A1 phase would need to accommodate an even larger misfit of about +20%.

Table 4.1.: Mössbauer parameters obtained by fitting the CEMS spectrum: isomer shift (δ), quadrupole splitting (ΔE_Q), Lorentzian line width (Γ), Gaussian standard deviation (σ) (all given in (mm/s)).

T (K)	δ	ΔE_Q	Γ	σ
295	0.063(5)	0.148(5)	0.280(5)	0.25(1)

The magnetic and local structural properties of the FeRh thin film were element-specifically investigated with Conversion Electron Mössbauer Spectroscopy (CEMS). The spectrum measured at RT is presented in Fig. 4.4. Surprisingly, it shows no magnetic sextet, which would have been expected from the properties of the bcc

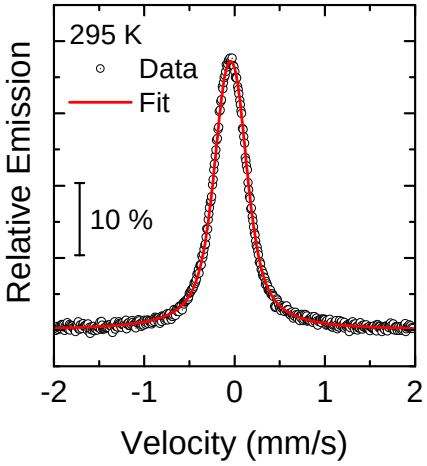

Figure 4.4: RT-CEMS spectrum of the FeRh/W bilayer, displaying a quadrupole doublet.

bulk phases [13, 57]. Instead, the spectrum is fitted best with a quadrupole doublet. Tab. 4.1 summarizes the obtained hyperfine parameters. The δ is close to what is expected for a FeRh alloy of that composition [13], while the observed ΔE_{Q} and Gaussian standard deviation (σ) are a result of the chemical disorder and distortion of the ^{57}Fe site.

As an interim result we note that the FeRh film grows highly strained in a chemically disordered state with a crystalline structure having a $c/a \sim 0.84$. CEMS evidences that ferromagnetic (FM) order is effectively suppressed in the strained FeRh film. This constitutes a quite unexpected finding given that both bcc phases A2 and B2, regardless of their chemical ordering, show a Curie temperature (T_{C}) of about 600 to 800 K [51, 62, 103, 104].

4.3 Insights from Density Functional Theory (DFT)

The experimental finding of a suppressed FM ordering in the highly strained FeRh film motivated a theoretical study, which is presented in the following.

Super-cell calculations with the *VASP* package (*Vienna Ab initio Simulation Package*), described in detail in Ref. [95], provided the first step to unravel the link between structural distortion and magnetic order on the atomic scale. A cubic 32 atom Special Quasirandom Structure (SQS) of the type A_2BC was employed, which was previously published by Jiang [105], as a starting point for the subsequent deformation and relaxation procedure.

In the beginning, we compared FM and paramagnetic (PM)[4] configurations in a bct environment with $c/a = 0.84$ (experimental value), but with atoms fixed at the ideal lattice positions. Here, we find that FM order is energetically favored as in the cubic A2 case [29, 62]. Hence, a simple strain-induced tetragonal distortion as was assumed in the previous section, would not sufficiently alter the magnetic exchange interaction according to theory, such that it could explain the experimental findings of a suppressed magnetic order.

One of the powerful features of the super-cell approach is that it allows for individual structural relaxation of atomic positions. Consequently, in a second set of calculations this possibility was exploited and the downhill relaxation of the atomic positions within the fixed super-cell (that means fixed c/a ratio) eventually leads to a PM ground state, and thus reproduces the experimental results. The relaxation process causes a cooperative displacement of the atoms from their ideal bct sites. In order to be able to relate this calculated relaxed structure to the experiment, a detailed geometrical analysis of the atomic positions in the super-cell was performed, which is described in the following paragraphs.

At first, the atomic positions of the initial bct and the relaxed configuration, which are given in relative coordinates of the primitive 32 atom super-cell, were converted with a matrix-transformation into a Cartesian coordinate system (xyz), corresponding to the principal axis of the tetragonal unit cell. The resulting atomic arrangement is shown in Fig. 4.5(a) and (d), where the parental bct arrangement is compared with the relaxed state. The upper row of the figure shows a top-view of the structure (with respect to the film geometry, hence along the c-axis), while the lower row presents a view along the in-plane b-axis. A closer look at the top-view in Fig. 4.5(a) shows that the relaxation caused a coherent in-plane displacement of the atomic positions along the [110] direction, illustrated by the arrows. The side-view (Fig. 4.5(d)) reveals that no atomic displacement in out-of-plane direction took place; hence only an alternating in-plane shuffle of atomic positions is observed.

Since the distribution of the atoms in the SQS cell does not obey cubic symmetry, the tetragonal distortion was imposed with the compressed c-axis oriented parallel to either of the three Cartesian axes, leading to essentially similar structures in terms of the relaxation pattern. Figs. 4.5(b) and (e) illustrate this is by plotting all three relaxed versions (in total 96 atoms).

The identification of the shuffle displacement made possible the determination of a new basic structural motif, hence a new unit cell, from the existing symmetries of the relaxation pattern. In the next step all atomic coordinates were translated onto only

[4] PM in the context of the DFT calculations primarily refers to a magnetically disordered state, given that the calculations as such do not include dynamic fluctuations typical of a real PM system.

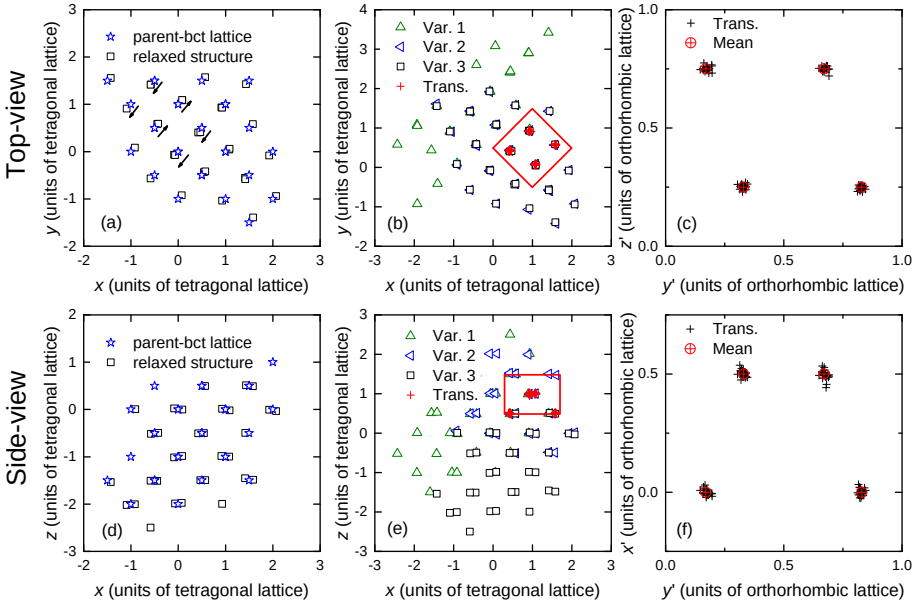

Figure 4.5.: Diagrams with atomic positions obtained in the 32 atoms super-cell calculations for the three tetragonally distorted (along each of the Cartesian coordinates) SQS cells. It illustrates how all individual atomic positions can be merged onto only four unique sites by a translation by multiples of the lattice vectors alone. By 45° rotation and scaling by $\sqrt{2}$ the final orthorhombic unit cell is obtained. (a-c) Top-view. (d-f) Side-view. (a, d) Comparison between parental-bct lattice and one relaxed variant. (b, e) Three variants (in total 96 atoms) showing the translated atom positions and the new unit cell. (c, f) Rotated orthorhombic lattice, all 96 atoms merged on four atomic positions plus the corresponding averaged mean positions.

one (arbitrarily chosen) unit cell, marked by the red square in Figs. 4.5(b) and (e), using only integral numbers of the lattice vectors in the in-plane and out-of-plane directions. The fact that only translational symmetry operations allow to reduce the entire set of 96 atoms onto only 4 reduced positions (red cross in Figs. 4.5(b) and (e)), shows the highly cooperative nature of the relaxation mechanism. In the last transformation step, presented in Fig. 4.5(c) and (f), the coordinate system was transformed by a 45° rotation and scaled by a factor of $\sqrt{2}$ into the new coordinate system $(x'y'z')$. Finally the coordinates of each of the four sites were averaged over

the corresponding individual atomic sites, yielding the mean coordinates presented in Tab. 4.2, which are also marked by the crossed circle in the figures.

x'	y'	z'
0	0.83	0.25
0	0.17	0.75
0.5	0.33	0.25
0.5	0.67	0.75

Table 4.2: Atomic positions obtained by applying translational symmetry to the atomic coordinates generated in super-cell calculations. Coordinates are expressed in the new $(x'y'z')$ coordinate system.

A symmetry analysis of the obtained basic motif, using the *FINDSYM* software [106], finds that the structure can be described in the orthorhombic space group No. 63 (*Cmcm*). The atomic rearrangement is graphically summarized in Fig. 4.6 in a top-view of the atomic columns of the parental bct lattice (left), the relaxed orthorhombic structure (right) and a superposition of both (middle). In the orthorhombic cell, the highest symmetry axis of the orthorhombic structure $a' = c$ is the out-of-plane axis of the film, while $b' = c' = \sqrt{a}$ are the in-plane axes, rotated by 45° with respect to the primary tetragonal cell. The structure can be described with only one 4c Wyckoff position $(0, y, 0.25)$ with $y = -0.17$, which represents essentially a displacement of the atoms along the b'-axis as indicated by the arrows in Fig. 4.6. Interestingly, the parental bct structure is recovered by setting $y = -0.25$, providing a direct transformation path.

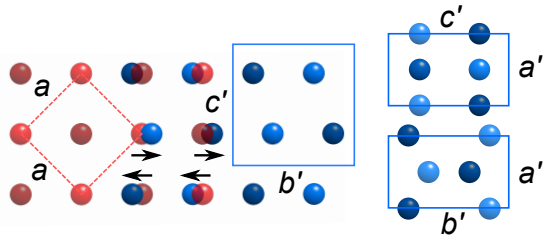

Figure 4.6.: Synoptical view of relaxed-orthorhombic and parental-tetragonal structure. View of the (left, red) bct parental lattice and the orthorhombic structure obtained by the super-cell calculation (right, blue, along all three crystallographic directions), (middle) superposition of both structures illustrating the cooperative motion of the atoms (arrows).

4.4 Structure solution

This section is dedicated to the experimental work intended to prove and refine the structural model obtained in the previous section. A short discussion of the implications of the findings is given.

4.4.1 Reciprocal Space Maps (RSMs)

The orthorhombic structure identified in Sec. 4.3 must result in an additional set of Bragg reflections, compared to the previously assumed bct structure, which can be investigated in RSMs. The structural model obtained in the super-cell calculation provides the guidance for the search of characteristic reflections in reciprocal space. Fig. 4.7(a) presents a RSM measured with azimuthal angle $\phi = 45°$ (0° corresponds per definition to the direction of the principal axes of the bcc-W lattice), hence parallel to the orthorhombic lattice. It displays the part of reciprocal space where the (220) or (202) reflections of the orthorhombic structure are expected.

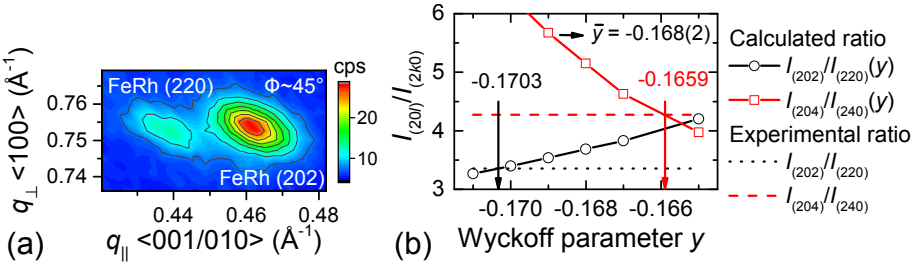

Figure 4.7.: (a) RSM intensity plots of asymmetric reflections: (202)/(220) showing the difference in in-plane lattice constants as well as their differing intensity. (b) Plot of the calculated intensity ratio $I_{(20l)}/I_{(2k0)}$ as a function of the y parameter of the 4c Wyckoff site. The measured integrated intensity ratio, obtained from fitting two 2D Gaussian peaks to the data, is plotted as straight line.

The intensity plot depicts two clearly split reflections corresponding to the above assumed planes. The reflections, which differ also in their intensity, are observed individually at different in-plane scattering vectors $q_{||}$, while their positions in the out-of-plane direction $q_\perp$ are basically identical. This is an evidence for non-equivalent in-plane lattice parameters. From fitting 2D Gaussian peaks to the (220), (202) pair of reflections and its higher order counterpart (240), (204) (shown in the Appendix A.3.1), their position in reciprocal space as well as their enclosed integrated intensities were established. The reciprocal scattering vectors are converted into real

space in-plane and out-of plane lattice constants, averaged over the two reflection pairs, resulting finally in the in-plane lattice constants $b' = 4.584(14)$ Å and $c' = 4.324(6)$ Å.

Therefore not only the change in y, predicted by theory, but also the in-plane dimensions of the unit cell reflect the orthorhombic distortion. The main characteristics of the structural rearrangement, cooperative shuffle displacement, distortion of the unit cell and lowering of symmetry, strongly suggest a martensitic nature of the observed phenomenon.

Another important result is the simultaneous observation of the two reflections, (202) and (220), in the same azimuthal direction. This implies that the film consists of 90° rotated variants (domains), similar to the adaptive nano-twinned martensites in Ni_2MnGa [46] and FePd [23] thin films. At these two points the experimental results go beyond the theoretical predictions as these particular structural features were not accounted for in the super-cell calculations.

An experimental approach to refine all crystallographic parameters independently, as in a full pattern fitting of integrated intensities for a single crystal, is very challenging in the case of epitaxial thin films. Various factors affect the integrated intensities, such as different effective beam paths of both incident and diffracted beams (asymmetric reflections), distortion of the beam imprint on the sample (in coplanar and non-coplanar geometries), change in illuminated area (as a function of ϕ, ω) and dynamical scattering effects from the underlying substrate. Therefore that kind of structural analysis is rarely found in the literature and if, then for rather thick films >100 nm, see for example [107]. Hence, a full pattern fitting is not feasible in the present case, but it will be shown that a quantitative refinement of the structure can still be achieved by combining the results of the super-cell calculation with the experimental data.

As a starting model we use the structure obtained in super-cell modeling (space-group No. 63, *Cmcm*, 4c Wyckoff site with $y = -0.17$), with the above determined orthorhombic lattice parameters. Hence, the only structural parameter that requires refinement is the y parameter of the 4c Wyckoff site (the others are fixed, due to symmetry requirements). The y parameter, which essentially describes the displacement of the atoms along b', is the major factor governing the intensity difference between reflections having either $(hk0)$ or $(h0l)$ components. By comparing the experimental ratio of integrated intensities of one pair $I_{(h0l)}/I_{(hk0)}$ with the calculated intensity ratios as a function of y, we can quantitatively determine y. Hereby we make use of the fact, that the observation of both in-plane directions b' and c' in the same azimuthal direction and their proximity in reciprocal (and also angular) space allows us to neglect, in first approximation, all scattering geometry dependent factors (since they cancel out under the division).

The intensities are calculated considering only the structure factor $(F)^5$ and the Lorentz-Polarization factor for coplanar, single crystalline diffraction [108],

$$I = F^2 \frac{1 + (\cos^2 2\theta_M)(\cos^2 2\theta)}{(1 + \cos^2 2\theta_M) \sin 2\theta} \tag{4.1}$$

with $2\theta_M = 45.306°$ the Bragg-angle of the monochromator.

Figure 4.7(b) depicts the calculated intensity ratios as a function of y and the experimentally obtained ratios (displayed as constant line) for the (202)/(220) pair as well as for the higher order reflection (204)/(204). From the intersection of the calculated curves with the corresponding experimental value a certain y value is determined, which yields a mean value of -0.168(2), in full agreement with the results of the super-cell calculations. The crystallographic parameters are summarized in Tab. 4.3.

Table 4.3: Final crystallographic parameters of the orthorhombic structure.

Spacegroup No. 63, *Cmcm*			
Lattice parameter (Å)		Wyckoff site 4c	
a'	2.655(5)	x	0
b'	4.584(14)	y	-0.168(2)
c'	4.324(6)	z	0.25

A closer look at the structural arrangement reveals surprising similarities to a hexagonal close packed (hcp) structure. This becomes clear when looking along the c' axis, which resembles a threefold axis with an ABA stacking, typical of a hcp structure. In such a model, a hypothetic hcp structure would be oriented with the hexagonal c-axis in the plane, while <110> represents the out-of-plane direction, again two 90° rotated in-plane variants would be needed to explain the data. The close resemblance between the two structures is illustrated in Fig. 4.8 in a view along the equivalent c-axes.

In an effort to unambiguously differentiate between the potentially present structures bct, hcp and *Cmcm* it was possible to successfully measure 19 out of 24 geometrically accessible reflections[6] in RSMs. Their expected positions in reciprocal

[5] F is calculated using the *Diamond* software package.

[6] The five remaining reflections were too weak and/or not observable due to an unfavorably large angle between respective scattering plane and sample surface. All other reflections not shown here are presented in the Appendix A.3.1.

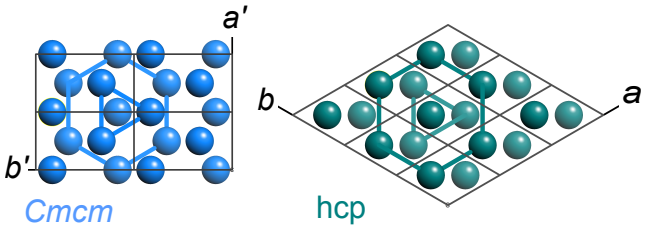

Figure 4.8.: Comparison of *Cmcm* and hcp structure. Both structures are shown along their (pseudo) hexagonal c axis.

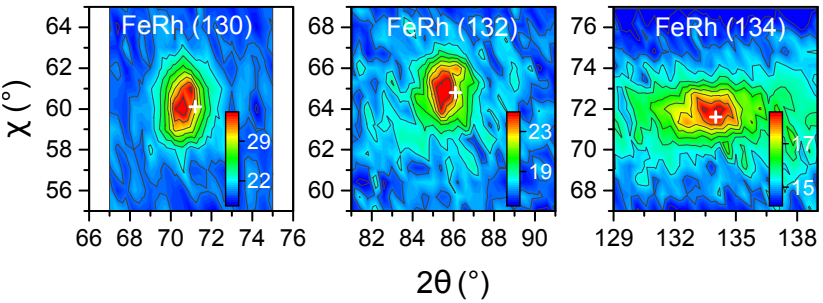

Figure 4.9.: RSMs of the (130), (132) and (134) reflection series, plotted in χ-2θ space. The three reflections are unique to the *Cmcm* structure, thus they have no counterpart in the related structures bct and hcp.

space were calculated based on the $Cmcm$ structure model. The three related structures $Cmcm$, bct and hcp naturally share common reflections. This is illustrated in Tab. 4.4 on page 65, where the list of geometrically accessible reflections for all three structures are compared and the corresponding reflections are aligned in the same row. The experimentally measured reflections are marked as well. From this comparison it becomes clear that the hcp and $Cmcm$ structure are more closely related, showing more overlap between their respective reflection lists. However, the $Cmcm$ structure features some extra reflections, due to its lower symmetry. Out of these supplementary reflections five could be clearly identified in coplanar and non-coplanar measurements. Fig. 4.9 depicts three representative reflections, namely the series (130), (132) and (134). The white cross indicates their expected position based on the $Cmcm$ structure model. Their presence finally allows to rule out a bct or hcp structure in support of the $Cmcm$ structure model.

The list of observed reflections obeys the reflection conditions for the $Cmcm$ space group: hkl, $h + k = 2n$ [109]. This is relevant, considering that also a structure

with even lower symmetry would be in principle possible, which in turn should lead to a larger number of existing reflections, due to the omitted reflection conditions. This possibility can be ruled out by the following consideration.

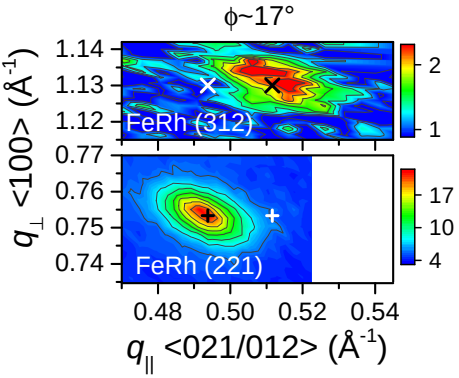

Figure 4.10: RSMs of the reflection pair (221) and (321). The black cross marks their calculated position; the white cross represents the position of a possible (212) and (321) reflection. Their absence proves that the *Cmcm* reflection conditions hkl, $h+k=2n$ are fulfilled.

Two exemplary orthorhombic reflections are discussed, namely the (221) and the higher order (in a' out-of-plane direction) reflection (312). Although the (h21) and (h12) reflections are expected at slightly different azimuthal angles ϕ of 17° and 20° respectively, due to the unequal length of the in-plane lattice constants, it is possible to observe them at the same ϕ[7]. This is illustrated in Fig. 4.10, which displays the two reflections. Their positions in reciprocal space, calculated using the crystallographic parameters shown in Tab. 4.3, are indicated by a black cross. The fact that only these very reflections appear, and not also the (212) and (321) reflections (expected position is marked by the white cross) with swapped in-plane indices, as in the case of the (220)/(202) pair, shows that the observed diffraction follows the above given general reflection condition hkl, $h+k=2n$ of the $Cmcm$ space group.

That, in summary, provides ultimate proof that the model of an orthorhombic structure, derived in the combined experimental and theoretical approach, can be unambiguously verified with the accessible diffraction data. However, a close relation of the martensite structure to a hcp structure was unraveled, which is interesting as no hcp phase has been reported in the FeRh system previously.

Given that also in bulk materials martensite transitions from bcc→hcp occur, for example in Li, Ti, Zr and Hf, it may be speculated that the final structure of the transformation is a hcp structure and the orthorhombic $Cmcm$ phase displays an intermediate state. Moreover, the transformation mechanism, which is in case

[7] Mainly due to the low resolution in ϕ, which is further virtually reduced by the in-plane rotational mosaicity of the W buffer layer, broadening the peaks also in ϕ.

of the thin films triggered by the epitaxial boundary condition, is in a similar way observed in the martensitic transformation of the high temperature β phases of noble-metal alloys, e.g. Ag, Au and Cu based alloys (after [110]). The bcc β phase transforms to a close-packed layer martensite structure by shearing along the $\{110\}_{\text{bcc}}$ transformation shear plane in either $[\bar{1}10]$ or $[1\bar{1}0]$ directions. If the shear direction is the same in every plane parallel to (110) a fcc phase results (ABC stacking), but if the shear direction is alternating every other plane a hcp structure is obtained (ABAB stacking). The correspondence of this shuffle is in our description the changing y-parameter of the Wyckoff site. To reach the close-packed arrangement additionally a homogeneous distortion of the lattice must occur, corresponding in our description to $c/a < 1$ and $c'/b' < 1$. The above proposed intermediate nature of the orthorhombic structure is supported by findings in the Ag-Cd alloy system [111]. There an orthorhombic phase was identified as intermediate state in the transition from bcc to hcp. This consideration closely links the observed strain-induced behavior in the disordered FeRh alloy to the adaptive modulated martensites occurring in the material class of shape memory alloys such as NiAl, FePd and the Heusler alloys [45]. This close relation to a hcp arrangement and the intermediate nature of the *Cmcm* structure will be further discussed in the course of the present chapter and in Chap. 5.

4.4.2 Adaptive martensite

The similarity of the observed strain-induced martensitic transformation, including the resulting arrangement of the 90° rotated variants, to the adaptive martensites in Ni_2MnGa [46] and FePd [23] thin films has already been mentioned. The following paragraphs discuss the adaptive nature of the structural relaxation in the FeRh film.

First of all it is noteworthy that the orthorhombic unit cell perfectly matches the W lattice on average, when considering that:

$$\frac{b' + c'}{2} = 4.454\,\text{Å} \approx 2d_{110}^{\text{W}} = \sqrt{2}a_{\text{W}} = 4.456\,\text{Å}. \tag{4.2}$$

This quantitative assessment is reinforced by the investigation with HRTEM, providing valuable information on the nano-scale arrangement of the structural domains.

A cross-sectional view of the film is shown in Fig. 4.11. The Focused Ion Beam (FIB) lamella was cut such that the electron beam, and hence the zone axis, is nearly parallel to the <110> direction of the W buffer layer and thus also to the orthorhombic in-plane axes of the FeRh lattice. This orientation was chosen for

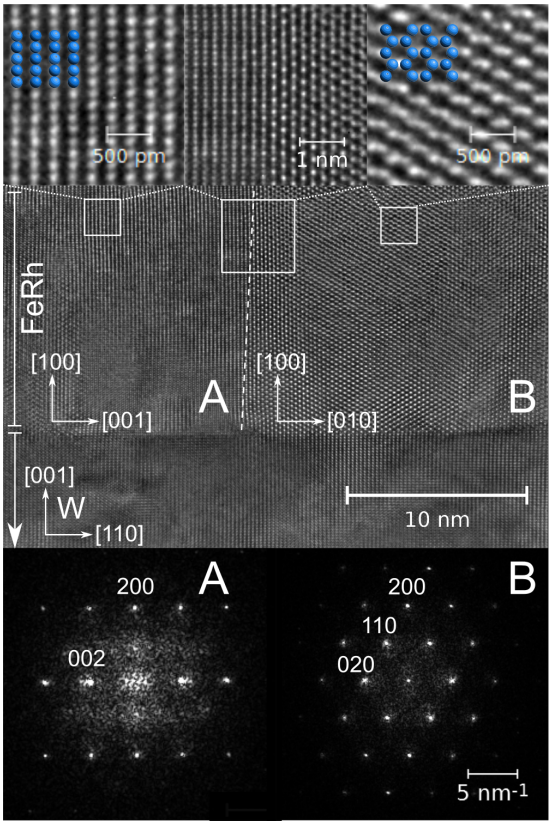

Figure 4.11: Results of HRTEM investigation. Center part: Cross-sectional view of the FeRh/W bilayer structure. In the FeRh two distinct domains with 90° rotated in-plane orientation are observed (separated by the dashed line). Bottom-row: respective Fast Fourier Transform (FFT) of the two structural domains. Top-row: Magnified images of the indicated areas, showing the projection of the structural model together with the experimental data. The center image displays the interface between both domains.

good reason, as the differences between the two expected variants with respect to their atomic arrangement (see Fig. 4.6), their in-plane lattice constant and also the resulting diffraction patterns are largest. A cross section aligned for instance along the W cubic axes <100>, would have corresponded to a [011] or [0$\bar{1}$1] direction of the $Cmcm$ lattice, which are basically not distinguishable.

Indeed, the center part of Fig. 4.11 shows a representative high-resolution micrograph featuring the top part of the W buffer layer and two FeRh grains that are oriented 90° with respect to each other in the plane. The dashed line indicates the grain boundary.

The FFT from each grain, presented in the bottom-row of Fig. 4.11, allows to determine the epitaxial relation of the two grains. Grain A is oriented with $\mathrm{FeRh}_{Cmcm}[001] \parallel \mathrm{W}[110]$ (horizontal direction in the figure), while for grain B the

same direction corresponds to FeRh$_{Cmcm}$[010]. Both grains are coherently aligned with their (100) planes parallel to the FeRh/W interface. The different orientations become apparent when comparing the two FFT patterns. FFT of grain A shows no (101) reflection while the (110) in the case of grain B is present, which is another indication for the analysis of crystallographic symmetry presented above, as it fits to the systematic reflection absence of space group $Cmcm$ (reflection condition: $hk0$, $h + k = 2n$ and $h0l$, $h, l = 2n$) [109]. Furthermore, the magnified areas presented on top in direct comparison with the structure model unambiguously illustrate the full agreement between the proposed structural model and the local lattice structure observed in the electron microscope.

The interface area between the two structural domains is magnified in the top-center image of Fig. 4.11. It clearly depicts that both grains are coherently oriented in [100] out-of-plane direction. Moreover from the obtained images an average size of the domains of about 10 - 20 nm can be determined. This nanometer-scale structure supports the supposition that strain-adaption is the real driving force for the structural rearrangements. The lateral periodicity or scale of the nanostructure is in the range of what is found for dislocation networks, which would be expected for a normal strain relaxation mechanism. The absence of dislocations in the HRTEM micrograph hence illustrates that the nano-scale alternating sequence of the two domain orientations replaces traditional epitaxial strain relaxation scenarios.

The HRTEM investigation and the above given geometric relations provide evidence for an alignment of the orthorhombic lattice along the [110] directions of the W bcc lattice. This is supported by measuring ϕ-scans of selected reflections, which displays another possibility to precisely determine the in-plane relations between the buffer layer and film lattice.

Fig. 4.12(a) presents ϕ-scans for several reflections with different in-plane components. Hence they appear at different positions in ϕ and more importantly with different periodicity. This is illustrated by Fig. 4.12(b), where the in-plane lattices of two 90° rotated variants, A and B, are drawn (each with two neighboring unit cells) and the in-plane components of the respective planes are marked as lines. Moreover, the ϕ angles between a pair of reflections is given, such as the (221) and (2$\bar{2}$1). Remarkably, these values are exactly found in the measured data. In that way each reflection observed in the ϕ-scans can be identified to originate from one of the two variants A or B, always with a 90° relation. A special case displays the (311) reflections on the bottom of the figure. The angle between (311) and (3$\bar{1}$1) planes is $\approx 92.5°$ hence $\neq 90°$ because of the orthorhombic lattice constants. The 90° rotation thus leads to an overlap of the individual reflections originating from both variants A and B, due to their proximity and their already rather broad width in ϕ, such that they cannot be distinguished clearly. In other words,

the increased width of the (311) reflections exactly confirms the epitaxial relation $[010]/[001]_{Cmcm} \parallel [110]_{\mathrm{W}}$.

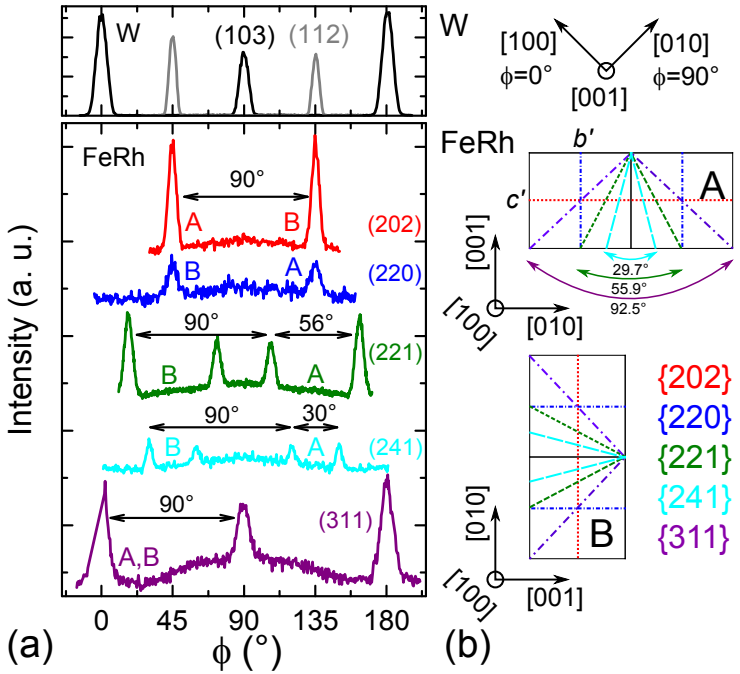

Figure 4.12.: (a) ϕ-scans of selected reflections of (top panel) the bcc-W buffer layer and the *Cmcm*-FeRh film (lower panel). The reflections are attributed to two in-plane orientations A and B. The in-plane components of the respective $\{hkl\}$ planes are presented in (b) and the angles between one pair of planes, e.g. (221) and $(2\bar{2}1)$, are given. The angular distance between these is also marked in the measured data in (a), as well as it is shown that the same pair of reflections is found 90° rotated, now originating from the other grain orientation. 0° of the ϕ-scale, as shown in (b), refers to the [100] direction of the bcc-W lattice.

The X-ray and electron diffraction experiments, which were presented and discussed previously, proved the relative orientation of the martensite domains and furthermore they showed that the domains are laterally alternating at the nano-scale. However, one question, which remained open, concerns the orientation and the structure of the interface between the two domains, hence the nature of the grain boundary. The obtained data provide no direct evidence in this case, beside the observation of the out-of-plane coherency of the two lattices by HRTEM. An attempt

to investigate the lateral arrangement of the grains by electron back-scattering diffraction (EBSD) remained unsuccessful, mostly due to the small domain size and the low film thickness. However, in the following a possible scenario is discussed.

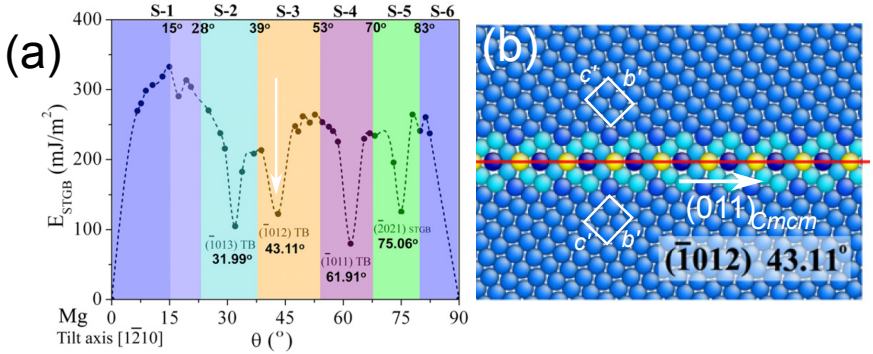

Figure 4.13.: (a) Grain boundary energies in hcp Mg for a tilting around $[1\bar{2}10]$. The arrow indicates the $(\bar{1}012)$ twin boundary, which has a tilt angle $\theta \sim 43°$. (b) Atomic arrangment for this twin boundary, the white rectangles represent the approximate size and orientation of the *Cmcm* unit cell, the hexagonal $(\bar{1}012)$ plane corresponds to the (011) in *Cmcm* indices. (*Reprinted with permission from* [112]. ©2012, Creative Commons ⓒ Attribution)

In their work on adaptive nano-twinning in FePd, Kauffmann-Weiss *et al.* [23] pointed out, that it is mostly the low twin boundary energy that allows the system to split and thereby to adapt to the preset lattice constant. A similar situation might be assumed in the case of the strained FeRh films, given that twin boundaries are the energetically most favorable high-angle grain boundaries [113]. Naturally there have been so far no calculations of grain boundary energies for the newly discovered *Cmcm* structure, however, we can exploit the similarity to a hcp structure. As already mentioned above, the hexagonal axis would lie in the plane, while the out-of-plane direction in hcp notation would be $[1\bar{2}10]$, thus the latter displays the tilt axis in order to achieve an in-plane rotation of the lattice. The potential energies for such a configuration as a function of the tilt-angle θ have been calculated for the hcp metal Mg by Wang *et al.* [112] and the result is displayed in Fig. 4.13(a). Indeed, the $(\bar{1}012)$ symmetric twin boundary, marked with an arrow, encloses a tilt angle θ that is almost reproducing the 90° rotation of the structural domains observed in the FeRh films.

Hence, it is proposed that the presence of a such a low energy twin boundary is an important condition for the occurrence of the adaptive twinning in FeRh

films and a similar atomic arrangement may well be also found here. This is illustrated in Fig. 4.13(b), which displays the calculated atomic structures of the $(\bar{1}012)$ twin boundary together with the approximate position, size and orientation of the corresponding $Cmcm$ unit cell. Such $(\bar{1}012)$ twin boundaries have already been observed experimentally by HRTEM investigations of deformed α-Ti [114]. Further experiments are planned to investigate the structure and orientation of the grain boundaries in the FeRh films using a plane-view HRTEM specimen.

4.5 Magnetic and electronic structure

In the previous sections it was shown first by theory that a PM or more precisely a magnetically disordered ground state is expected if the material undergoes a certain structural rearrangement towards an orthorhombic structure. Then this was combined with extensive HRXRD investigations using RSMs and HRTEM, yielding a refined structural model. Yet an understanding of the consequences of the structural changes for the magnetically relevant quantities, such as exchange interaction parameter (J) or magnetic moment (μ) has not been elucidated. Just as the triggering mechanism behind the martensite transformation remains unclear.

Therefore, a second set of DFT calculations was performed, now employing the Coherent Potential Approximation (CPA) for modeling the chemical disorder in a Korringa-Kohn-Rostoker (KKR) approach, as described in Sec. 3.7 on page 36. This method is applicable here as no further structural calculations are required; furthermore, the rather economic computational effort allows to map and to compare the electronic structure and magnetic properties of the two endpoints and intermediate structures all along a transformation path from cubic $\rightarrow$ tetragonal $\rightarrow$ orthorhombic FeRh. The obtained theoretical findings will be compared with detailed experimental studies of the low temperature magnetic properties.

4.5.1 Magnetic coupling along a hypothetical transformation path

The KKR-CPA calculations are carried out along a hypothetical transformation path from the cubic A2 structure to the final orthorhombic structure, using the structural parameters c/a, y and c'/b' as obtained from the experiment. Along the path, we have kept the volume per atom constant.

The energetic order of the magnetic and geometric structures and the respective changes in the electronic Density of States (DOS) obtained with the KKR-CPA approach were found to be consistent with the super-cell calculations described

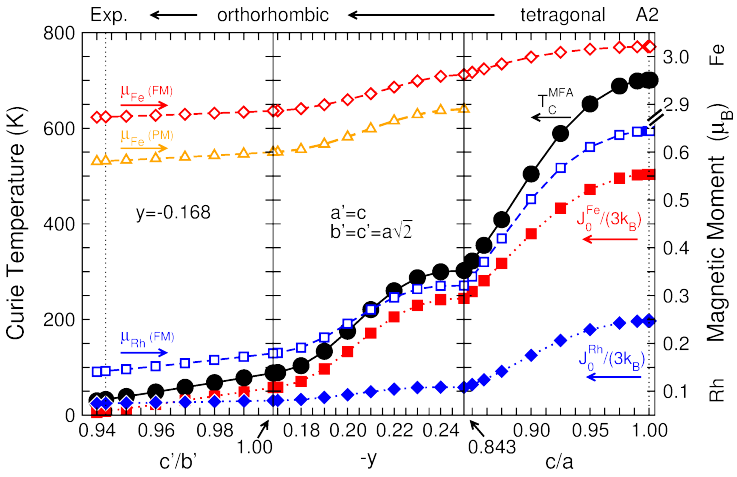

Figure 4.14.: Calculated variation of the effective exchange coupling constants $J_0^{\mathrm{Fe,Rh}}$, mean-field Curie temperature T_C^{MFA}, Rh and Fe magnetic moments, μ_{Rh} and μ_{Fe} (the latter for the FM and the PM state) along a hypothetical transformation path, from right to left: bcc-A2$\rightarrow$bct ($c/a = 0.843$) $\rightarrow$*Cmcm* ($y = -0.168, b' = c'$)$\rightarrow$*Cmcm* ($y = -0.168, c'/b' = 0.943$).

above. The T_C in the Mean Field Approximation (MFA) is directly linked to the element resolved effective intersite exchange parameters J_0^{Fe} and J_0^{Rh} by

$$k_B T_C^{\mathrm{MFA}} = \frac{2}{3} J_0 = \frac{2}{3} (0.5\, J_0^{\mathrm{Fe}} + 0.5\, J_0^{\mathrm{Rh}}). \tag{4.3}$$

The Heisenberg model exchange parameters J_0^{Fe} and J_0^{Rh} were determined using the approach of Liechtenstein *et al.* [50].

The variation of T_C^{MFA}, its element-resolved constituents and the magnetic moments μ_{Fe}, μ_{Rh} are depicted in Fig. 4.14. Starting from the right-hand side with the cubic A2 structure, we first tetragonally distort the cell, before lowering the symmetry to orthorhombic by varying the internal y-parameter. Finally, the ratio c'/b' is altered without changing the symmetry any further. With increasing tetragonal distortion, T_C^{MFA} decreases rapidly, due to a reduction of both J_0^{Fe} and J_0^{Rh}. The drastic decrease of the latter is directly linked to the altered hybridization between Fe and Rh states under these structural changes, leading to a reduced spin-polarization of Rh d-electrons and thus to a smaller μ_{Rh}.

Since the contributions to J_0^{Rh} originate mostly from FM coupled Fe-Rh pairs [29, 30] (see Fig. 2.5 on page 15 and Fig. 4.15 on the next page), the stronger decrease

in J_0^{Fe} (compared to J_0^{Rh}) cannot be explained by the reduced FM Fe-Rh interaction alone (which contributes to both, J_0^{Fe} and J_0^{Rh}). This is investigated by comparing the site-resolved pair exchange interaction parameter (J_{ij}) (with i, j = Fe, Rh) for the first part of the transformation path from bcc→bct. The results for the cubic case are in agreement with previous calculations [29], which are discussed also in Sec. 2.2. The upper panel of Fig. 4.15 directly shows that $J_{\mathrm{Fe-Rh}}$ collapses upon tetragonal distortion, which is ultimately reflected in the strong reduction of the effective Heisenberg exchange parameter J_0^{Rh} as seen in Fig. 4.14. In contrast, $J_{\mathrm{Fe-Fe}}$, presented in the lower panel of Fig. 4.15, decreases as well although remaining FM at least for the nearest and next nearest neighbors. However, for Fe-Fe pairs at larger distance new AF contributions (marked by the dashed circle) are created. Hence, the competition and degree of frustration between the short-range FM and longer ranged Fe-Fe AF interactions, already existing in the cubic structure, increases in the tetragonal structures. This directly contributes in a further reduction of the effective exchange parameter J_0^{Fe}, as seen in Fig. 4.14.

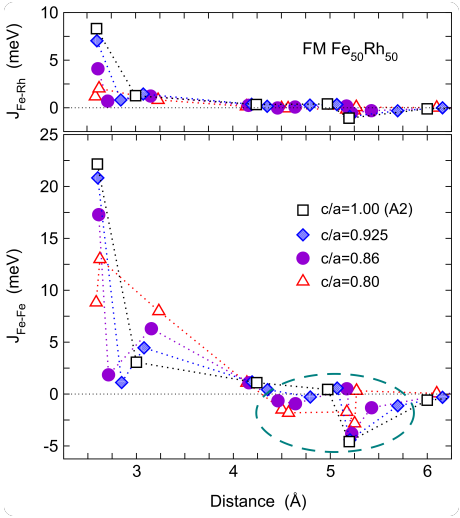

Figure 4.15: Site resolved pair exchange parameters $J_{\mathrm{Fe-Fe}}$ and $J_{\mathrm{Fe-Rh}}$ for different tetragonal distortions c/a. The dashed circle highlights the AF exchange interactions between Fe-Fe pairs at larger distances discussed in the text.

However, the bct structure with $c/a = 0.843$ still has a considerable $T_{\mathrm{C}}^{\mathrm{MFA}}$, which is above RT. This stands in contrast to the observed PM state in the epitaxial films, but is in full agreement with the preference for FM order found in the unrelaxed super-cells (see Sec. 4.3). Introducing the orthorhombic distortions enhances the competition between the different contributions, which eventually results in an effective annihilation of J_0^{Fe} as seen in Fig. 4.14. In turn J_0^{Rh} finally becomes the leading contribution to $T_{\mathrm{C}}^{\mathrm{MFA}}$. Observing that in the PM configuration, the μ_{Rh}

collapses, while the PM Fe moments remain well localized and large, decreasing by less than 0.1 μ_B with respect to the FM state, we conclude on a complete disappearance of FM order in support of a magnetically disordered configuration.

4.5.2 Magnetic ground state

The results of DFT calculations bring up an interesting question: Is the calculated PM ground state a dynamic state or rather a magnetically disordered but frozen configuration such as a spin glass (SG). The calculations do not take into account any dynamics as found in a real PM system, hence a PM state here refers to a magnetically disordered ground state. Moreover, the results of the theoretical investigation, namely the remaining large μ_{Fe} in the presence of frustrated exchange

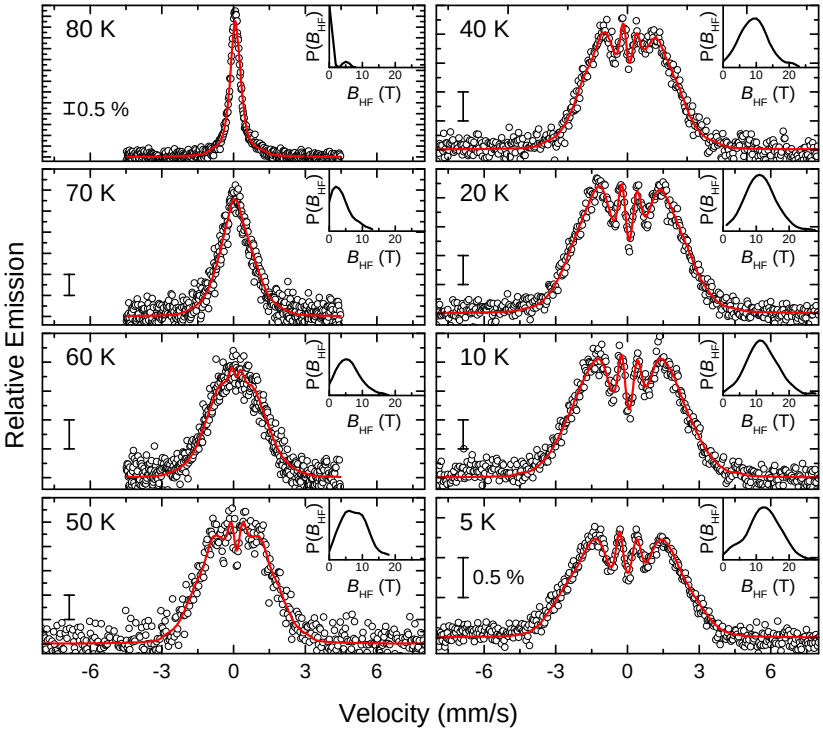

Figure 4.16.: Temperature dependent CEMS spectra from 80 - 5 K, the spectra are fitted with a distribution of B_{HF}, which is depicted in the inset.

interactions together with the inherent structural disorder, may suggest a SG configuration as the magnetic ground state at lowest temperature [115].

In order to distinguish between a dynamic or frozen magnetically disordered configuration, further, detailed CEMS measurements as a function of temperature 80 - 5 K were performed. Fig. 4.16 displays the obtained series of spectra. Starting below 70 K, the spectra develop a magnetic splitting resulting eventually in a broadened magnetic sextet at 5 K. The spectra are tentatively fitted with a distribution of magnetic hyperfine field (B_{HF}) (inset), which is as such quite expected in a disordered alloy, since the distribution of local environments in turn results in a distribution of hyperfine parameters. Fig. 4.17 plots the resulting average $\langle B_{\mathrm{HF}} \rangle$ as a function of temperature. The $\langle B_{\mathrm{HF}} \rangle$ starts to stabilize below 30 K, though not entirely saturating at low temperatures. This is expected since the magnetic frustration prevents saturation even at absolute zero temperature.

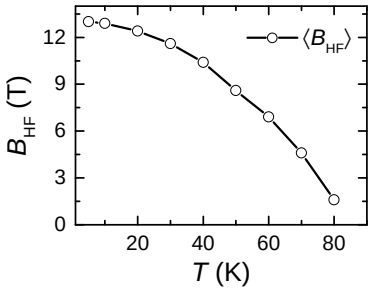

Figure 4.17: Average magnetic hyperfine field $\langle B_{\mathrm{HF}} \rangle$ as a function of temperature.

The observation obtained by the element-specific method CEMS is corroborated by magnetization measurements. Field Cooling (FC) magnetization data $M(T)$ (380 - 5 K) in a constant magnetic field $\mu_0 H$ of 50 mT are presented in Fig. 4.18. The inset shows $M(\mu_0 H)$ at 30 K for a field $\mu_0 H$ sweep from -1 to 1 T. The $M(T)$ shows no trace of a magnetic phase transition or appreciable magnetization down to 5 K. This is obvious when one compares the results with the reported reference values for the FM FeRh phases, which are represented by the hatched areas. For A2-FeRh (obtained by thermodynamical calculations based on experimental data) [62] and partially ordered B2-FeRh (experiment) [65], values are reported, which are all greater by three orders of magnitude (note the break in the magnetization axes, in order to present the actual data and the reference values). Consequently, the $M(\mu_0 H)$ sweep at 30 K, which shows no sign of FM behavior and remanent magnetization, confirms this finding.

This observation seems to be in contrast to the spectroscopic investigation with CEMS, which proves the appearance of a stable local magnetic moment below 80 K. However, the theoretically identified competing magnetic exchange interaction

already suggested a highly frustrated magnetic configuration. Therefore the macroscopic magnetic behavior of the sample is only providing further evidence for this and it can be concluded that the magnetically disordered ground state proposed by theory is most probably a frozen configuration, such as a spin glass (SG) state.

As already discussed in Chap. 3.3, such a frustrated and non-saturating magnetic phase cannot be separated from the field dependent behavior of the magnetic impurities in the MgO substrate at lowest temperatures (5 K) in a macroscopic measurement of the magnetization with a magnetometer. Without the complementary spectroscopical investigation with CEMS it would have been impossible to identify.

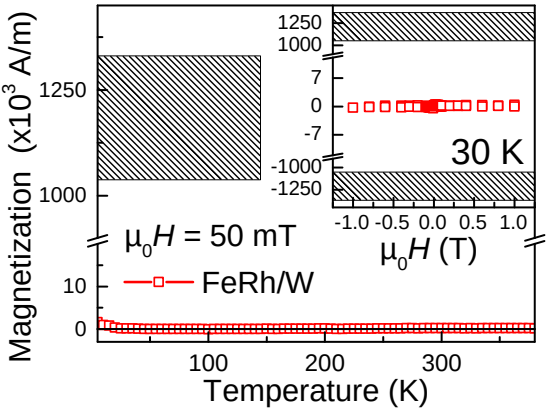

Figure 4.18.: Magnetic characterization of the FeRh/W bilayer. FC curve $M(T)$, in an external magnetic field of $\mu_0 H = 50\,\mathrm{mT}$. The hatched areas correspond to magnetization values expected for chemically disordered A2-FeRh, taken from Ref. [62, 65]. Inset: $M(\mu_0 H)$ at 30 K over a range of $\pm 1\,\mathrm{T}$.

Furthermore, the comparison of the observed magnetic behavior with the published literature reveals that the observed SG behavior, its spin freezing temperature (T_f) as well as the determined $\langle B_\mathrm{HF}\rangle$ and its temperature dependence $\langle B_\mathrm{HF}\rangle(T)$ correspond well to what was previously observed for the fcc A1 phase [14–17]. This metastable phase has been synthesized by severe mechanical deformation of the B2-ordered compound, given that the equiatomic A1 phase cannot be prepared by rapid quenching [12]. These obvious similarity of the magnetic properties of the A1 phase to the present results on strained FeRh thin films is possibly explained by the resemblance of the determined *Cmcm* structure to a hcp arrangement. Although, this structure is intrinsically different to a fcc configuration, the pseudo-close packed local environment of the *Cmcm* structure seems to be sufficiently similar to eventually determine the magnetic properties of the material.

4.5.3 Electronic structure

The disappearance of FM order becomes more apparent from a comparison of the electronic DOS in the magnetically disordered (or PM) and the FM configuration presented in Fig. 4.19 (a) and (b) respectively. Of particular interest in the latter case is the minority channel, where we observe a Rh-peak slightly above the Fermi energy (E_F) in the cubic A2 structure. With increasing tetragonal distortion, this

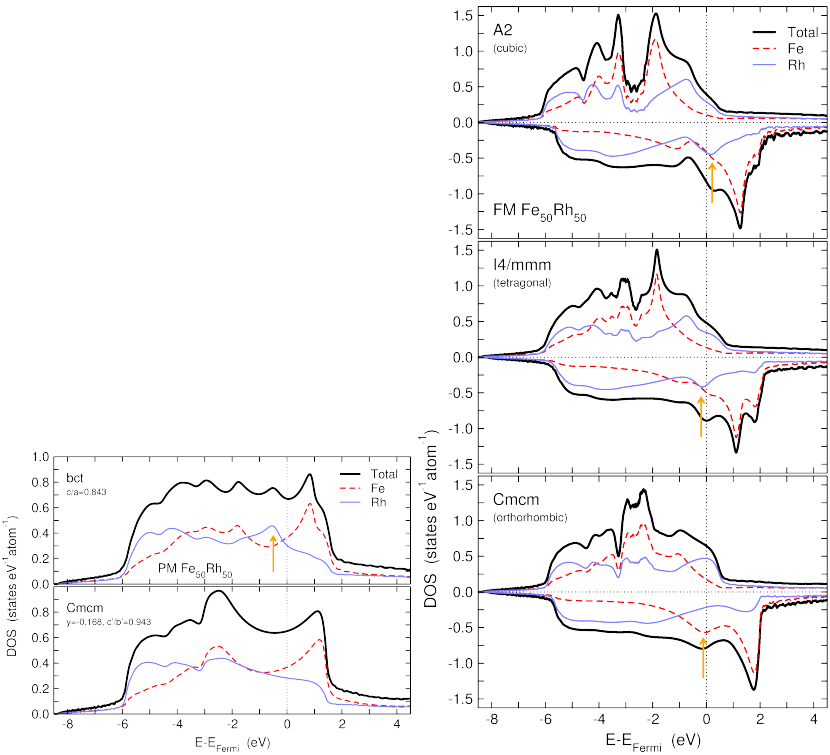

(a) PM-DOS (b) FM-DOS

Figure 4.19.: (a) Total and element resolved electronic DOS of PM (magnetically disordered) FeRh in the tetragonal state with $c/a = 0.843$ (top) and the orthorhombic ground state (bottom). (b) Total and element resolved spin-dependent electronic DOS of cubic FM A2-FeRh (top), tetragonal (center) and orthorhombic (bottom) FeRh. The negative ordinate indicates the minority spin channel. The peak-like features discussed in the text are marked by orange arrows.

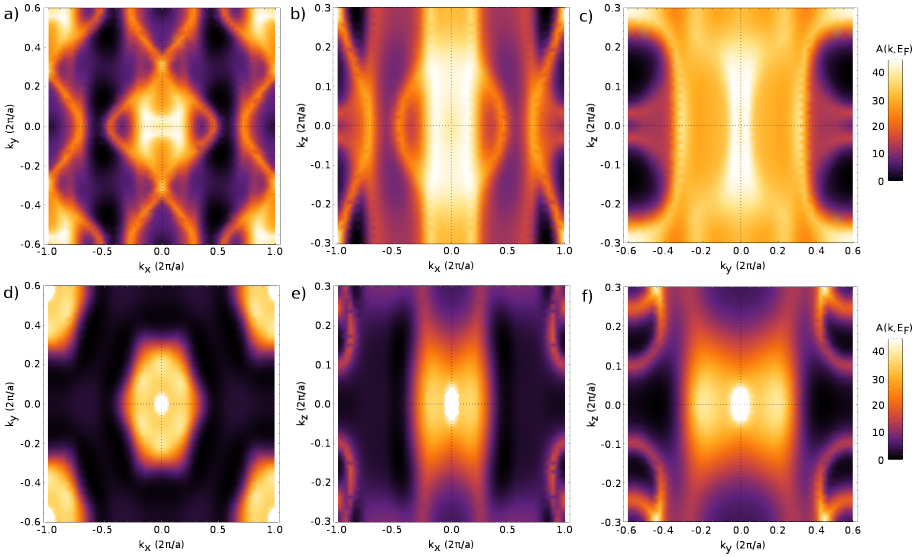

Figure 4.20.: Cross-sections through the minority spin Fermi surface of FM FeRh, in terms of the Bloch spectral function $A(\vec{k}, E_\mathrm{F})$ represented in the reciprocal coordinates of the orthorhombic lattice. The subfigures (a)-(c) refer to the k_x-k_y, the k_x-k_z and the k_y-k_z plane of the structure with tetragonal symmetry, while (d)-(f) show the corresponding plots of the final structure with orthorhombic symmetry. The colors on the intensity scale indicate to the magnitude of $A(\vec{k}, E_\mathrm{F})$ in arbitrary units.

peak eventually crosses the Fermi energy and is finally located slightly below E_F in the tetragonal structure with $c/a = 0.843$. The orthorhombic distortion completely removes this Rh peak in the minority-spin DOS – but simultaneously another peak appears in the partial DOS of Fe close to E_F. Since this feature is absent in the magnetically disordered phase, it likely contributes to a destabilization of the FM order in the final structure, leading to the observed magnetically disordered ground state.

In both magnetic states, the martensitic transformation, from bct to $Cmcm$, is accompanied by a gain in band energy, which arises from the redistribution of a peak in the Rh partial DOS just below E_F (features marked by arrows in both magnetic configurations in Fig. 4.19(a) and Fig. 4.19(b)). This is reminiscent of a band-Jahn-Teller-like mechanism, which is known from other ferrous alloys, such as Fe-Pd [97, 98].

The combination of a specific shuffling of atomic planes associated with the disappearance of a peak-like structure in the minority spin DOS is reminiscent of the Fermi surface nesting. The latter results in a softening of a phonon mode via electron-phonon coupling at a certain wave vector corresponding to the nesting vector connecting the Fermi surface in reciprocal space. Such a behavior is also known as Kohn anomaly [116]. In this view the observed shuffling of the atoms in the (110) planes in $[\bar{1}10]$ directions (bct notation) may be well described as a static, frozen phonon with a wavelength equal to $\sqrt{2}a$. This is known to play a decisive role in triggering the martensitic transformations occurring in other functional transition metal alloys and compounds, such as in the FM shape memory alloy Ni_2MnGa [117–121]. Particular cross-sections of the minority spin-channel of the Bloch spectral function $A(\vec{k}, E_F)$ in FM FeRh (Fig. 4.20) suggest the suppression of marked parallel features by the distortion. This may be counted as a first indication of nesting-induced electron-phonon coupling. A brief illustration of the band-Jahn-Teller effect and Fermi surface nesting induced phonon softening can be found in the Appendix A.1.1 on page 135.

The theoretical prediction of a possible nesting-induced phonon softening motivated a planned experimental investigation of the Fe-phonon DOS with nuclear inelastic scattering, for which a beamline proposal at the European Synchrotron Radiation Facility has been submitted.

4.6 Summary and discussion

In this chapter it was shown that a chemically disordered FeRh thin film can be epitaxially grown on top of a W buffer layer, despite the lattice mismatch being f=+6%. Moreover, it was found that the FeRh films grow fully strained and do not relax towards any known bulk structure. However, DFT calculations in combination with RSMs clarify that a certain relaxation takes place, which results in a coherently grown orthorhombic structure, that was comprehensively solved and described. The orthorhombic structure is related to a hcp structure, which is unexpected as no hcp phase has been described in the FeRh system previously. The investigation identifies the structural rearrangement as an epitaxial strain-induced martensite transition, as the displacement of the atoms from their ideal bct sites takes place in a highly cooperative way (shuffle displacement) together with a distortion of the unit cell. Moreover, the change of symmetry (from bct to orthorhombic) is a typical characteristic of martensitic transformations. DFT unravels that the tetragonal-to-orthorhombic transition is triggered by a band-Jahn-Teller-type lattice instability. First investigations indicate a possible Fermi surface nesting, which

is known to drive structural transitions in other intermetallics together with an associated phonon-softening.

HRXRD and HRTEM reveal that the film is arranged on the nano-scale in 90° rotated martensite variants, which serves to accommodate the large epitaxial misfit (f). This is illustrated by the fact that the mean in-plane lattice constant of the new orthorhombic FeRh structure exactly matches the W lattice constant. This is reminiscent of the adaptive martensites found in other ferrous alloys and intermetallics [23, 46].

The structural changes lead to the breakdown of FM order and the emergence of a SG phase at low temperatures, due to the increasing competition and frustration between FM nearest neighbor interactions (between both Fe-Fe and Fe-Rh moments) and AF coupling among Fe-Fe pairs at longer distance. The created frustration is directly linked to the reduction of the hybridization induced FM Fe-Rh interaction. The magnetic behavior resembles closely the behavior of metastable fcc FeRh, hence it is concluded that the pseudo-close-packed environment of the $Cmcm$ martensite is the decisive parameter that determines the magnetic properties.

As pointed out above, both the induced lattice instability as well as the magnetic ground state of the resulting structure is intimately linked to the Rh electronic states. So the hybridization-induced Rh moments play an important role and based on the results of the theoretical modeling, a distinct composition dependence of the observed magneto-electronic phenomena in the strained FeRh films is expected. This reasoning motivates a study of the composition dependence, which will be presented in Chap. 6.

Table 4.4.: List of geometrically accessible reflections for the bct, *Cmcm* and hcp structures. Reflections labeled with (*) have been identified in RSMs. (#) indicates reflections present exclusively in the orthorhombic structure. Reflections labeled with a minus (-) are weak and/or due to a unfavorably large angle between scattering plane and sample surface not measurable.

bct				*Cmcm*				hcp					
2 Theta (°)	h	k	l	2 Theta (°)	h	k	l	2 Theta (°)	h	k	i	l	RSM
				39.211	1	1	0	39.194	1	0	-1	0	*
44.629	1	0	1	44.663	1	1	1	44.647	1	0	-1	1	*
				58.631	1	1	2	58.618	1	0	-1	2	*
71.001	0	0	2	71.001	2	0	0	71.032	1	1	-2	0	*
				71.196	1	3	0						*, #
76.539	2	1	1	78.305	1	1	3	78.294	1	0	-1	3	*
85.06	1	1	2	84.301	2	2	0	84.257	2	0	-2	0	*
				85.912	2	0	2	85.942	1	1	-2	2	*
				86.098	1	3	2						*, #
				87.952	2	2	1	87.909	2	0	-2	1	*
98.82	2	0	2	98.915	2	2	2	98.871	2	0	-2	2	*
				104.021	1	1	4	104.01	1	0	-1	4	-
104.247	3	0	1		1	1	3						-
				104.359	1	3	3						-
				118.217	2	2	3	118.168	2	0	-2	3	*
				125.034	3	1	0	125.092	2	1	-3	0	*
129.214	2	2	2	125.411	2	4	0						*, #
				133.752	2	0	4	133.793	1	1	-2	4	*
129.585	1	0	3	129.615	3	1	1	129.677	2	1	-3	1	*
				125.638	1	5	0						-
				130.016	2	4	1						*, #
136.468	3	2	1	130.258	1	5	1						-
				144.527	1	1	5	144.509	1	0	-1	5	-
				134.009	1	3	4						*, #
				145.928	3	1	2	146.013	2	1	-3	2	*

5 Influence of the epitaxial interface on the adaptive structure

The discovered structural instability in FeRh is generated by the strain induced at the epitaxial interface between FeRh and the W buffer layer. However, the in-plane displacement of atomic positions in the relaxed structure from the positions preset by the W seeding layer is significant and represents a local structural misfit situation. Thus, a distinct influence of the film thickness on the strain-induced martensite structure is expected, which is discussed in the following chapter.

5.1 Sample preparation details

The samples presented in this chapter were prepared by using the layer-by-layer deposition approach introduced in Chap. 3.6.4 on page 33. This deposition strategy allows to achieve a defined and controllable thickness and, more importantly, an identical composition from sample to sample. Thus, any experimental parameter, other than the film thickness, is kept constant, facilitating interpretation of the results obtained. However, in contrast to the sample discussed in Chap. 4, the present sample series was deposited at a moderately increased growth temperature of 300 °C. In this way alloying between the individually deposited elemental layers was ensured [91, 92], while the course of the investigation showed that the growth temperature neither influenced the structural properties nor induced any chemical ordering. The FeRh film was coated with a Rh layer of 2 monolayer (ML) thickness for oxidation protection[1].

Five samples were prepared bridging a thickness range from 1 to 8 nm, while their composition, as obtained by Energy-Dispersive X-ray Spectroscopy (EDX), remained well equiatomic within the experimental error of the method (±5 at.-%). Fig. 5.1 presents X-ray Reflectometry (XRR) patterns measured for the sample series. The evolution of the Kiessig fringe periodicity originating from the FeRh layer is apparent, while the shorter period oscillation resulting from the thicker W layer is constant. For comparison and completeness the results obtained for the 13 nm

[1] For the thinnest samples, CEMS reveals the presence of a small amount of a Fe oxide, which is in the range of ≤1 ML of Fe.

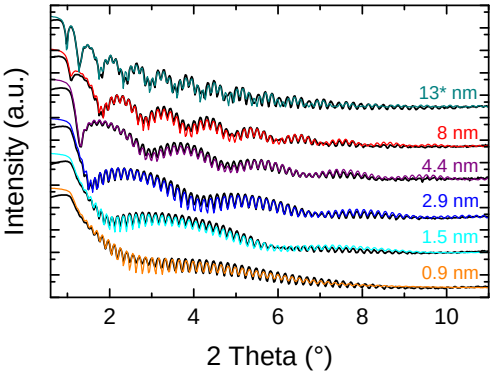

Figure 5.1: XRR patterns of the FeRh/W bilayers, with variation of FeRh thickness. The numbers given in the figure refer to the FeRh thickness, the W buffer layer thickness is kept constant with about 50 nm. The curve labeled with an asterisk marks the data presented in the previous chapter.

sample, discussed in the previous chapter, are also presented and they are labeled with an asterisk throughout the chapter. Although that sample was prepared in a different way (co-evaporation at room temperature (RT)) it integrates naturally into the present sample series, proving the equivalence of the two deposition methods with respect to the final structures.

5.2 Influence of FeRh layer thickness on the structural properties

The thickness dependence of the resulting thin film structures was investigated with two complementary methods. First, High-Resolution X-ray Diffraction (HRXRD) and Reciprocal Space Maps (RSMs) were used, providing detailed crystallographic information, and secondly Conversion Electron Mössbauer Spectroscopy (CEMS) studies were made, probing the local environment and symmetry of the ^{57}Fe sites spectroscopically.

5.2.1 Crystallographic structure

The results obtained with HRXRD are summarized in Fig. 5.2: (a) presents diffraction patterns measured for the six samples featuring the symmetric (200) reflection of the *Cmcm* crystal structure. Already the raw data reveal that the position of the reflection shifts significantly with decreasing thickness (taking the thickest, 13 nm sample as a reference), resulting in an increase of the out-of-plane lattice constant a' with decreasing film thickness, which is plotted as a function of thickness in Fig. 5.2(c) in the lower part of the graph. The reflection shows distinct Laue oscillations down to a film thickness of 2.9 nm, which provides again evidence for

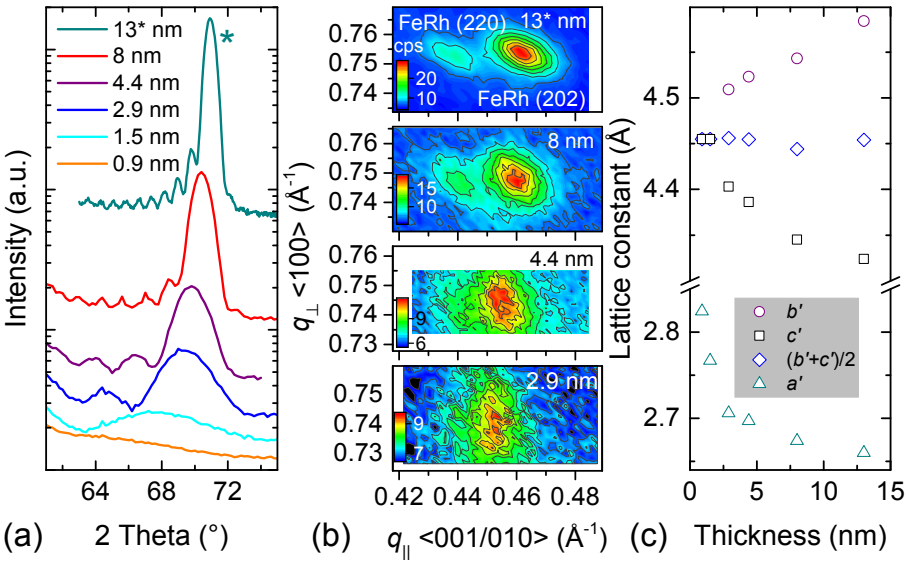

Figure 5.2.: Influence of FeRh layer thickness on the martensite structure as seen by HRXRD. (a) $\theta/2\theta$ diffraction patterns of the $(200)_{Cmcm}$ reflection. (b) RSMs of the (202), $(220)_{Cmcm}$ pair of reflection, measured for the samples with 2.9, 4.4, 8 and 13 nm thickness. (c) Synoptic view of the obtained in-plane and out-of-plane lattice constants, b', c' and a' respectively. The data labeled with an asterisk relate to the sample presented in the previous chapter.

a coherently grown film with homogeneous structure. For the even thinner film, with 1.5 nm thickness, Laue fringes might be also present but are so broad that they overlap with the tail of the W (002) reflection. For the 0.9 nm film it is barely possible to determine the position of the reflection at all, due to finite size broadening. However, some tentative value is given for a' in Fig. 5.2(c) as well.

Further information is obtained by measuring RSMs on the asymmetric (202), (220) reflections. Here it should be pointed out that these reflections in $Cmcm$ nomenclature have a counterpart in the body centered tetragonal (bct) system, namely (112). This becomes more evident when the geometric relation between the two structures is considered. Fig. 4.6 on page 44 illustrates that the $[110]_{\text{bct}}$ corresponds to the $[001]_{Cmcm}$ direction. The fact that the reflection splits into (202) and (220) is a result of the orthorhombic distortion of the unit cell $b' \neq c'$, which is also the ultimate reason why the inner change of symmetry (Wyckoff y-parameter) can be observed in the first place.

It was possible to measure RSMs for film thicknesses down to 3 nm; the results are displayed in Fig. 5.2(b). It is quite obvious that the orthorhombic splitting increases with increasing thickness, starting from a barely split reflection for the 2.9 nm sample, over an already distinctly asymmetric intensity distribution for the 4.4 nm sample, to a pronounced splitting in the 8 and 13 nm thick samples. The increased broadening in out-of-plane scattering direction $q_\perp$ reflects the finite size of the scattering volume in that direction. Fitting Gaussian curves to in-plane intensity cross-sections yields the in-plane lattice parameters presented in the upper part of Fig. 5.2(c). In case of the two thinnest samples no splitting and fully strained growth on W is assumed. The curves reflect a growing orthorhombic distortion with increasing film thickness, while the average in-plane lattice parameter $(b' + c')/2$ remains constant at the value corresponding to the W lattice. This underlines the adaptive nature of the structures in the entire thickness range. It also shows that the FeRh-W interface and the epitaxial relation remain intact. The evolution of the y-parameter is not easy to follow because the integrated intensities of the strongly overlapping reflections are not accessible. However, it is a reasonable approximation to link y to the orthorhombic distortion of the unit cell b'/c'. This suggests, judging by the disappearance of the orthorhombic splitting for the 2.9 nm sample, that the even thinner samples do not grow in the $Cmcm$ but rather in a bct structure.

Briefly summarizing the results obtained from diffraction experiments, one can state that the films evolve continuously from a pseudomorphic bct structure in the 0.9 nm thin FeRh film to the pronounced orthorhombic, adaptive martensite structure in the thickest film. The average in-plane lattice spacing remains constant, always adapting to the W buffer layer, while the out-of-plane spacing systematically decreases with film thickness.

5.2.2 Local structure

CEMS provides a local, spectroscopic view on the structural changes in the surroundings of the ^{57}Fe probe nuclei, yielding information on the local symmetry of the Fe sites complementary to the diffraction results. Fig. 5.3(a) presents the spectra measured at RT for the thickness series, while all relevant fitting parameters are summarized in Tab. 5.1. The spectra can be fitted with a narrow quadrupole doublet as already shown for the 13 nm sample presented in Chap. 4 on page 41. For the thinnest samples it is apparent that an additional subspectrum in the form of a quadrupole doublet is needed to correctly represent the measured data. The rather positive δ of this component ranging from 0.4 - 0.6 mm/s and the fact that its spectral fraction scales inversely with the thickness (see Tab. 5.1) suggest that it originates from a mixed valence surface oxide. The spectral fraction corresponds to

Table 5.1.: Mössbauer hyperfine parameters obtained by fitting the CEMS spectra: isomer shift (δ), quadrupole splitting (ΔE_{Q}), Lorentzian line width (Γ), Gaussian standard deviation (σ) (given all in mm/s). The spectral fraction (area) refers to the oxide subcomponent. Fixed parameters are labeled $^{\#}$.

t (nm)	δ	ΔE_Q	Γ	σ	Oxide (%)
13*	0.063(5)	0.148(5)	0.280(5)	0.25(1)	0
8.0	0.059(5)	0.156(3)	0.27(#)	0.23(2)	0
4.4	0.055(5)	0.160(5)	0.27(#)	0.25(1)	4
2.9	0.051(5)	0.180(10)	0.27(#)	0.24(2)	6
1.5	0.052(5)	0.200(10)	0.27(#)	0.23(1)	5
0.9	0.036(5)	0.240(8)	0.27(#)	0.26(1)	16

less than 1 ML of Fe oxide. The two subspectra are displayed together only for the 1 nm sample; in the other plots solely the fit sum is drawn for clarity. Besides the variation in the relative amount of oxide component another systematic evolution of the spectra becomes apparent, namely a distinct broadening of the spectra with decreasing film thickness. Again, as in the diffraction experiments, the co-evaporated sample naturally integrates into the series of layer-by-layer deposited samples. This broadening can be related to an increasing ΔE_{Q}, which is plotted in Fig. 5.3(b) as a function of film thickness. The Lorentzian line width (Γ) is kept constant for comparability at a value of 0.27 mm/s (Γ obtained for a Fe calibration standard), while the Gaussian standard deviation (σ) as a measure of the distribution of local environments due to chemical disorder is fitted freely. The latter remains mostly constant over the sample series. The isomer shift (δ) is also essentially constant with thickness, indicating no significant changes to the average electron density at the ^{57}Fe nucleus. Hence the observed behavior of ΔE_{Q} displays the only systematic change of a hyperfine parameter with thickness, reflecting a distinct variation of the local symmetry of the charge distribution and thus a modification of the EFG.

Calculating the absolute value of the EFG and the experimentally observable ΔE_{Q} for a given structure is not straightforward. But in the following it will be shown that it is possible to relate the observed systematic change of ΔE_{Q} to the proposed structural evolution in the FeRh films, using some reasonable approximations and symmetry considerations.

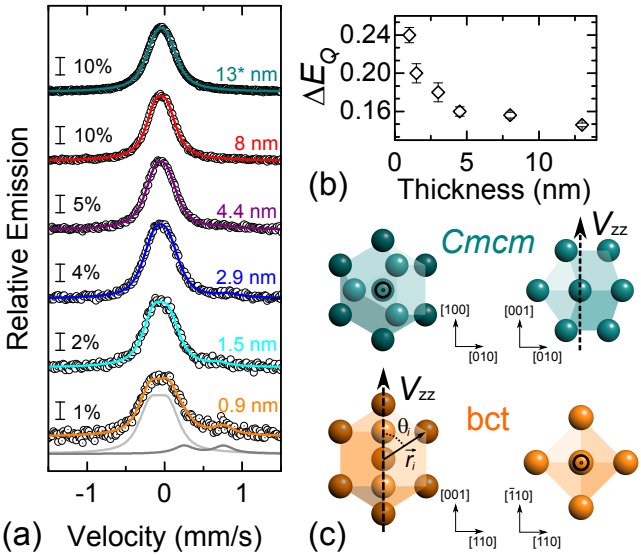

Figure 5.3.: (a) CEMS spectra measured at RT for the FeRh thickness series. The spectra are fitted with two quadrupole doublets, one attributed to the FeRh phases and a minor one, only visible in the thinnest samples, to a surface oxide. The two subspectra are plotted individually only for the 0.9 nm sample; for the rest only the fit sum is drawn. The data labeled with an asterisk relate to the sample presented in the previous chapter. (b) Evolution of ΔE_Q with FeRh thickness. (c) Nearest neighbor polyhedra for the two end point structures, bct (bottom) and *Cmcm* (top), each presented along two view directions (left: in-plane, right: out-of-plane). The arrows indicate the determined direction of V_{zz}, as explained in the text, while the polar coordinates applied for the calculation of V_{zz} are also depicted.

The first simplifying fact is that for a ^{57}Fe site with three-fold or higher symmetry, the principle axis of the EFG, the V_{zz}, is oriented along this symmetry axis. Moreover, it is known that for such a system the Hamiltonian describing the interaction of the EFG with the nuclear quadrupole moment can be simplified in a way that the following proportionality holds: $\Delta E_Q \sim V_{zz}$ [77]. Hence, for a qualitative assessment of the trend in variation of ΔE_Q it is sufficient to compare V_{zz}. In general V_{zz} can be approximated by summing up the contributions from the surrounding n point charges q, considering their relative position in space with respect to the z-axis (primary axis of the EFG tensor) in polar coordinates r and θ (as shown in Fig. 5.3(c)):

$$V_{zz} = \sum_{i=1}^{n} q_i r_i^{-3} (3\cos^2\theta_i - 1). \tag{5.1}$$

At this point the next approximation is used, by assuming point charges q for the neighboring atoms, which is a strong simplification especially in a metal, where charges are largely delocalized. Moreover, the contribution to the EFG arising from the possibly non-spherical distribution of valence electrons of the ^{57}Fe probe atom itself is neglected. Especially this contribution can alter the effective EFG significantly. But nevertheless the purely geometrical comparison allows to compare the contribution of local symmetry to the ΔE_Q in both endpoint structures, (bct and $Cmcm$), and adequately describes trends.

This is straightforward for the tetragonal structure, where the four-fold axis (the out-of-plane axis of the film) cuts through the body centered atomic site in the unit cell and therefore defines the direction of V_{zz} (as seen in Fig. 5.3(c)). The situation is less clear in the $Cmcm$ structure: here the highest crystallographic symmetry elements are the two-fold axes along the orthorhombic directions ($C\,2/m\,2/c\,2_1/m$). However, from the point-of-view of Mössbauer spectroscopy it is the local symmetry around the probe nucleus which is relevant. At this point the reader is referred to the discussion of the $Cmcm$ structure in Chap. 4.4, where the close resemblance of the $Cmcm$ structure to a hexagonal close packed (hcp) stacking was highlighted. This is further illustrated in Fig. 5.3(c), where the nearest neighbor polyhedron around one atomic site is depicted with the view direction parallel to the c' and the a' axis, respectively. Along the c' direction the atoms are arranged in a way, which is close to a three-fold axis (the angles in between are $120 \pm 0.5°$). For this reason the quasi-three-fold axis can be selected as the principal axis of the EFG, V_{zz} in the calculation.

The numbers obtained for the two structures follow a clear trend: $V_{zz}^{bct} \gg V_{zz}^{Cmcm}$ with V_{zz}^{Cmcm} being roughly 1000 times smaller, therefore in agreement with the observed experimental trend. These considerations provide only a rough approximation of the expected change of ΔE_Q between bct and $Cmcm$, solely resulting from the surrounding altered charge symmetry, but neglecting the valence electron contribution and also any local distortions resulting from the random chemical distribution of the alloy, which is known to contribute to the observed ΔE_Q. Given that the contribution arising from the local symmetry of the site in the $Cmcm$ is basically vanishing due to the high local symmetry of the site, one can conclude that the remaining, experimentally measured ΔE_Q is a result of the random chemical distribution of Fe and Rh.

5.3 Discussion

The evolution from a bct to the $Cmcm$ structure, observed by diffraction and local spectroscopy, can be qualitatively understood using thermodynamic arguments, by comparing the different contributions to the total energy U of the FeRh film system and their thickness dependence.

The first contribution arises from the tetragonal distortion induced by the epitaxial misfit between FeRh and the W buffer layer. This is the elastic energy (U_{el}), which is determined by the misfit and the elastic constants of the material, assuming fully strained, pseudomorphic growth of the distorted FeRh lattice in a bct structure. It is this contribution in the first place, which the system tries to reduce by adopting the orthorhombic structure with the entangled nano-twinned structure. Hence one can write $U_{\mathrm{el}}^{\mathrm{bct}} > U_{\mathrm{el}}^{Cmcm}$. Naturally, U_{el} is a volume term scaling linearly with the thickness (for a constant lateral area of the sample).

The second contribution to the total energy originates from the interface between the W buffer layer and the FeRh thin film. It is thus an interface energy (γ_{IF}), independent of the thickness. Here it is quite straightforward to assume that the $\gamma_{\mathrm{IF}}^{\mathrm{bct}}$ for a perfectly pseudomorphic grown FeRh layer, like in the case of a solely tetragonal distorted bct structure, is smaller than the $\gamma_{\mathrm{IF}}^{Cmcm}$ of the interface between the cubic W buffer layer and the orthorhombic FeRh structure. The latter situation involves large, unfavorable local distortions due to the coherent in-plane displacement of the atomic sites from the former bct sites, described by the Wyckoff parameter y. This local misfit between bct and orthorhombic atomic positions is illustrated in Fig. 4.6 on page 44 (neglecting for simplicity the orthorhombic distortion of the unit cell). Accordingly on can formulate $\gamma_{\mathrm{IF}}^{\mathrm{bct}} < \gamma_{\mathrm{IF}}^{Cmcm}$.

Therefore, summarizing this argument, the two competing contributions to the total energy U have an opposite dependence on the Wyckoff parameter y. Moreover, with γ_{IF} being constant (with respect to the film thickness) it is clear that the thickness dependent term U_{el} will dominate with increasing film thickness, leading eventually to the final orthorhombic structure. Whereas in the case of the thinnest films the interfacial energy dominates the elastic terms, resulting in a tetragonal structure. Hence, a structural evolution with film thickness of the FeRh film is actually expected and well explainable. Consequently, it is most probable that the structure in even thicker films may entirely relax towards a hcp arrangement, as the influence of the epitaxial interface becomes less and less important.

At this point it is worth emphasizing that the structural relaxation occurs throughout the actual film thickness and not, as for a usual strain relaxation scheme, gradually. This coherent structural behavior underlines the martensite character of the transition and the related nano-twinning even further.

Another peculiarity is the behavior of the out-of-plane lattice constant, which decreases with increasing thickness. Again in a traditional strain relaxation scenario an increase with thickness would have been expected (for a positive epitaxial misfit, hence out-of-plane compressive strain). However, in the context of the evolving phase transformation, this observation can be interpreted as evidence for different elastic constants in the two structures, resulting eventually in modified Poisson coefficients. The latter describe the ratio between the transverse and axial strain in a material in a plain stress state. A modification of the elastic constants in the *Cmcm* structure in comparison to the bct structure is conceivable as the structural rearrangement can be seen as a stress relaxing mechanism. With the strain being constant, it is essentially the altered elastic constants, which eventually reduce the epitaxial stress and hence U_{el} as well. The modification of the elastic constants directly reflects the proposed softening of a phonon mode along with the structural transformation [122], which was discussed in Chap. 4.

6 Epitaxial Fe_xRh_{1-x} thin films on W: Impact of composition on the structure and magnetic properties

In Chap. 4.5 the triggering mechanism of the lattice instability was identified in the electronic structure of the material. Density Functional Theory (DFT) calculations show that a body centered tetragonal (bct) phase is destabilized due to a local maximum in the partial Density of States (DOS) of Rh located close to the Fermi energy (E_F). The redistribution of the latter initiates the transformation to the orthorhombic phase in a band-Jahn-Teller-like mechanism within the constraints imposed by the epitaxial boundary conditions.

These structural changes form the basis of the altered magnetic properties. The origin of the drastic effects is identified in the complex interplay between ferromagnetic (FM) Fe-Rh and competing antiferromagnetic (AF) and FM Fe-Fe exchange interactions, leading to magnetic frustration. The balance between these competing interactions is decisively altered in the orthorhombic structure, mostly due to the basically vanishing hybridization induced FM Fe-Rh interaction, eventually resulting in a highly frustrated, magnetically disordered spin glass (SG) ground state.

Therefore, both the induced lattice instability in the first place, but as well the magnetic characteristics of the resulting structures are intimately linked to the Rh electronic states. This suggests a distinct Fe_xRh_{1-x} composition sensitivity of the entire magneto-electronic phenomenon, which is the topic of the present chapter.

6.1 Sample preparation details

The W buffer layer preparation is identical to the sample presented in Chap. 4. Subsequently, $^{57}Fe_xRh_{1-x}$ films, ranging from $\simeq 9 - 13$ nm in thickness, were deposited at room temperature (RT) by co-evaporation (deposition mode I.), as described in Chap. 3.6.4 on page 34. By adjusting the individual ion-currents measured during the deposition the final $^{57}Fe_xRh_{1-x}$ composition was controlled. Three bilayers with varying Fe content x were deposited, additional to the (near)-equiatomic sample presented in Chap. 4. Elemental analysis by Rutherford Backscat-

tering Spectroscopy (RBS) and Energy-Dispersive X-ray Spectroscopy (EDX) yield x=0.52, 0.57, 0.72, 0.78 with an absolute uncertainty of ±5 at.-%. As for the sample series presented before, the layer stack was covered with a 1 nm thick Rh capping layer for oxidation protection.

6.2 Thin Film Growth and Morphology

During the deposition the growth was monitored *in situ* with Reflection High Energy Electron Diffraction (RHEED). The obtained streak patterns indicate epitaxial growth for all four heterostructures (not shown). The thickness of the respective layers is obtained by means of X-ray Reflectometry (XRR). The interference patterns with pronounced Kiessig fringes are shown in Fig. 6.1. The longer period oscillation corresponds to the thinner FeRh layers whereas the short period oscillation originates from the larger thickness of the W layer. For the latter a thickness of 50(2) nm was obtained in all cases. The FeRh thickness is given in the figure for each sample. The pronounced interference fringes, which reach to a relatively high angle, demonstrate the rather low surface and interface roughness and high quality of the film in agreement with RHEED. The surface morphology of the complete layer stack, investigated by Atomic Force Microscopy (AFM), is of similar quality for all four samples (not shown), with a flat surface and a Root Mean Square (RMS) of < 0.5 nm.

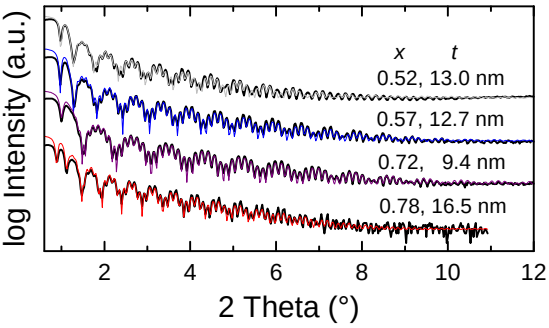

Figure 6.1: XRR patterns of the four investigated samples. The determined FeRh thickness t is also given. The measured data is plotted as black-thick line, while the fit-curve is drawn as a thin colored line.

6.3 Crystallographic structure characterization

The results of the structural investigation with HRXRD are displayed in Fig. 6.2. The diffraction patterns feature two reflections, which can be assigned to W and

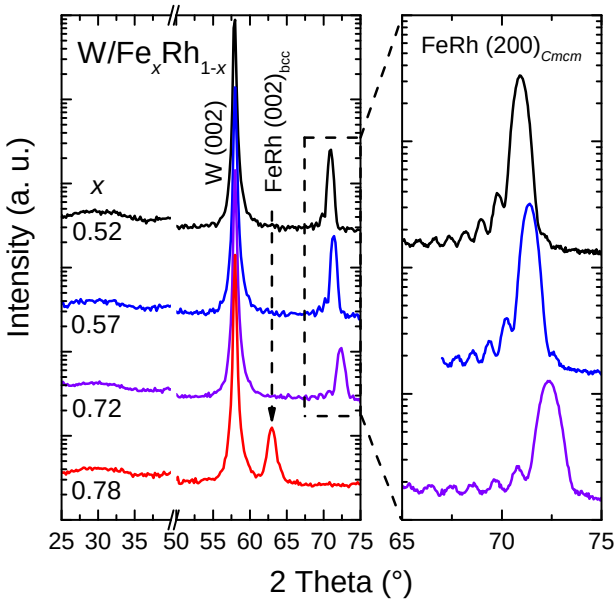

Figure 6.2.: HRXRD pattern of the Fe_xRh_{1-x}/W bilayer films. The FeRh layer grows in the adaptive orthorhombic structure for $x \leq 0.72$, the film with higher Fe content grows fully relaxed with the bulk bcc lattice constant. The inset shows a detail view of the orthorhombic FeRh (200) reflections, exhibiting pronounced Laue oscillations as a sign of highly coherent growth.

FeRh, respectively (the MgO(002) substrate reflection is hidden in the axis break). The W (002) reflection confirms an out-of-plane lattice constant of $c_W \approx 3.18$ Å for all samples in agreement with the sample investigated in Chap. 4. The remaining reflection is attributed to the FeRh layer. For the $x = 0.52$ sample the position corresponds to 2.656 Å, and it is identified as (200) reflection of the adaptive orthorhombic martensite structure [95]. With increasing Fe content, the position of the reflection constantly shifts to higher angles, meaning smaller lattice constants. This is probably due to the decreasing unit cell volume with increasing Fe content, which in turns leads to a stronger contraction in out-of-plane direction at a fixed in-plane lattice constant. Interestingly, the trend is broken for $x = 0.78$. Here a lattice constant of 2.95 Å is found, which instead is close to the literature value for a bulk sample of that composition with cubic structure [13, 57]. The inset shows a detailed view of the (200) reflection belonging to the samples with the

Cmcm structure. The shift of their position and the distinct Laue oscillations are clearly visible, providing evidence for a highly coherent growth and a uniform lattice constant throughout the film. The reflection of the $x = 0.78$ sample instead shows no oscillations.

This finding and the measured lattice constant suggest, that the orthorhombic structure is no longer stable at this composition and the film grows fully relaxed, decoupled from the W buffer layer, in a bcc structure instead. It should be emphasized that the FeRh alloy for all four samples is in a chemically disordered state as manifested in the absence of a first order superstructure reflection.

Table 6.1.: FeRh Lattice constants determined from the $(220), (202)_{Cmcm}$ and the $(112)_{bcc}$ reflections. The W in-plane lattice constant a_W is obtained from the (112) reflection. Δ is the residual misfit between the W and the FeRh lattice, for the *Cmcm* samples it refers to $\Delta = ((b'_{FeRh} + c'_{FeRh})/2 - \sqrt{2}a_W)/\sqrt{2}a_W$ for the bcc sample it is $\Delta = (a_{FeRh} - a_W)/a_W$. $^{\#}$ denotes the out-of-plane lattice constant of the film.

x	$a'^{\#}$ (Å)	b' (Å)	c' (Å)	a_W (Å)	Δ (%)
0.52(5)	2.655(1)	4.584(14)	4.324(6)	3.151(1)	-0.05
0.57(5)	2.644(2)	4.545(3)	4.315(2)	3.149(1)	-0.5
0.72(5)	2.608(1)	4.513(4)	4.267(2)	3.155(1)	-1.6
	a (Å)		$c^{\#}$ (Å)		
0.78(5)	2.951(1)		2.944(1)	3.158(1)	-6.6

Further structural information about the crystallographic structure is obtained by means of RSMs. Fig. 6.3(a) presents RSMs of the samples with $x \leq 0.72$, the axes are labeled according to the *Cmcm* unit cell with a being the out-of-plane axis. The individual graphs share the identical $q_{||}$ axis, whereas the $q_\perp$ axis is adapted to the position of the intensity maximum. The left panel shows the (221) reflection, which is not present for a bcc or bct structure and it is only allowed in the orthorhombic symmetry. Observed under an azimuthal angle $\phi \approx 17°$ ($0°$ refers to one of the cubic axes of the W-bcc lattice) it is direct evidence for the orthorhombic structure. On the right side the (220) and (202) reflections are presented. The observation of both principal crystallographic directions of the orthorhombic lattice in the same azimuthal direction evidences the presence of the two rotated martensitic variants

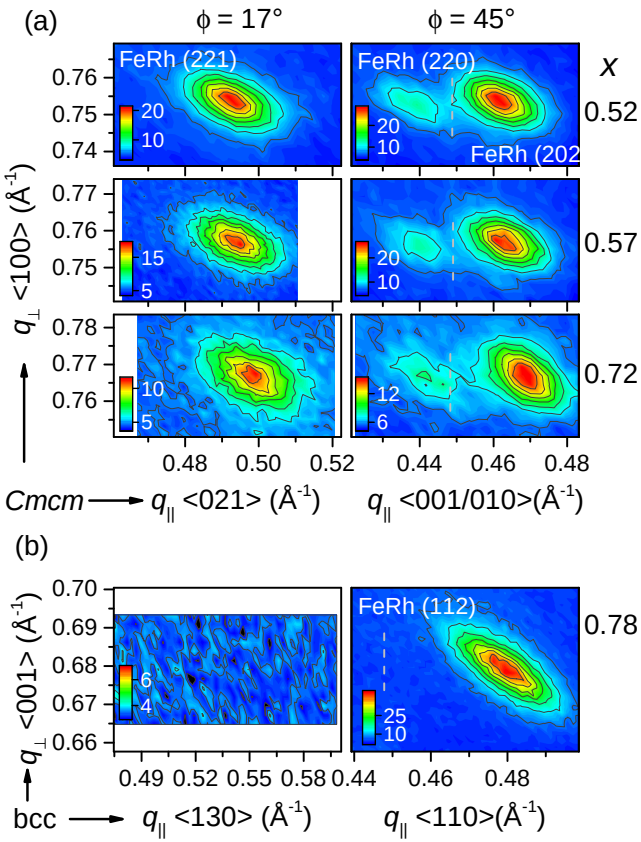

Figure 6.3.: RSMs of FeRh reflections. (a) Displays the (221) and (220), (202) reflections of the samples in the *Cmcm* regime, respectively. The presence of the (221) reflection confirms orthorhombic symmetry. (b) Presents the same regions in reciprocal space. The absence of the orthorhombic reflection in the left panel rules out orthorhombic symmetry, therefore the axes are labeled according to a bcc or bct lattice. The in-plane position of the respective W (112) reflection is marked by a grey-dotted line for comparison.

also in these films. The corresponding in- and out-of-plane lattice spacing are determined from the reflection positions in reciprocal space by fitting 2D Gaussian peaks to the data. The obtained values are presented in Tab. 6.1 also in comparison to the in-plane lattice constants for the respective W layer. The adaptive nature

of the orthorhombic structure becomes evident when its (average) in-plane lattice constant is compared to the W lattice parameter, which is expressed as the residual misfit Δ presented in the right-most column of Tab. 6.1. This is especially true for the two near-equiatomic samples, while the $x = 0.72$ film has a slightly smaller value, indicating a reduced ability of the material to accommodate the large strain by forming the adaptive structure.

Fig. 6.3(b) finally proves that the $x = 0.78$ film has a bcc structure, therefore the axes are indexed according to the bcc notation with the c-axis as out-of-plane axis. The azimuthal directions are the same as in the graph above. The (112) reflection (which is the corresponding reflection in bcc notation to the (202), (220) reflections in $Cmcm$ notation) on the right hand side is not split, indicating an equiaxed crystal system. Its position yields ≈ 2.95 Å in- and out-of-plane lattice spacing, confirming the fully relaxed growth of this film [13, 57]. Moreover, the left hand side shows a featureless RSM measured in the region of reciprocal space where the $(221)_{Cmcm}$ reflection is expected (again under the same azimuthal angle as above), finally ruling out orthorhombic symmetry. Thus it can be stated that the adaptive orthorhombic martensite can be stabilized up to at least 72 at.-% Fe for the given epitaxial misfit and within the investigated film thickness.

6.4 Local structure and magnetic properties

Further insights into the local structure as well as in the magnetic state of the samples are obtained with ^{57}Fe Conversion Electron Mössbauer Spectroscopy (CEMS). Fig. 6.4 presents the spectra measured at RT: (a) for the samples $x \leq 0.72$ and (b) $x = 0.78$, respectively. The spectra of the samples with $x \leq 0.72$ can be fitted as a quadrupole doublet with a relatively narrow Lorentzian line width (Γ) of 0.28 mm/s. Both the isomer shift (δ) and the quadrupole splitting (ΔE_{Q}) decrease with increasing Fe content as shown in Tab. 6.2. Both trends are expected due to the continuous change of the local Fe environment. The decrease of ΔE_{Q} reflects the reduced local Fe site distortion, caused by a chemically more homogeneous nearest neighbor shell. The systematic change and the absolute value of δ as a function of x is in agreement with reports on disordered face centered cubic (fcc) alloys [12], which are, in terms of local structure, the closest bulk phase to the orthorhombic structure. This point relates to the discussion of the similarity of the $Cmcm$ structure to a close-packed-like local environment presented in Chaps. 4.4 and 5.2.2.

In contrast, the spectrum of the $x = 0.78$ sample (Fig. 6.4(b)), which has been shown to have a bcc structure, consists of a broadened magnetic sextet with an average magnetic hyperfine field $\langle B_{\mathrm{HF}} \rangle$ of 35 T (the data is fitted with a histogram

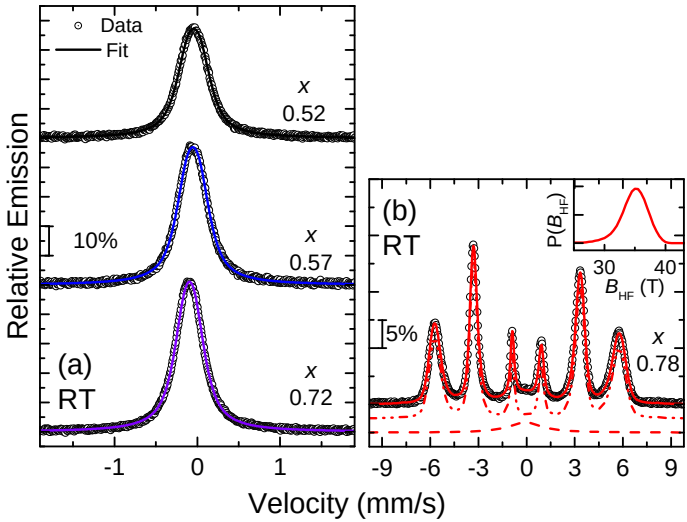

Figure 6.4.: RT-CEMS spectra measured, (a) for $x \leq 0.72$ and (b) for $x = 0.78$. The inset in (b) represents the distribution of magnetic hyperfine fields $P(B_{\mathrm{HF}})$ as a function of the magnetic hyperfine field B_{HF} used to fit the broadened sextet.

distribution of B_{HF} linearly correlated with δ) and an average $\langle\delta\rangle$ of 0.12 mm/s. The obtained $\langle B_{\mathrm{HF}}\rangle$ compares well to Shiranes report on the A2 phase with comparable composition, prepared by a martensitic transformation from the fcc-field [13]. The $\langle\delta\rangle$ observed for this sample is larger than what is reported in the work by Shirane, which finds a value of about 0 - 0.02 mm/s. The reason for this deviation might possibly be the slightly larger unit cell of the thin film sample, due to the minor tetragonal distortion, which results in a decrease in s-electron density and hence an increased value of $\langle\delta\rangle$. As it is known that chemical ordering also influences δ substantially [13], local chemical ordering may be another possible explanation. Besides the sextet, an additional subspectrum is needed to reproduce the measured data correctly, which is a broad singlet shown in the center of the spectrum ($\approx 8\%$ spectral area). Most probably this can be assigned to the first few FeRh layers, which grow fully strained, either pseudomorphically or in the orthorhombic structure, before the strain relaxation sets in.

CEMS spectra measured at 80 K of the samples $x \leq 0.72$ are presented in Fig. 6.5(a). Comparable to the RT data, they exhibit only a quadrupole doublet or singlet, which shows that the magnetic order is still quenched at this temperatures in the samples with $x \leq 0.72$, similar to the near-equiatomic sample presented in

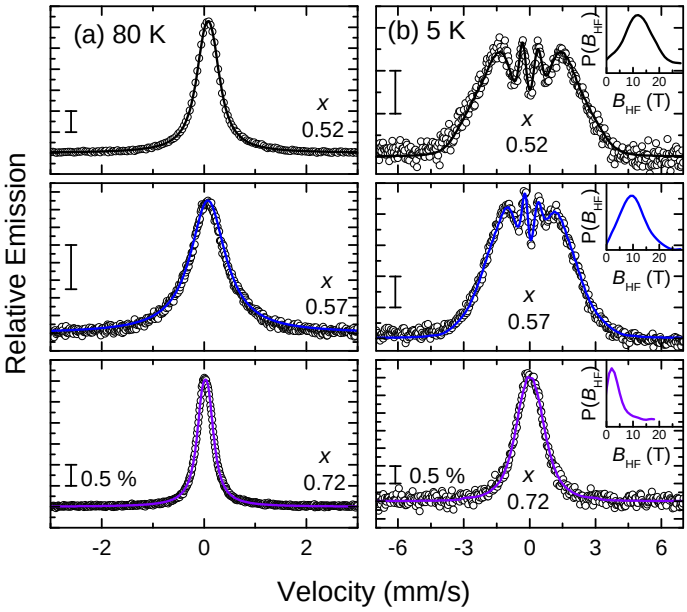

Figure 6.5.: CEMS spectra measured for the samples with $x \leq 0.72$ at (a) 80 K and (b) at 5 K. The inset in (b) represents the distribution of magnetic hyperfine fields $P(B_{\mathrm{HF}})$ as a function of the magnetic hyperfine field B_{HF} used to fit the broadened sextet.

Chap.4. Nevertheless it is noticeable that the spectra of $x = 0.52, 0.57$ display a quite different shape compared to the RT data. The spectra are discernibly broadened (see Γ in Tab. 6.2), whereas the sample $x = 0.72$ shows a perfect doublet with an essentially identical linewidth as compared to RT. Moreover, the spectrum $x = 0.57$ cannot be reproduced anymore with a doublet, but needs to be fitted with a broad singlet instead. This broadening cannot be of structural origin, as the RT spectra show no such anomalous feature for the sample series. Thus the broadening observed in the 80 K spectrum is attributed to the onset of correlated spin fluctuations at the spin freezing temperature (T_{f}) of the SG phase. Hence, T_{f} is slightly increased compared to the $x = 0.52$ sample (see Fig. 4.17 on page 59).

A possible explanation for this behavior can be found in the competition of FM Fe-Rh interaction and the frustrated AF exchange interactions between Fe-Fe pairs at longer distances. Thus a compositional dependence of the spin dynamics and spin freezing may be expected, given that more Fe nearest-neighbors enhance the

hybridization induced Rh spin-polarization and in turn the FM Fe-Rh coupling. Whereas the relative number of FM coupling Fe-Rh pairs gets reduced and additional frustrated, AF coupling Fe-Fe pairs appear. Possibly the first effect is still able to slightly enhance the effective exchange parameters in the $x = 0.57$ sample, while the latter takes over at around $x = 0.72$, which results again in a complete balance of FM and frustrated AF interactions at 80 K.

The spectra measured at 5 K for the three samples are presented in Fig. 6.5(b), together with their respective distributions of magnetic hyperfine field (B_{HF}), which are shown in the inset. From the data it is obvious that the splitting and the resulting $\langle B_{\mathrm{HF}} \rangle$ is decreasing with increasing Fe content x. This is in agreement with the earlier report on ball-milled fcc alloys of similar composition [15], again referring to the local structure similarities of strained thin films with a close packed arrangement.

Table 6.2.: Mössbauer hyperfine parameters, δ or CS, ΔE_{Q}, Γ, σ (all given in (mm/s)) and B_{HF} (in T) obtained by fitting the CEMS spectra. The RT spectrum of sample $x = 0.78$ and the 5 K spectra are fitted with a distribution of hyperfine parameters, the values given are thus average values. The values labeled with $^{\#}$ are fixed during the fit.

	x	δ/CS	ΔE_{Q}	Γ	σ	$\langle B_{\mathrm{HF}} \rangle$
RT	0.52	0.063(5)	0.148(5)	0.280(5)	0.25(1)	-
	0.57	0.053(5)	0.144(5)	0.280(5)	0.25(1)	-
	0.72	0.011(5)	0.120(5)	0.280(5)	0.24(1)	-
	0.78	0.12(3)	-	$0.28^{\#}$	-	35(2)
		$0^{\#}$	-	2.5(1)	-	-
80 K	0.52	0.184(5)	0.151(5)	0.435(5)	-	-
	0.57	0.181(5)	-	0.84(2)	-	-
	0.72	0.131(5)	0.121(5)	0.285(3)	-	-
5 K	0.52	0.100	0.05	-	-	13
	0.57	0.160	0.05	-	-	11
	0.72	0.134	0.00	-	-	5

Further macroscopic information on the magnetic state is obtained by Superconductive Quantum Interference Device (SQUID) magnetometry. Magnetization M results are given in Fig. 6.6(a) as a function of temperature T at constant external magnetic field $\mu_0 H = 50\,\mathrm{mT}$ and (b) versus $\mu_0 H$ at 30 K, respectively. Please note that the magnetization axis is broken in both figures for the sake of clarity. It is obvious that the overall magnetization of the two near-equiatomic samples is in both measurements vanishing. This is especially interesting since these samples revealed a sizable magnetic splitting of the 5 K CEMS spectra, which is evidence for the presence of local magnetic moments. The fact that it is obviously not possible to observe these magnetic moments with dc-SQUID magnetometry shows unequivocally that the magnetic exchange interactions must be highly frustrated and the spin configuration frozen at low temperature. Again, this behavior is in agreement with the findings in the structurally related fcc alloys [16] and it emphasizes the importance of the spectroscopic investigation with CEMS.

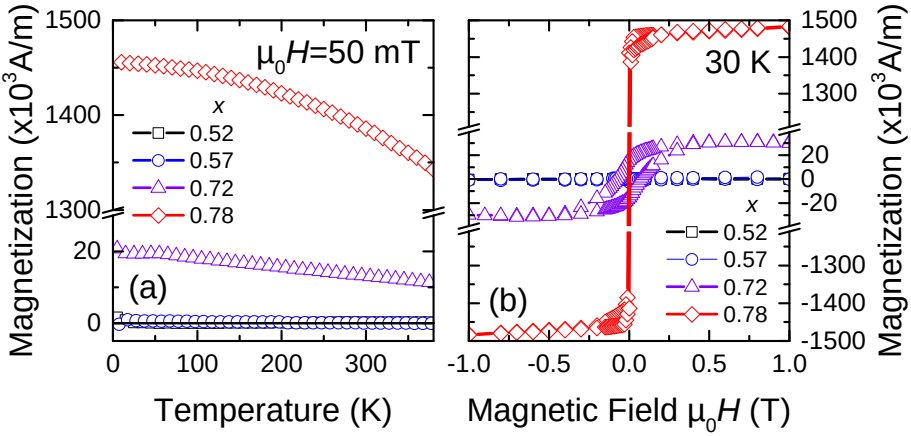

Figure 6.6.: Magnetization results for all four samples. (a) $M(T)$ FC curves at an external field of 50 mT. (b) $M(\mu_0 H)$ at $T = 30\,\mathrm{K}$. In both cases, the magnetization axis is broken in order to include the data from magnetic and (virtually) non-magnetic samples.

However, the Fe-richest *Cmcm* sample with $x = 0.72$ shows a small magnetic signal of about 20 - 25 kA/m, far less than the bcc sample with about 1450 kA/m. The latter value is in fair agreement with previous work on bulk A2- and B2-FeRh of that composition [1, 13] confirming the bulk nature of the observed magnetism.

Considering that a similar number would be also expected for $x = 0.72$ (if it were in the bcc structure) and that this sample showed also in the 5 K CEMS spectra no sign of magnetic splitting, it is evident that the small measured magnetization corresponds only to about 2% of the sample volume. This small magnetic contribution can be attributed to small lateral regions of the sample, which grew in the magnetic A2 structure. This is well possible, as the investigation with RSMs has shown (see Fig. 6.3(a) and Tab. 6.1) that the adaptive lattice constant of the $x = 0.72$ sample is reduced by -1.6% compared to the W buffer layer. So, despite the adaptive structure, some local lattice defects, e.g. misfit dislocations, must be present in the material. These local areas, where the FeRh is decoupled from the W lattice beneath, might act as nucleation sites for the A2 structure, which is then magnetic. However, considering the small relative part of the magnetic signal, we can confirm the above discussed CEMS[1] results, which show only a weak or rather no discernible magnetic splitting down to 5 K.

6.6 Discussion

In conclusion of this chapter it can be stated that the discovered epitaxial strain-induced martensitic lattice instability in equiatomic disordered FeRh thin films can also be sustained in alloys with a greatly increased Fe content. HRXRD on symmetric and asymmetric reflections clearly shows that thin films with $x \leq 0.72$ grow in the orthorhombic martensite structure, while a sample with slightly higher Fe content of $x = 0.78$ grows fully relaxed in a bcc structure. This can be understood by considering the fact that the underlying cause of the lattice instability is found in an energetically unfavorable feature in the partial Rh-DOS, discussed in Chap. 4.5. With the reduced Rh-content this contribution to the total energy becomes less important, until it is no longer able to trigger the stress-relieving martensite transformation. At that point regular strain relaxing processes set in, such as misfit dislocations, which results in a thin film with basically bulk structure and magnetic properties. The composition of about 78 at.-% Fe, at which the thin films are growing fully relaxed in a bcc structure compares to the composition for which a martensitic transition to the A2 phase has been achieved in the bulk by quenching from the fcc-field [13]. This suggests that the metastability of the disordered bcc and bct phases is linked, in the bulk as well as in the strained thin films, to the electronic features observed in the Rh-DOS.

[1] Such a minor magnetic phase of 2% spectral area is not observable in the CEMS measurement as the integral intensity of that magnetic subspectrum is spread over the six-lines of the sextet, eventually vanishing in the noise.

These observations provide experimental evidence that the orthorhombic martensite structure is at the basis of the prevailing magnetic ground state. For instance, the samples $x = 0.72$, 0.78 differ only negligibly in terms of composition, whereas they have entirely different structures and hence magnetic properties. Despite their different chemical compositions, the two structural and magnetic states can be seen as end points of the hypothetical transformation path from bcc $\rightarrow Cmcm$ proposed and discussed in Fig. 4.14 on page 56.

It is interesting that, at least in the investigated thickness range, the transition from the strained adaptive structure to the fully relaxed growth, is rather abrupt. Furthermore, one should remember that the total energy of the real bilayer also includes the interfacial energy, which of course favors or forces the adaptive structure in the first place, as seen in Chap. 5. Therefore, one more natural degree of freedom, inherent to the bilayer system, is the imposed epitaxial misfit. This will be the focus of the following Chap. 7.

7 Alloy buffer layers: Tailoring the epitaxial boundary condition

The preceding Chapts. 4 and 5 have illustrated the importance of the epitaxial boundary condition for the resulting structure and nanostructure of the FeRh thin films. This straightforward relation may provide a strategy for effective tailoring of their functional magnetic properties towards potential applications. Indeed, the use of W-V alloy buffer layers, enabling the precise adjustment of the epitaxial strain, allows strain-engineering of novel self-assembled magnetic nanostructures.

In the course of the investigation it was found that the careful choice of the deposition temperature plays a decisive role for the formation of the self-assembled nanostructures. Therefore the present chapter is organized into two major sections, first considering bilayers with the FeRh films deposited at ambient temperature, then films grown at 300 °C are presented and discussed.

7.1 Room temperature growth: Metastable adaptive structures

The first set of experiments investigates the structure of FeRh films deposited at room temperature (RT) on $W_{1-z}V_z$ buffer layers, it therefore displays a natural continuation of the experiments presented in Chap. 4.

7.1.1 Sample preparation details

The $W_{1-z}V_z$ buffer layers were prepared according to the procedure described in Chap. 3.6.3 on page 31. Five samples are presented here, with the buffer layer composition ranging from pure W to pure V. Again the sample on pure W is the same as in Chap. 4.

As it was found in Chap. 6 that the Fe_xRh_{1-x} composition, at least close to the equiatomic value, has no dramatic impact on the resulting structures, small variation in FeRh composition within the sample series could be accepted. Hence, the (near)-equiatomic FeRh layers were deposited subsequently, using co-evaporation of ^{57}Fe and Rh, explained on page 34, allowing for the more straightforward growth of thicker films. The growth was monitored using Reflection High Energy Electron

Table 7.1.: (a) Results of chemical analysis of the $W_{1-z}V_z/Fe_xRh_{1-x}$ bilayers deposited at RT. (b) Results of XRR and HRXRD, presenting the thickness t of both layers, the out-of-plane lattice constant of the FeRh layer a' and the in-plane lattice constant a_{WV} of the buffer layer.

(a) EDX		(b) XRR		HRXRD	
z	x	t_{FeRh} (nm)	t_{WV} (nm)	a' (Å)	a_{WV} (Å)
1.00	0.57(5)	12.5	54	2.672(2)	3.014(5)
0.70(5)	0.58(5)	11.3	42	2.672(2)	3.030(5)
0.57(5)	0.44(5)	8.6	43	2.680(2)	3.066(5)
0.32(5)	0.44(5)	8.0	51	2.680(2)	3.108(5)
0.00	0.52(3)	13.0	50	2.655(2)	3.151(5)

Diffraction (RHEED), which already provided information on the epitaxial character of the grown bilayers (not shown). The composition of both, buffer layer and FeRh thin film, were determined with Energy-Dispersive X-ray Spectroscopy (EDX) and the obtained results are given in Tab. 7.1(a) together with other basic properties such as film thicknesses and the lattice constants of the buffer layers.

The samples presented in the following have been comprehensively investigated using HRXRD, Conversion Electron Mössbauer Spectroscopy (CEMS) and Superconductive Quantum Interference Device (SQUID) magnetometry. For the sake of clarity only the relevant results are shown, those which displayed a significant variation as a function of the in-plane buffer layer lattice spacing.

7.1.2 Structural characterization

XRR patterns of the five samples are presented in Fig. 7.1. The observed Kiessig oscillations with different periodicity can be attributed to the two different layers of the heterostructure. A clear distinction between the oscillation stemming from the individual metal layers becomes difficult for the intermediate samples. This is related to the difference in (electron) density between the two layers, which is vanishing for the intermediate $W_{1-z}V_z$ compositions, resulting in a strongly reduced scattering contrast, e.g. for the sample with $z = 0.7$.

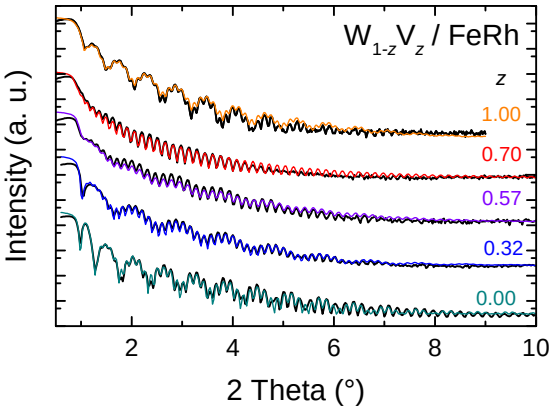

Figure 7.1.: XRR patterns of FeRh/$W_{1-z}V_z$ bilayers grown at RT. The obtained thicknesses of the respective layers are given in Tab. 7.1(b).

The results of the structural investigation with HRXRD are presented in Figs. 7.2 and 7.3, displaying standard $\theta/2\theta$ measurements and Reciprocal Space Maps (RSMs) of asymmetric reflections, respectively. The $\theta/2\theta$ diffraction patterns lead to an interesting finding: the position of the reflection attributed to the FeRh layer is virtually not changing with the composition of the buffer layer. This is a rather unexpected behavior of the FeRh layers, as in-plane and out-of-plane lattice constants are usually linked; hence an influence would have been expected in some form. Moreover, the lattice parameter values corresponding to the 2θ position range around the lattice constant obtained for the FeRh films on W in the $Cmcm$ martensite phase, as can be seen from the obtained lattice constants a' given in Tab. 7.1(b). However, no trend associated with the variation of the in-plane lattice constants of the buffer layers a_{WV} is observed.

This unexpected observation is further investigated employing RSMs shown in Fig. 7.3. For reference and comparison: these are the same reflections, in a similar range of reciprocal space, as already presented in the previous chapters in Fig. 4.7 on page 45 and Fig. 6.3 on page 81. The (221), which is a reflection not present for a body centered cubic (bcc) or body centered tetragonal (bct) structure, is shown in the left panels, while the (220), (202) pair is plotted in the right panels. The latter would have a counterpart in the cubic structures, while the splitting is a sign of the different in-plane lattice constants and the orthorhombic structure, as discussed extensively in Chap. 4.4 on page 45.

The presence of the (221) reflection for all samples unambiguously proves that they all have a structure with crystallographic symmetry lower than tetragonal.

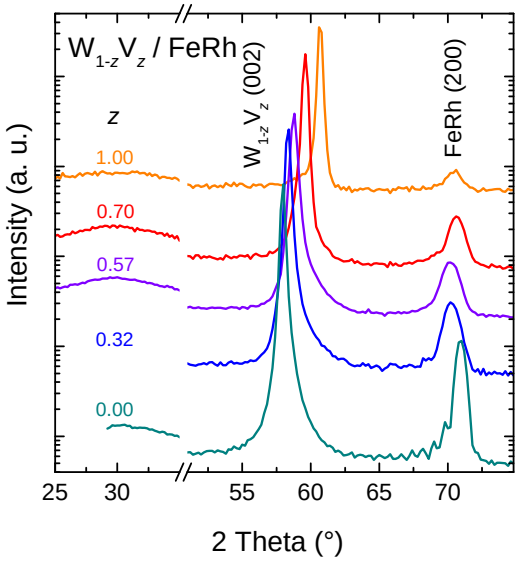

Figure 7.2.: HRXRD patterns of FeRh/$W_{1-z}V_z$ bilayers grown at RT. The determined FeRh out-of-plane lattice parameters a' are given in Tab. 7.1(b).

Judging by the observed lattice constant it is most probably the orthorhombic $Cmcm$ structure. Furthermore, the center position of the reflections in reciprocal space does not decisively change with $W_{1-z}V_z$ composition. In contrast, what is changing dramatically is the width of the reflection. With decreasing in-plane lattice constant it becomes increasingly smeared out. This broadening is oriented approximately perpendicular to the scattering vector q, as indicated by the white bar in the topmost panel, perpendicular to q. Hence, the broadening corresponds to a mosaic spread of the crystal planes, i.e. a tilting of the unit cells [123]. This information is intrinsically directional, that means it actually shows a mosaic spread, or tilting of the planes in the direction of the in-plane components of the chosen reflection $< h21 >$, which was selected by the azimuthal orientation ϕ of the sample.

In order to be able to distinguish whether the observed mosaicity is isotropic or itself directional (meaning that the crystals or domains are tilted in certain specific crystallographic directions), it is necessary to investigate reflections with different in-plane orientations. Indeed the measurement of the (220), (202) pair of reflections presented in the right panel of Fig. 7.3, provides evidence for directional (or anisotropic) tilting. It is obvious that with decreasing lattice constant of the buffer layer (indicated by the white dotted bar), starting from pure W, the (220) reflection

progressively smears out to an extent that only a diffuse intensity distribution remains. In contrast, the (202) reflection remains well defined, with only little broadening. These observations may be interpreted as follows.

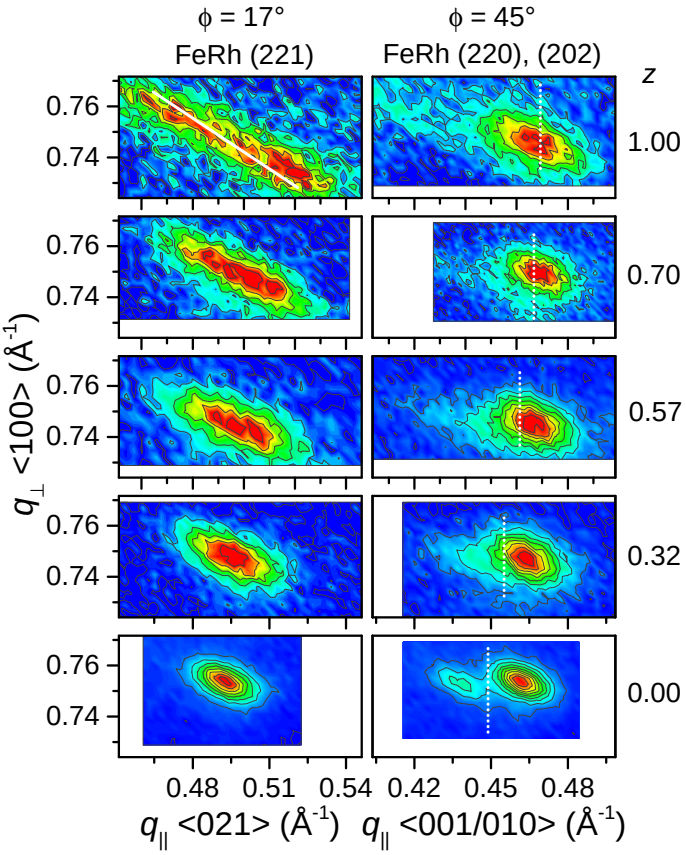

Figure 7.3.: RSMs of FeRh/$W_{1-z}V_z$ bilayers grown at RT. The left panels present measurements of the $(221)_{Cmcm}$ reflection, with decreasing in-plane lattice spacing the reflection becomes smeared out. The white bar is perpendicular to the scattering vector q indicating that the broadening corresponds to an enhanced mosaicity. The right panels show the evolution of the (220), (202) reflection pair. The (220) is smearing out entirely towards the V-rich buffer layers, while the (202) remains well defined.

The broadening of the (220) reflection indicates that in this particular crystallographic (in-plane) direction namely along the b' the tilting is strongest, while the lattice along the c' axis is undisturbed. The (221) reflection, having an in-plane component in both directions, shows hence also the signs of tilting but not to the extent as the (220) reflection. Furthermore, the (221) intensity plot can be further analyzed unraveling that it actually consists of two overlapping maxima, which can be fitted with two 2D Gaussian peaks as shown in Fig. 7.4(a). This is an important observation as it implies a well defined tilt angle between the two crystallographic domains. In principle this should be also observed in rocking curves of symmetric reflections as a function of the in-plane rotational orientation ϕ. Fig. 7.4(b) displays the rocking curves of the reflection coming from the FeRh (200) planes for an azimuthal angle ϕ of 45°, hence parallel to [010], [001] directions (see orientation relations in the sketch in Fig. 7.4(c)). Indeed the $\phi = 45°$ measurement shows a strong broadening and the curve can be deconvoluted into three peaks: the two outer ones corresponding to the domains tilted in this azimuthal direction (labeled 1 and 2). They are thus shifted from the center position, while the center peak corresponds to the domains oriented in perpendicular in-plane direction (labeled 3). From the position of the outer peaks a maximum tilt angle of $\alpha \approx 4.2°$ can be determined.

Moreover, the observation that the structural domains are tilted in b' direction, which can also be seen as a rotation of the domain orientations around the c' axis, is very intriguing, given that the c' axis has been identified as the pseudo-hexagonal close packed (hcp) axis of the *Cmcm* structure (see discussion in Chap. 4.4 on page 45). Whereas the c' axis itself is, as evidenced by the RSMs, not affected from the tilting and remains parallel to the film plane.

However, despite these distinct changes in the (nano-)structure of the adaptive martensites, the local structure is not modified drastically as found by the investigation with CEMS. The obtained spectra (not shown) are basically not changing throughout the sample series, and they can always be represented with a narrow quadrupole doublet with a quadrupole splitting (ΔE_Q) of 0.15 - 0.17 mm/s and an isomer shift (δ) of ∼0.06 mm/s. This supports the hypothesis obtained from the analysis of the HRXRD results, that the FeRh films remain very close to the already described *Cmcm* martensite structure. Similar results are obtained by SQUID magnetometry, yielding no measurable magnetization down to low temperatures, just as the samples on pure W.

7.1.3 Discussion

Directional tilting of epitaxial layers has been already described in the literature as a strain or epitaxial misfit relaxation process [124]. It has been observed in the heteroepitaxy of e.g. ferroelectric materials [125, 126] but as well in compound semiconductor thin films [127]. However, in the case of the present FeRh thin films, it is not immediately apparent why such a mechanism is appearing.

The discussion begins with the sample on pure W: as was already mentioned in Chap. 4 on page 40, the disordered bcc A2 phase has the closest lattice spacing to the W buffer layers (+6%), while for the A1 phase with face centered cubic (fcc) symmetry there exists a huge epitaxial misfit (f) of ≈+20%. That is why the A2 phase was chosen as a reference for the films grown on W presented in Chap. 4. Hence it is clear that the system avoids the thermodynamically unfavorable A2-like bct phase by growing in the seemingly more stable pseudo-close packed $Cmcm$ structure. In the case of the W-V buffers, the in-plane lattice parameter is reduced, so that the epitaxial misfit for the metastable A2 phase is getting smaller, reaching +1%. From this purely geometrical consideration, one thus expects a stabilization of the A2 phase on the V-rich and pure V buffer layers. However the thermodynamic suppression of this phase [62], which was already discussed in Chap. 2.2, is so strong, that even films grown on MgO having virtually zero misfit to the A2 phase, crystallize in the A1 phase instead [19, 20], despite the drastic misfit of about +12%. These huge strains are certainly not accommodated by elastic deformation of the lattice. Hence the films grow in a fully relaxed way, entirely loosing the direct connection between substrate and film in-plane lattice spacings, despite the energetic cost of an increased interface energy due to a considerable number of defects and misfit dislocations [20].

Moving now from the $Cmcm$ structure on pure W to the V-rich buffer layers, it seems that the system tries to remain in this pseudo-close packed arrangement. But along with decreasing lattice constant of the buffer layer, this crystallographic structure is not able to entirely adapt to the preset lattice constant anymore. This is mostly because of the longer b' axis, while the shorter c' lattice parameter is becoming closer to that of the buffer layer, until both completely converge. This is illustrated by the overlap of the white dotted bar (in-plane position of the buffer layer reflection) with the position of the (202) reflection in the case of the pure V sample. However, the misfit in the b' direction drastically increases, which eventually is the reason for the observed directional tilting of the layer along b'. A tentative sketch of the nanostructure, including yet another variant of the crystallographic domains, namely the tilting, is shown in Fig. 7.4(c). In the graph each peak in the RSM is referred to one (arbitrarily chosen) orientation of the tilted domains. The

figure also illustrates the tilt angle α between the domains, which corresponds to a rotation of the lattice planes around the c'-axis. The habit planes between the

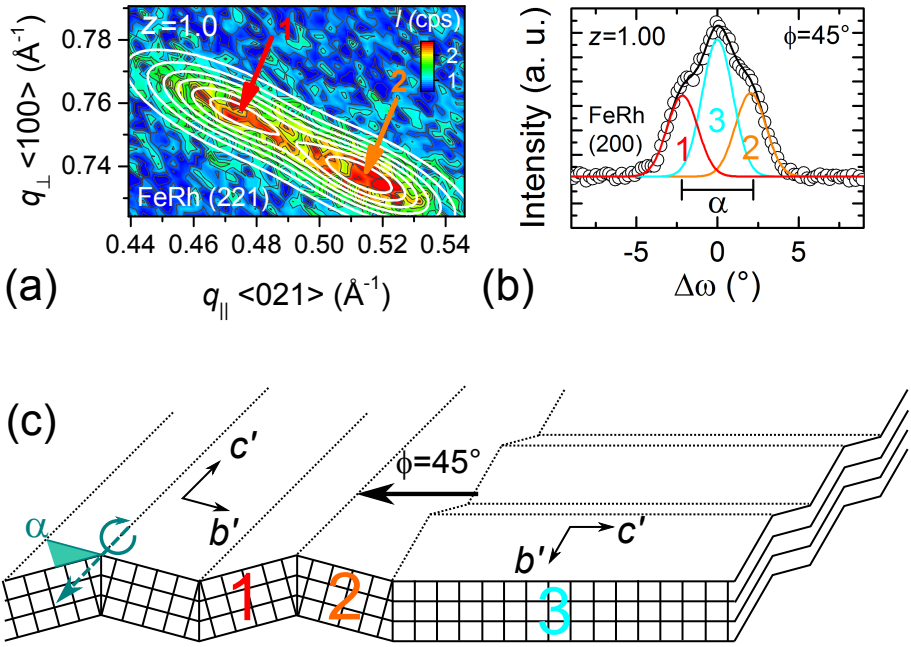

Figure 7.4.: (a) RSM of the FeRh(221) reflection for the film grown on pure V. The broad reflection can be reproduced with two Gaussian peaks, indicating that the structural domains are tilted with a well defined tilt angle against each other. (b) Rocking curve of the FeRh (200) reflection, measured with an azimuthal angle ϕ of 45°. The data can be fitted with three individual Gaussian peaks (identical width). The labeling relates them to the differently oriented domains shown in (c), which presents a sketch of the proposed adaptive nanostructure, including on top of the 90° in-plane rotated variants, also the additionally tilted domains along the b' direction. They can be attributed to the three components observed in the rocking curve. The tilt angle α is also drawn, while the tilting is exaggeratedly displayed, the real α is $\approx 4.2°$. The interfaces or habit planes between the domains are drawn with dotted lines. This is meant to indicate that the real habit planes cannot be identified, only the orientation of the crystalline domains is known. See text for more details.

tilted and in-plane rotated domains have not been identified, therefore they are only indicated by the dotted lines.

Interestingly, the present FeRh thin films on the V and V-rich alloy buffer layers behave entirely different compared to the literature results on chemically disordered FeRh thin films deposited on MgO, which were cited above [19, 20]. This divergent behavior may be qualitatively understood by considering the different thin film interfaces and the different nature of bonding between substrate or buffer and FeRh layer. The growth of Fe on MgO is known to happen on the oxygen sublattice [128, 129]: hence the first layer of the metallic FeRh thin films is tightly bound due to the covalent and thus directional nature of the bonding. In contrast, on the metallic buffer layer the bonding is of metallic kind, which is less directional and may therefore allow for the sizable local misfit between the cubic and orthorhombic lattice. This misfit has been already identified as an important factor in the thickness dependent structural behavior of the FeRh thin films on W, which were discussed in Chap. 5. The much stiffer interface between MgO and FeRh presumably does not allow for these local displacements and so the large misfit leads to a strain relaxation via misfit dislocations as reported. This illustrates that the adaptive properties of the FeRh lattice also crucially depend on the nature of the heteroepitaxial interface.

In summary, the results of this systematic investigation show that the *Cmcm* structure can be stabilized over a wide range of in-plane lattice parameter due to yet another adaptive mechanism, namely the observed buckling or tilting of the lattice in direction of the longer in-plane axis b', and this leads to a reduced misfit in this particular direction. Furthermore they illustrate that the adaptive structures not only allow to accommodate the strain, but also display a possibility for the system to avoid the thermodynamically unfavorable A2 phase, despite the preset lattice parameters, which clearly would favor the latter phase.

Referring to Chap. 5, where a distinct evolution of the structure, from bct $\rightarrow$ *Cmcm*, with increasing film thickness for FeRh on W buffer layers was observed, one can speculate whether the FeRh films grown on the V- or V-rich alloy buffer layers might behave in a similar way. In this scenario one possibly expects a transition from a ferromagnetic (FM) to a paramagnetic (PM) state (at RT) with increasing film thickness.

Similarly it would be interesting to grow Fe_xRh_{1-x} films again on W-V buffer layers, but now at the border of the critical composition region with $x \approx 0.72$. Here the *Cmcm* structure can still be stabilized on W, as was found in Chap. 6, while the stable composition of the bcc structure is very close ($x \approx 0.78$). It might be expected, given the supposedly rather flat structural energy-landscape in this composition range, that it is possible to obtain a continuous evolution of the FeRh structure between the two structural end points bcc on V $\rightarrow$ *Cmcm* on W. In

principle, this would represent an experimental realization, albeit with a different composition, of the hypothetical transformation path presented and discussed in Fig. 4.14 on page 56.

These questions and the proposed experiments remain open and may inspire future experimental and theoretical studies.

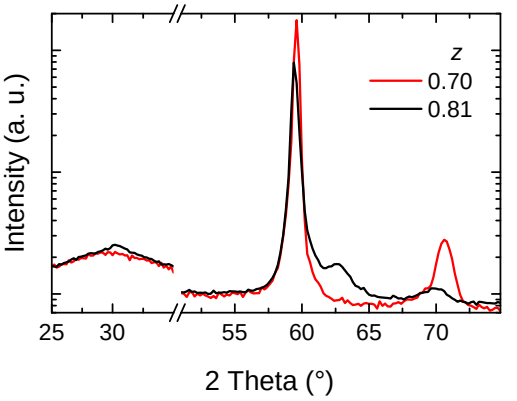

Figure 7.5.: HRXRD pattern of FeRh/$W_{1-z}V_z$ bilayers with $z = 0.7, 0.81$ grown at RT. The diffraction pattern gives evidence for a different structure of the FeRh layer, despite the similar preparation and buffer layers, which can be taken as a sign for the metastable nature of the FeRh structure.

As an outlook and motivation for the second part of this chapter, Fig. 7.5 shows that the FeRh thin films deposited on W-V buffer layers are highly metastable. The $\theta/2\theta$ patterns obtained for two samples deposited on very similar buffer layers under similar conditions (RT) are presented. The first diffraction pattern yields the well known result of the $Cmcm$ structure, while the other displays an entirely different shape. The familiar $Cmcm$ reflection is replaced by two small reflections, thus indicating distinct structural differences.

7.2 Phase separation at elevated growth temperature

The above observed metastability of the FeRh structure on the $W_{1-z}V_z$ buffer layers might imply a certain kinetic sensitivity. Therefore the growth temperature is expected to have a decisive influence on the final structures, which is discussed in the following.

7.2.1 Sample preparation details

The $W_{1-z}V_z$ buffer layers were prepared according to the procedure presented in Chap. 3.6.3 on page 31. Three samples are discussed here, with their buffer layer composition ranging from pure W to a V-rich alloy. Growing Fe layers on top of pure V at elevated temperatures is known to lead to interdiffusion [130, 131], while RT growth results in sharp interfaces [132]. For this reason this study was limited to V-rich $W_{1-z}V_z$ buffer layers.

The FeRh layers were deposited by co-evaporation at 300 °C and then capped with a 1 nm Rh layer. Thus, the only relevant difference between the two sample series is the deposition temperature of the FeRh layer. Just as in the other experiments the growth was monitored using RHEED, providing evidence for the epitaxial growth of the buffer layers and the FeRh thin film (not shown). The composition of both, $W_{1-z}V_z$ buffer layers and FeRh thin films, were determined with EDX and the results are given in Tab. 7.2(a).

7.2.2 Structural characterization

High-Resolution X-ray Diffraction (HRXRD) patterns and RSMs of asymmetric FeRh reflections are presented in Fig. 7.6(a), and (b), respectively. The main reflection in the diffraction patterns in Fig. 7.6(a) corresponds to the $W_{1-z}V_z$ buffer layer, which shifts, as expected, with increasing V content z to higher angles and lower lattice constants.

The FeRh reflection observed for the $z = 0$ sample is attributed to the $(200)_{Cmcm}$ planes of the orthorhombic structure (a'-axis is normal to the film plane as explained in Chap. 4.4) [95]. Again the absence of a first order reflection points out the disordered nature of the structure even at 300 °C growth temperature. In contrast, for the film on the V-rich alloy with $z = 0.75$ a reflection at much lower angles is observed, corresponding to a 2.944 Å lattice spacing, which is attributed to the (002) planes of a bcc or bct structure (c-axis pointing in the out-of-plane direction). The presence of the first order reflection at lower angles for this sample, indicates at least partial chemical ordering in a B2-structure. Surprisingly, the intermediate sample $z = 0.57$ presents features of both structural phases, suggesting a phase separation into the two competing structures in the intermediate strain regime. The reduced intensity and increased broadening of the reflections are possibly the result of the finite size of the structural motives, an enhanced mosaicity, and a general distribution of structural parameters.

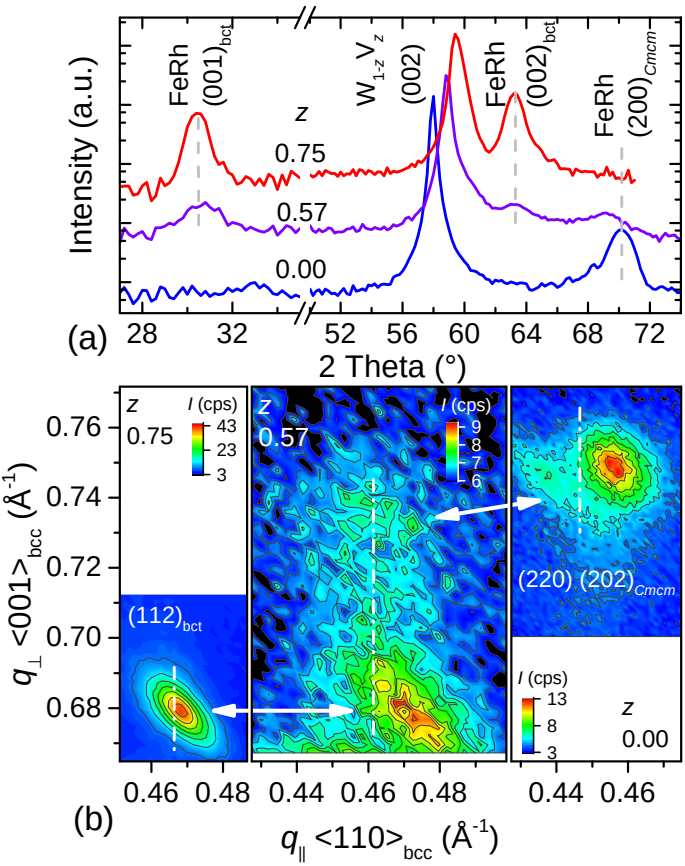

Figure 7.6.: (a) HRXRD pattern showing the out-of-plane reflections of the $W_{1-z}V_z$ and FeRh layers. The FeRh reflection for $z = 0$ is attributed to the $(200)_{Cmcm}$ of the orthorhombic structure, while the sample $z = 0.75$ shows reflections typical for a (partially) B2-ordered alloy. The intermediate sample presents features of both structural phases. This is supported by RSMs presented in b), measured with the in-plane scattering vector $q_{||}$ along $<110>_{bcc}$. For $z = 0$ (rightmost panel) a split reflection is observed, typical for the adaptive *Cmcm* structure [95], while $z = 0.75$ (leftmost panel) reveals a single intensity maximum which is attributed to a bct structure. The intermediate sample (center) presents features of both structures, as indicated by the arrows. The dash-dotted lines indicate the position of $q_{||}$ of the buffer layer.

This interpretation is supported by the RSMs presented in Fig. 7.6(b). Here the in-plane scattering vector $q_{||}$ points along the <110> direction of the cubic buffer layers, while the dash-dotted line in all RSMs indicates the $q_{||}$ position of the respective buffer layer reflection. The obtained crystallographic information is summarized in Tab. 7.2 (in-plane lattice spacings of the buffers are also obtained from RSMs, not shown). For $z = 0$ (rightmost panel) a split reflection is observed, typical for the two in-plane directions of the adaptive orthorhombic $Cmcm$. The two reflections can be attributed to the $(202)_{Cmcm}$ and $(220)_{Cmcm}$ planes. The existence of both reflections in the same azimuthal direction results from the adaptive nano-twinned martensite, which features 90° rotated domains. The epitaxial relation is then $FeRh_{Cmcm}(100)[010/001] \parallel W(001)[110]$. The opposite RSM for the sample $z = 0.75$ shows a single maximum which is attributed to a bct structure, given the tetragonal distortion of the lattice (see Tab. 7.2(b)), which results from the in-plane misfit and the pseudomorphic growth, yielding the epitaxial relation $FeRh_{bct}(001)[110] \parallel W(001)[110]$. This finding confirms the fully strained growth of the FeRh film on the buffer layer in this thickness and strain regime.

Table 7.2.: (a) Results of chemical analysis of the $W_{1-z}V_z/Fe_xRh_{1-x}$ bilayers. (b) WV and FeRh lattice constants of the two structural phases determined from RSMs, all given in (Å). Δ is the residual epitaxial misfit between the $W_{1-z}V_z$ and the respective FeRh lattice in [100] direction of the buffer layer. For the *Cmcm* phase it refers to $\Delta = (\sqrt{{b'_{FeRh}}^2 + {c'_{FeRh}}^2} - 2a_{WV})/2a_{WV}$, while for the bct phase it is $\Delta = (a_{FeRh} - a_{WV})/a_{WV}$. The value of a_{WV} is obtained from the (112) reflection (not shown). $^{\#}$ denotes the lattice constant in the out-of-plane direction.

(a) EDX		(b) HRXRD					
z	x	a_{WV}	Phase	a' $^{\#}$ / $c^{\#}$	b' / a	c'	Δ
0.00(0)	0.50(5)	3.167(2)	*Cmcm*	2.678(2)	4.587(5)	4.384(2)	+0.1(1)
0.57(5)	0.50(5)	3.067(5)	*Cmcm*	2.708(5)	4.457(10)	4.276(10)	+1.5(5)
			bct	2.955(5)	3.005(5)		-1.9(2)
0.75(5)	0.57(5)	3.033(5)	bct	2.944(2)	3.021(5)		-0.4(1)

Further evidence of phase separation in the intermediate sample ($z = 0.57$) is presented in the middle panel of Fig 7.6(b). The observed diffraction features can be related to the structural phases already identified in the two boundary samples, indicated by the arrows in Fig. 7.6(b). The orthorhombic splitting of the $(202)_{Cmcm}$ and $(220)_{Cmcm}$ reflections is barely visible. Nevertheless, a slight shoulder can be observed on the lower $q_{||}$-side of the reflection, indicative of the orthorhombic distortion, which permits the determination of the lattice constants with a two peak fit to a $q_{||}$-cross section (not shown). However, the bct reflection found at smaller $q_{\perp}$ is more pronounced and it is shifted to smaller in-plane lattice spacings, compared to the $Cmcm$ peak, but also in relation to the underlying W-V buffer layer.

The individual, residual epitaxial misfit of each phase to the buffer (Δ) is shown in Tab. 7.2(b). It clearly evidences that both phases share the strain, in the intermediate regime, by adapting a lattice constant closer to that of their equilibrium structure. These observations suggest that strain is the driving force promoting phase separation and at the same time they point out the adaptive nature of the nanostructure. Here it should be noted that this phase separation phenomenon represents a novel epitaxial stress relaxation process not only with respect to the standard case of defect incorporation (misfit dislocations) but also by reference to the already mentioned nano-twinned adaptive martensites [23, 95].

7.2.3 Spectroscopic characterization

Unequivocal support for the phase separation model is provided by CEMS, spectroscopically probing the local surrounding of the ^{57}Fe nuclei in the film. Fig 7.7 displays CEMS spectra measured at ambient temperature; the obtained hyperfine parameters are summarized in Tab. 7.3.

For $z = 0$ only a singlet is observed, indicative of a PM state. The line broadening indicates a small quadrupole effect. This is in agreement with the samples prepared at RT, which have been discussed in Chap. 4. For $z = 0.57$ an additional feature appears in the CEMS spectrum. A clear magnetic splitting is observed, while the remaining single line is reproduced by a broadened singlet. The broadening possibly reflects a distribution of local structural environments. The sextet with a spectral area of about 40% is attributed to the bct phase in the thin film, which is expected to be magnetically ordered, considering the magnetic properties of the bulk-phases [13].

The assignment of the sextet to the bct phase is further reinforced by the spectrum obtained for the $z = 0.75$ sample (having, according to HRXRD, the bct structure), which shows mainly the presence of a sextet with only a minor singlet

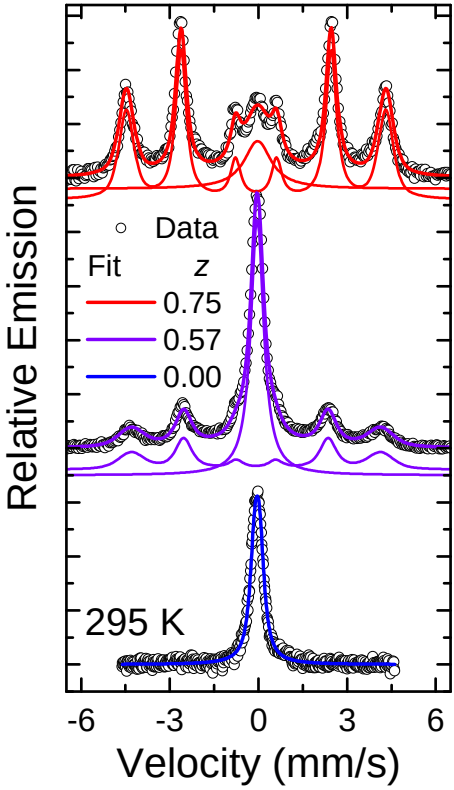

Figure 7.7: RT-CEMS spectra for the sample series. The data can be fitted with a sextet corresponding to the ferromagnetic bct phase and a singlet attributed to the (at RT) PM *Cmcm* phase.

component (≈22% spectral area). The singlet probably originates from residual $Cmcm$ phase, which is not detected in the HRXRD measurements due to its smaller fraction in the $z = 0.75$ sample and possibly also because of its small crystallite size, ultimately broadening the reflections. The δ and B_{HF} for the sextets in the $z = 0.57$, 0.75 samples agree with what has been reported about the B2-ordered phase in FeRh [13], while the observed ΔE_{Q} and δ for sample $z = 0$ compares well to the values we previously reported for the $Cmcm$ phase grown on pure W at RT [95]. Hence, the CEMS results entirely support the two phase model proposed above and they even provide additional crucial information by resolving and attributing two distinctly different magnetic states to the two structural phases.

Table 7.3.: Mössbauer hyperfine parameters obtained from fitting the RT-CEMS spectra. δ, ΔE_Q and Γ are all given in (mm/s) while B_{HF} is provided in (T). Area denotes the relative spectral fraction of the subcomponents.

z	Phase	δ	ΔE_Q	B_{HF}	Γ	Area
0.00	$Cmcm$	0.063(1)	0.17(1)	-	0.35(1)	1
0.57	$Cmcm$	0.064(1)	-	-	0.52(1)	0.59(5)
	bct	0.016(3)	-	26.5(35)	0.60(1)	0.41(5)
0.75	$Cmcm$	0.072(7)	-	-	1.11(2)	0.23(5)
	bct	0.025(2)	-	27.2(20)	0.40(1)	0.77(5)

7.2.4 Microscopic characterization

The co-existence of both phases in the $z = 0.75$ sample, which was evidenced by CEMS, was further investigated using High-Resolution Transmission Electron Microscopy (HRTEM) at atomic resolution. Fig. 7.8 summarizes the obtained results. The cross section Focused Ion Beam (FIB) lamella was prepared with its normal parallel to the [110] directions of the bcc lattice of the buffer layer and the FeRh bct phase, which corresponds to the [010] or [100] directions of the $Cmcm$ lattice (45° rotation of the unit cell). The high-resolution image in Fig. 7.8(a) proves the epitaxial growth of the film and it features pronounced Moiré fringes, evidencing the presence of two different crystalline lattices with slightly different periodicity throughout the thickness of the lamella. Moreover the representative Fast Fourier Transform (FFT) pattern shown in Fig. 7.8(b) can be indexed and the reflections can be assigned to the two phases previously identified in HRXRD measurements. The splitting of the out-of-plane reflections into two spots clearly indicates the presence of two different out-of-plane lattice constants (highlighted by the circle), of about 2.68 Å and 2.94 Å for the $Cmcm$ and bct phase, respectively. The difference in in-plane lattice spacings can not be distinguished as the corresponding features in the FFT are lying very close and are smeared out. The FFT shows the presence of (001) and (111) reflections for the bct phase, which evidences its B2 ordering on a local scale as well, in agreement with the HRXRD data. The pattern assigned to the $Cmcm$ phase is essentially similar to the one obtained for the RT growth of FeRh on pure W buffer layers presented in Chap. 4 in Fig. 4.11 on page 51.

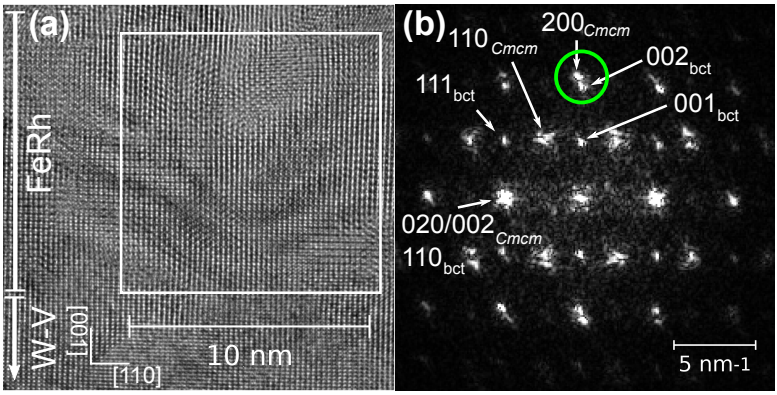

Figure 7.8.: Results of HRTEM investigation performed on a FIB lamella cut from the $z = 0.75$ sample. (a) HRTEM micrograph and (b) FFT of the sketched region, unambiguously showing the presence of two different out-of-plane lattice spacings attributed to the bct and *Cmcm* phase, which is highlighted by the circle.

An attempt to investigate the FeRh nanostructure also in the case of the $z = 0.57$ sample was not successful. A possible explanation is found in the sensitivity of the B2-phase to energetic ion-bombardment, as it was shown that high energy Ga-ion beams can transform B2-FeRh to the disordered A1 phase [64]. The delicate arrangement and nanosize of the B2 domains in the $z = 0.57$ sample in comparison to the $z = 0.75$ sample make them possibly more prone to this ion-beam induced transformation occurring during the preparation of the lamella by FIB.

As an alternative and non-invasive approach to gain insights into the lateral distribution of the two phases, freshly prepared samples were investigated *in situ* with STM. Fig. 7.9 shows a constant-current image of a sample in the intermediate lattice constant range (here $z = 0.5$), while the inset presents the surface morphology of a bct sample (here $z = 0.75$, same lateral and similar height scale in both figures). The latter depicts well defined rectangular-shaped crystal facets with edges aligned to the $\langle 100 \rangle_{\mathrm{bct}}$ directions. The morphology of the phase separated sample appears somewhat more complex and heterogeneous. Nevertheless it is possible to identify areas that have a similar faceted appearance as the bct sample (enclosed by red-continuous lines) while other regions (enclosed by blue-dashed lines) reveal the presence of fine structures showing step-edges that seem oriented along the principal axes of the *Cmcm* crystal lattice (45° rotated). This observation of two distinctly different surface morphologies provides microscopic evidence in support of a laterally separated two-phase state in the thin film.

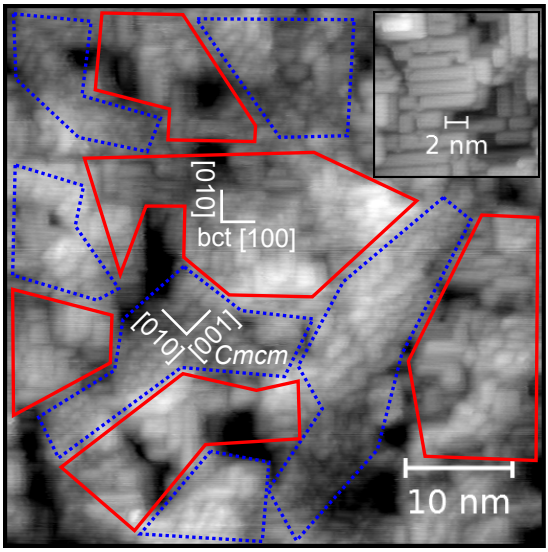

Figure 7.9.: *In situ* STM investigation of the surface of a freshly prepared phase separated sample with $z = 0.5$. The inset shows the (predominately) bct sample ($z = 0.75$) with well defined rectangular facets. The areas demarcated by continuous red lines highlight areas where the morphology has a similar bct-like rectangular appearance, while the blue-dotted lines enclose areas which show a more fine grained structure with step edges along the principal axes of the *Cmcm* unit cell. The images were measured in constant-current mode and the total height difference is about 9 Å.

In order to exclude any lateral variation of the lattice constant of the buffer layer as possible cause of the phase separation a HRTEM investigation of the buffer layer was performed. A high resolution micrograph is presented in Fig. 7.10(a), while (b) gives the result of a geometrical phase analysis [133], which allows a comparison of the local lattice parameter to a reference value. It represents thus a map of the strain state of the film. Here the in-plane strain ϵ_{xx} is presented, and the reference area (average zero strain value) is depicted by the rectangle in Fig. 7.10(a). The hot spots in the strain map might indicate the presence of misfit dislocations in the strained W-V layer. However, no lateral variation of the local lattice constant is observed on a scale larger than these single dislocations. Hence, any local structural inhomogeneity of the buffer layer on the length-scale of the FeRh nanostructures is safely ruled out as origin of the observed phase separation in support of a purely strain-induced mechanism.

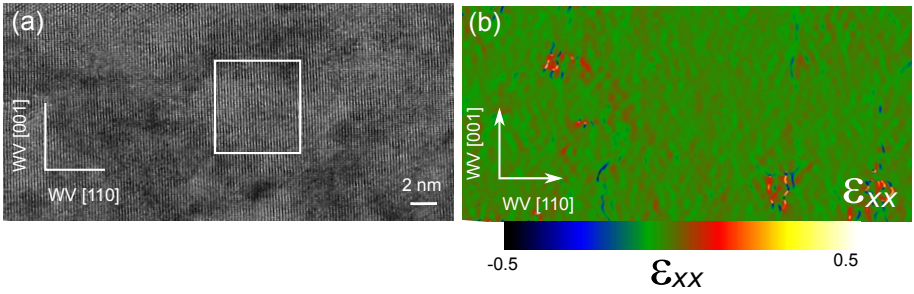

Figure 7.10.: (a) HRTEM micrograph of $W_{1-z}V_z$ buffer layer with $z = 0.57$. (b) Geometrical phase analysis (GPA) of the in-plane ϵ_{xx} strain, proving lateral homogeneity of the in-plane lattice constants.

In summary, the HRTEM and STM experiments thus microscopically confirm the presence of the two phases throughout the film thickness and their lateral distribution on the nano-scale, eventually completing the nano-structural picture of the strain adaption mechanism in the FeRh film.

7.2.5 Magnetic properties

In order to probe the macroscopic magnetic state and to identify a possible antiferromagnetic (AF) order and AF-FM transition (which would be expected for a perfectly ordered equiatomic B2-FeRh thin film [13]), we performed magnetic hysteresis $M(\mu_0 H)$ measurements at 30 K presented in Fig. 7.11(a), whereas the temperature (T) dependent Field Cooling (FC) $M(T)$ plots in a constant magnetic field of $\mu_0 H = 50$ mT, are shown in Fig. 7.11(b).

For the $z = 0$ sample we find no measurable magnetization M both for the 30 K hysteresis measurement and the temperature-sweep, in agreement with the properties of the RT grown samples (see Fig. 4.18 on page 60). The other two samples instead exhibit both FM behavior with average saturation magnetization values of 937 and 382 kA/m for $z = 0.75$ and 0.57, respectively. The $M(T)$ plots provide no evidence for an AF-FM transition, which would be marked by a steep increase in the value of M above room temperature. This is actually not very surprising as the fragile AF state is easily suppressed by a defective B2-ordering [59] and the rather moderate growth temperature of 300 °C is not sufficient to achieve full B2-ordering. Using the spectral fraction obtained from CEMS one can estimate the magnetization of the respective bct phases of the samples $z = 0.75$, 0.57 to about 1200 and 931 kA/m, respectively. The first value is close to what is expected

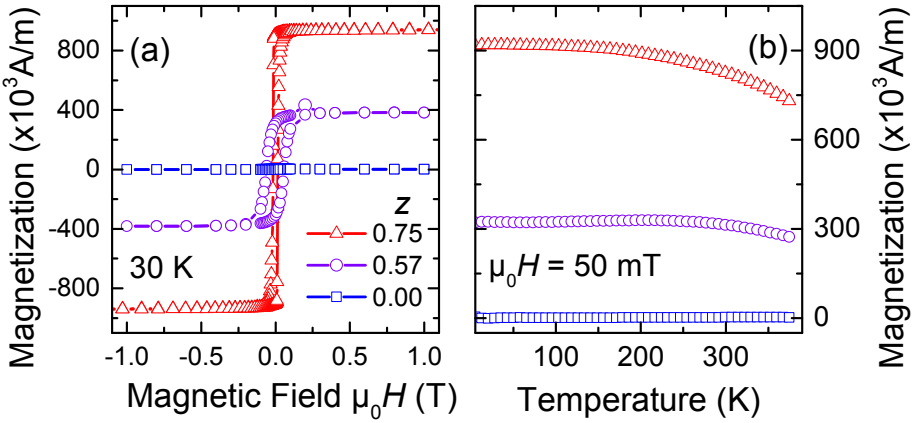

Figure 7.11.: (a) Hysteresis measurements $M(\mu_0 H)$ at 30 K. (b) Temperature dependent FC curves measured at constant magnetic field $\mu_0 H = 50\,\mathrm{mT}$ between 380 - 10 K.

for a FeRh alloy of that composition [57, 62]. The origin of the reduced value for the phase-separated sample can be related to reduced magnetic moments at the interfaces or grain boundaries, as well as to possible spin-canting or pinning due to the exchange coupling with the magnetic moments in the neighboring $Cmcm$ domains, which are at this temperature already in a spin glass (SG) state. The latter point might also be responsible for the increased coercivity in the phase-separated sample $z = 0.57$, which is about four times larger than that of the structurally more homogeneous sample $z = 0.75$.

The initial experiments which investigated the effect of the lattice constant of the buffer layers were conducted on a sample series with a reduced FeRh layer thickness of 3 nm. These samples provided already preliminary evidence for the phase separation and motivated the experiments with the thicker films unambiguously identifying the two phase state in the film. Details of this additional study are given in the Appendix A.3.2. However, the final result of this study is shown in Fig. 7.12. Here the average magnetization (in saturation) at 30 K is plotted as a function of the in-plane lattice parameter of the buffer layer a_{WV} for the 3 and 10 nm sample series. The clear correspondence between the two parameters in both samples series illustrates that the ratio of the FM B2 phase can be effectively tailored and strain-engineered by the choice of the appropriate buffer layer composition. Moreover, it proves once more that the adaption mechanism and also the actual

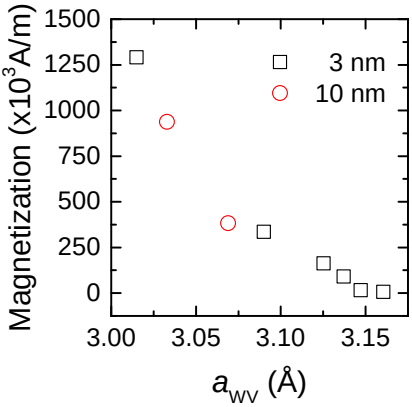

Figure 7.12.: Average magnetization at 30 K plotted as a function of the in-plane lattice constant of the buffer layer a_{WV} for the 3 and 10 nm sample series.

phase separation occurs directly at the $W_{1-z}V_z$/FeRh interface, solely driven by the epitaxial strain.

7.2.6 Discussion and conclusion

The experimental facts presented above suggest the following (magneto-)structural model and provide the basis for some hypothetical comments regarding the energy-landscape in the Fe-Rh system, as a function of strain, degree of chemical ordering and composition. In both boundary regions of epitaxial strain, the system is in a (meta)stable state. This is illustrated by Fig. 7.13, which depicts the strain or the in-plane lattice constant dependent calculated total energy of FM B2-FeRh (data adapted with permission from [134]) and a hypothetical trend for the $Cmcm$ phase. The latter scales the elastic energy U_{elast} with the strain ϵ, using a simplified quadratic relation, thus $U_{\text{elast}} \propto \epsilon^2$. Most probably, this curve overestimates the real trend, given that the material possesses yet another possibility to adapt its (effective) lattice constants to the buffer layer with the observed directional tilting of the lattice. Hence, it might be found at even lower total energies, considering also this additional kind of structural relaxation.

For small tensile in-plane strains, the film grows in a tetragonal distorted B2-structure, which is FM due to the defective B2-ordering. In a perfectly B2-ordered

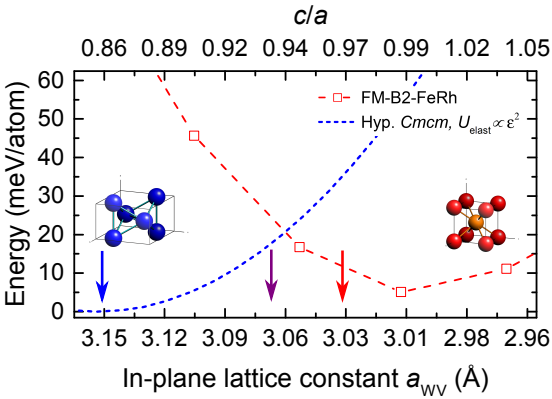

Figure 7.13.: Energy-landscape as a function of c/a at constant unit cell volume for FM-B2-FeRh, data adapted from [134] with permission, and a hypothetical curve proposed for *Cmcm*-FeRh, having its energy minimum at the W-in-plane lattice constant and scaling then with $\propto \epsilon^2$. The arrows indicate the lattice constant of the buffer layer of the three samples.

state, AF order would have been expected[1]. However, under maximum strain conditions, on an elemental W layer, the stable state is the orthorhombic structure with the already discussed consequences for the magnetic order. Interestingly, in this structure the chemical ordering is effectively suppressed, for the samples grown at ambient growth temperature, but also for the film deposited at a higher temperature, as it was the case in the present study. For intermediate strain values, phase separation takes place, resulting in the coexistence of both competing structures. The reduced thermodynamic stability of the B2 structure with increasing tetragonal distortion $c/a < 1$ (regardless of the kind of magnetic order) has been already calculated in a theoretical work [134]. By contrast, the $Cmcm$ structure is only forming due to an epitaxial strain-induced electron-lattice instability. For this reason it becomes less favorable with reduced in-plane strain, as suggested by the proposed shape of the energy curve shown in Fig. 7.13. This increase in metastability with reduced in-plane lattice spacing becomes obvious in the spontaneous decomposition in the two phases, seen also in one of the RT grown samples (see Fig. 7.5 on page 98).

[1] Evidence for at least partial AF ordering in other samples is presented at the end of the section.

The principal conclusion that can be drawn from the experiments is that in the intermediate strain regime the FeRh film does not follow traditional strain-relaxation schemes, such as the formation of misfit dislocations, which would have ultimately led to the bulk equilibrium structure. Instead, the film accommodates the strain via an adaptive nanostructuring mechanism, which, in addition to the results presented in Refs. [23, 95], contains now two distinctly different structural phases. Thus, the FeRh system distributes the epitaxial-strain by adjusting the relative ratios of the two phases, while each phase remains relatively close to its minimal-energy in-plane lattice constant, thus minimizing the total energy. This is reminiscent of the behavior in a two phase region of a compositional binary phase diagram and it thus offers the possibility to directly adjust and engineer the ratio of the two phase with the epitaxial strain.

Of crucial importance for the occurrence of such nanostructures is, as it has been pointed out by Kaufmann-Weiss *et al.* [23], the presence of relatively low interfacial or grain boundary energies (in their case twin boundary energies) between the different structural units, compared to the elastic energy terms. The structure and orientation of these boundaries in the samples, the interface between both structures, and the role of chemical order, will need further experimental and theoretical investigation, which is left open for future studies.

In summary, an original method for preparing epitaxial strain-induced, self-assembled, two-phase magnetic nanostructures with about 10 - 20 nm feature size has been presented. The findings might be applicable to the design of novel magnetic data storage media. Various experimental parameters, such as growth temperature, FeRh composition and the use of ternary element additions, can be explored in future, allowing for a further tailoring and optimizing the magnetic response of the nanostructures for their potential use in future technological applications. Moreover, the possibility of obtaining the bct-FeRh structural phase in the AF state in a well-tuned compositional range, will allow controlled down-scaling of the magnetic-bit size in the recently reported AF memory devices [7, 8] or in thermally assisted magnetic recording media based on the AF-FM transition [4–6].

The latter has been preliminary explored by applying an additional post-annealing step to the film, which is discussed as an outlook in the following section.

7.2.7 Outlook: Preliminary post-annealing study

Motivated by the above proposed potential application a preliminary post-annealing study was performed on a sample, which already in the as prepared state showed signs of the AF-FM transition. The partial presence of AF order, in contrast to the above presented FM samples, is possibly due to somewhat enhanced B2 ordering

and a Fe_xRh_{1-x} composition being well in the necessary window, where AF order can be stabilized.

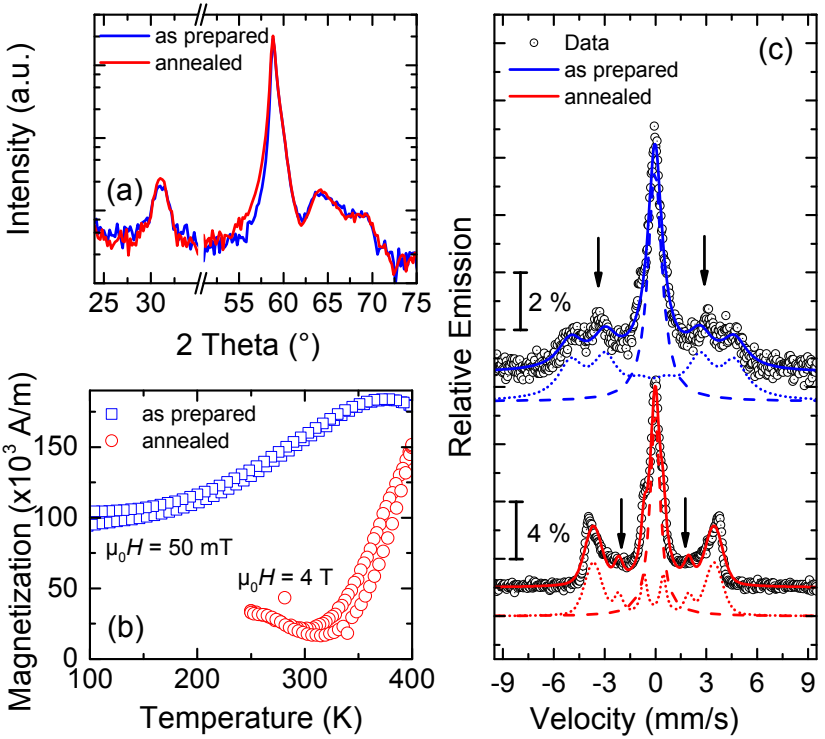

Figure 7.14.: Influence of post-annealing. (a) HRXRD patterns for a sample with $z = 0.5$, which in the as prepared and annealed state, after 90 min post-annealing at 500 °C. (b) Temperature dependent magnetization curves measured between 100 - 400 K for the as prepared and annealed state in a constant magnetic field $\mu_0 H = 50$ mT and 4 T, respectively. (c) RT-CEMS spectra of the two states, each fitted with a single line (dashed) and a magnetic sextet (dotted). The arrows indicate the position of the second and fifth absorption line. See text for details.

The bilayer sample with $z = 0.5$ was post-annealed under vacuum at 500 °C for 90 min. Fig. 7.14 shows the obtained results: (a) HRXRD patterns and (b) temperature dependent magnetization measurements of the as prepared and the post-annealed state. The structural investigation shows the familiar presence of the two phases, while the structure is not significantly changed by the post-annealing

procedure, besides a small increase in area of the super-structure reflection, due to enhanced B2 ordering. This indicates that the strain-induced nanostructure possesses a considerable thermal stability.

However, the more sensitive probe for the increase of B2-ordering is the observed magnetic behavior. The temperature dependent magnetization curves shows, already in the as prepared state, signs of the AF-FM transition, which is evidenced by the increase of magnetization with temperature. Yet, the transition appears smeared out and the sample shows some remaining magnetization at low temperature, which is due to the imperfect B2-ordering in the as prepared state effectively suppressing the subtle AF order in some areas of the sample. The post-annealing step removes this FM contribution nearly entirely, leading to the sharp increase of the magnetization above room temperature typical for the AF-FM transition [54].

A spectroscopic view with CEMS on the two states is presented in Fig. 7.14(c). The as prepared sample shows a similar spectrum as in the case of the FM intermediate sample displayed in the center of Fig. 7.7 on page 103, with at least two components, a paramagnetic singlet and a magnetic sextet. The latter is very broad indicating structural but possibly also magnetic disorder. The spectra are not unambiguously reproducible, a tentative fit is using a singlet and a magnetic sextet with Gaussian broadening, however the most important change upon post-annealing is visible with the bare eye.

The ratio between the absorption lines of the sextets is drastically changing from one state to the other, which indicates a variation of preferred orientation of the magnetic moments. For the as prepared state lines two and five are present (arrows). The ratio between second and third line can be obtained by fitting it with a Gaussian broadened sextet and the analysis yields a ratio of about 3.4. This indicates a spin arrangement between nearly random and in-plane [77]. However in the spectrum of the post-annealed sample the lines two and five are hardly observable (fitting with again a broadened sextet yields a ratio of 0.6), pointing at a spin reorientation towards an out-of-plane orientation, due to a strong magneto-crystalline anisotropy in the AF state. This is in agreement with literature, Bordel *et al.* showed that slightly tetragonal distorted grown FeRh films ($c/a = 0.985$) show this kind of preferred orientation of the spin arrangement in the AF phase [55]. As a tetragonal distortion with $c/a < 1$ is expected in the B2 phase also in the present sample, the observed spin reorientation represents also spectroscopic evidence for the occurrence of the AF state and effectiveness of the annealing procedure. The spectral area ratios of the magnetic and paramagnetic subspectra remain about constant (50%), supporting the claim based on HRXRD results, that the nanostructure is basically unharmed by the temperatures treatment.

The extraordinary thermal stability of the nanostructures allows further post-treatment of the films, with the aim of achieving a perfect B2 ordering and the AF-FM transition. This result provides solid and promising evidence for the above tentatively proposed potential applications of the magnetic nanostructures.

8 Conclusions and future work

8.1 Conclusions

The aim of the work presented in this thesis was to design novel nanostructured magnetic materials and to tailor their magnetic properties employing epitaxial strain. For that purpose the Fe-Rh system was selected as system of choice, and strained epitaxial $^{(57)}Fe_xRh_{1-x}$ films were deposited by Molecular Beam Epitaxy (MBE) onto W and $W_{1-z}V_z$ buffer layers grown by magnetron sputtering on MgO(001) single crystalline substrates. The bilayers were characterized by various advanced diffraction, electron and scanning probe microscopy, and spectroscopy techniques. The experimental studies were supported by Density Functional Theory (DFT)[1] first principle calculations. The newly found strain-adaption phenomena were systematically studied experimentally by varying the thickness and the composition of the Fe_xRh_{1-x} films on W buffer layers. The influence of the epitaxial boundary condition (epitaxial misfit (f)) was investigated in equiatomic FeRh films deposited on $W_{1-z}V_z$ alloy buffer layers by varying the V content z. In this case a distinct growth temperature dependence of the final (nano-)structure was observed. Fig. 8.1 summarizes the performed experiments and schematically illustrates the obtained conclusions, which are discussed in detail in the following paragraphs.

In equiatomic, but chemically disordered, FeRh films on W a yet unknown lattice instability was discovered, resulting in the formation of a novel strain-induced orthorhombic martensite structure (space group No.63, *Cmcm*, see Fig. 8.1(a)). The films form a 90° rotated domain pattern on the nano-scale, allowing for, on average, coherent strain-adaption of the FeRh film to the W buffer layer. The crystallographic structure, derived from a combination of DFT calculations and X-ray diffraction, reveals similarities to the local atomic arrangements of a hexagonal close packed (hcp) structure. This itself is an unexpected finding, since a hcp phase has not been reported in the Fe-Rh system so far, although hcp phases exist in related transition metal binary alloys, such as Fe-Ir, Fe-Ru [135, 136] or Co-Rh, Cr-Rh [137, 138]. Results of electronic structure calculations by DFT suggest that this adaptive transformation is triggered by a band-Jahn-Teller-type mechanism

[1] The collaboration with M. E. Gruner (Theoretical Physics department, University Duisburg-Essen) has been established during this project.

entangled with Fermi surface nesting. These findings establish the disordered and strained FeRh alloys as a member of a larger material class with such prominent examples as the magnetic-shape-memory alloys FePd [97, 98] and Ni_2MnGa [117–121]. The magnetic properties of the novel phase are characterized by a high degree of magnetic frustration, leading to the suppression of ferromagnetic (FM) order and the formation of a spin glass (SG) state at low temperatures, similar to the magnetic behavior of metastable face centered cubic (fcc) FeRh (A1-phase) [14–17]. Hence one may conclude that the (pseudo-)close-packed atomic arrangement defines the magnetic properties in both phases.

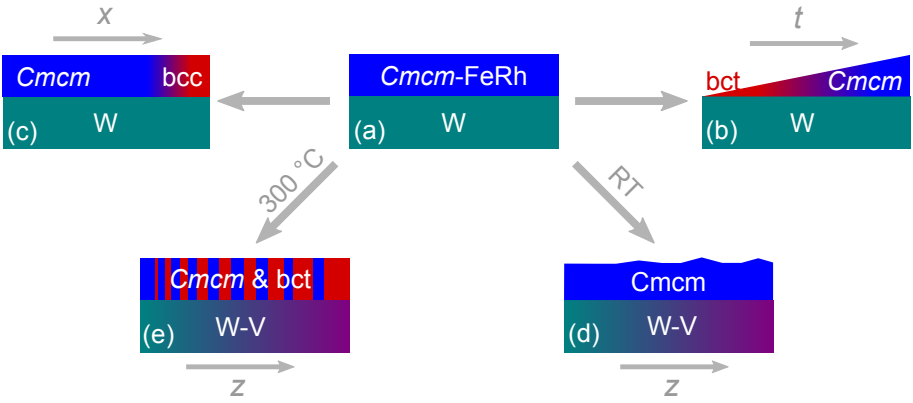

Figure 8.1.: Graphical summary of the presented research. The discovery of the strain-induced *Cmcm* martensite phase in FeRh/W bilayers is represented in the center of the figure (a). Then the (b) thickness t and (c) Fe_xRh_{1-x} composition dependence of the strain-induced transformation is illustrated. The influence of the epitaxial misfit (f) was explored by using $W_{1-z}V_z$ alloy buffer layers. Here a distinct effect of the growth temperatures on the final structures was identified, which is illustrated in (d) for the RT growth, and in (e) for the growth at 300°C.

More generally, the observed structural transition can be interpreted as an internal amplification of an external symmetry breaking, namely the epitaxial boundary condition, which at first forces a cubic-to-tetragonal transformation, eventually resulting in an even lower symmetry orthorhombic structure due to an induced lattice instability. An analogous case was identified in thin films of multiferroic $BiFeO_3$, where the applied epitaxial strain results in the formation of reduced symmetry structures [139, 140], which might be linked to a phonon softening [141].

The study of the thickness dependence of the transformation gave evidence for a continuous, coherent evolution from a body centered tetragonal (bct) structure

in the thinnest films, towards the *Cmcm* phase observed in the thickest films, underpinning the cooperative and martensitic nature of the transformation (see Fig. 8.1(b)). The theoretical results suggested a strong influence of the Fe_xRh_{1-x} composition. Indeed it was found experimentally that the *Cmcm* phase cannot be stabilized beyond a Fe content of 72 at.-% and a fully relaxed, FM body centered cubic (bcc) phase is identified instead (Fig. 8.1(c)).

The growth of equiatomic FeRh on $W_{1-z}V_z$ alloy buffer layers (decreased epitaxial misfit with respect to pure W) revealed a highly metastable state of the grown structures. This leads to different results in terms of structural, nano-structural and magnetic properties, which strongly depend on the growth temperature.

The deposition of epitaxial FeRh layers on $W_{1-z}V_z$ buffer layers at ambient temperature (see Fig. 8.1(d)) shows that the *Cmcm* phase, which was found on pure W, can be stabilized on buffer layers with a smaller lattice constant as well. However, with decreasing buffer layer lattice constant, the *Cmcm* structure is no longer able to adapt to the epitaxial boundary conditions by straining alone. Hence a second adaption mechanism is observed: Directional tilting or buckling of the lattice planes in one specific crystallographic direction. This may be understood considering the thermodynamic relations of the disordered phases, which favor the close-packed A1 over the bcc A2 phase [62]. However, the A2 phase geometrically matches better to the lattice constant of the V-rich buffer layers. Thus the buckling of the *Cmcm* structure displays a possibility for the system to remain close to the favorable close-packed configuration, avoiding the A2 phase, while still conforming to the epitaxial boundary condition.

Finally, FeRh layers grown at elevated temperatures of 300 °C (see Fig. 8.1(e)) show a phase separation into two structurally and magnetically different phases: On the one hand the (room temperature) paramagnetic (PM) *Cmcm* phase and on the other hand the partially B2-ordered FM bct phase. Since this phase separation happens spontaneously and laterally on the nanometer-scale one may refer to the resulting structure as a self-assembled magnetic nanostructure. Furthermore, the two phases are proposed to share the misfit to the underlying buffer layer by adjusting their ratio, each staying as close as possible to their equilibrium structure, which eventually minimizes the elastic energy (U_{el}). This direct relation promotes straightforward tailoring of the nanostructure, by using the epitaxial misfit. Although this strain-adaption mechanism shares some characteristics with the adaptive nano-twin modulations observed in strained FePd thin films [23], it reaches even further by involving an additional second phase for the adaption mechanism.

The fabrication of the self-assembled magnetic nanostructure illustrates how the discovered lattice instability in FeRh alloys, which was primarily of fundamental

scientific interest, was placed into an application related context employing the versatile tools of epitaxial strain-engineering, as it was stated in the objectives.

8.2 Outlook and future work

The implication of the work presented in this thesis may reach well beyond the Fe-Rh system, given that also other transition metal binary (or ternary) alloys possess lattice instabilities and interesting functional properties. However, based on the here presented findings several future experiments on the Fe-Rh material system can be proposed; the examples are briefly discussed below.

One straightforward experiment concerning the FeRh films on W is the growth of even thicker films[2] $> 100\,\mathrm{nm}$, which would explore the possibility of further structural relaxation towards a hcp phase or another structure. Investigations by plane-view High-Resolution Transmission Electron Microscopy (HRTEM), might provide a definite answer to the open question of the nature of the grain boundaries between the two 90° rotated domains.

Another interesting point which remained notional in the present work, is whether Fermi surface nesting together with a phonon softening is the causative reason for the transformation. Here, the planned Fe-partial phonon-Density of States (DOS) measurements by nuclear inelastic scattering will provide further insights by comparing the phonon-DOS of a sample with bcc structure to one with $Cmcm$ structure, while support from theory will facilitate data interpretation.

Further first principle calculations of the relaxed structures and their energies in a broad lattice constant range, bridging the entire Bain path, and possibly also for different Fe_xRh_{1-x} concentration, will shed light on the relation between the competing disordered phases and would possibly identify flat areas of the energy landscape of the system as function of strain and composition.

The experimental counterpart to this calculations is the growth of Fe-rich alloys, close to the limit of the $Cmcm$ compositional limit, on W-V alloys. In such way it may be possible to map the entire martensitic transformation path from $Cmcm$ to bcc. However, in an extension to that, it is also interesting to close the gap between the bcc and fcc phase, hence study the growth of structures with $c/a > 1$ using e.g. Cr-V [85] and Au-Cu [87] buffer layers.

With respect to the self-assembled nanostructures, it makes sense to optimize the films further to obtain a perfectly B2-ordered second phase in the antiferromagnetic (AF) state. The preliminary results presented in Chap. 7.2.7 prove that the nanostructures withstand post-annealing procedures as high as 500 °C and that the

[2] Due to the small amount of source material and the vanishing low growth rates, the growth of films in that thickness range is not possible with the Mini-MBE employed in this thesis.

AF-FM transition can in principle be achieved. The resulting magnetic nanostructure, consisting of AF nano-sized areas in a PM matrix, may be used for down-scaling the bit size of the recently proposed AF memristor [7, 8].

This achievement may also allow to grow vertically exchange coupled multilayer-nanostructures, deployable in thermal assisted magnetic recording devices [4–6]. Such multilayers can be prepared by adjusting the Fe_xRh_{1-x} composition through the deposited thickness combined with a well-chosen post-annealing strategy. The first layer is grown with a near-equiatomic composition, necessary to stabilize an AF state in the B2-phase. The second layer is deposited with a higher Fe content, resulting in a FM state, while everything is laterally embedded in the *Cmcm* matrix, which is PM in both Fe_xRh_{1-x} compositions. Moreover, the concept of thermally assisted magnetic recording can be further extended, by exploiting the magneto-crystalline anisotropy induced in the AF state by the tetragonal distortion of the B2 phase. The latter may additionally result in a perpendicular magnetization of the entire exchange coupled multilayers, without involving another material with high intrinsic magnetic anisotropy e.g. $L1_0$-FePt, as initially suggested by Thiele *et al.* [4]. This again illustrates the various beneficial possibilities of epitaxial strain-engineering.

Bibliography

[1] M. Fallot, Ann. Phys. **10**, 291 (1938) (cit. on pp. 1, 13, 86).

[2] M. Fallot, and R. Horcart, Rev. Sci. **77**, 498 (1939) (cit. on pp. 1, 13).

[3] R. O. Cherifi, V. Ivanovskaya, L. C. Phillips, A. Zobelli, I. C. Infante, E. Jacquet, V. Garcia, S. Fusil, P. R. Briddon, N. Guiblin, A. Mougin, A. A. Ünal, F. Kronast, S. Valencia, B. Dkhil, A. Barthélémy, and M. Bibes, Nat. Mater. **13**, 345 (2014) 10.1038/nmat3870 (cit. on pp. 1, 15).

[4] J.-U. Thiele, S. Maat, and E. E. Fullerton, Appl. Phys. Lett. **82**, 2859 (2003) 10.1063/1.1571232 (cit. on pp. 1, 111, 119).

[5] Z. Jia, and R. D. K. Misra, Mater. Technol. **26**, 200 (2011) 10.1179/175355511X13109965351112 (cit. on pp. 1, 111, 119).

[6] L. Lounis, C. Spezzani, R. Delaunay, F. Fortuna, M. Obstbaum, S. Günther, C. H. Back, H. Popescu, F. Vidal, and M. Sacchi, J. Phys. D. Appl. Phys. **49**, 205003 (2016) 10.1088/0022-3727/49/20/205003 (cit. on pp. 1, 111, 119).

[7] X. Marti, I. Fina, C. Frontera, J. Liu, P. Wadley, Q. He, R. J. Paull, J. D. Clarkson, J. Kudrnovský, I. Turek, J. Kuneš, D. Yi, J.-H. Chu, C. T. Nelson, L. You, E. Arenholz, S. Salahuddin, J. Fontcuberta, T. Jungwirth, and R. Ramesh, Nat. Mater. **13**, 367 (2014) 10.1038/nmat3861 (cit. on pp. 1, 111, 119).

[8] T. Moriyama, N. Matsuzaki, K.-J. Kim, I. Suzuki, T. Taniyama, and T. Ono, Appl. Phys. Lett. **107**, 122403 (2015) 10.1063/1.4931567 (cit. on pp. 1, 111, 119).

[9] D. W. Cooke, F. Hellman, C. Baldasseroni, C. Bordel, S. Moyerman, and E. E. Fullerton, Phys. Rev. Lett. **109**, 255901 (2012) 10.1103/PhysRevLett.109.255901 (cit. on p. 1).

[10] J. Liu, T. Gottschall, K. P. Skokov, J. D. Moore, and O. Gutfleisch, Nat. Mater. **11**, 620 (2012) 10.1038/nmat3334 (cit. on p. 1).

[11] E. Stern-Taulats, A. Gràcia-Condal, A. Planes, P. Lloveras, M. Barrio, J.-L. Tamarit, S. Pramanick, S. Majumdar, and L. Mañosa, Appl. Phys. Lett. **107**, 152409 (2015) 10.1063/1.4933409 (cit. on p. 1).

[12] C. C. Chao, P. Duwez, and C. C. Tsuei, J. Appl. Phys. **42**, 4282 (1971) 10.1063/1.1659766 (cit. on pp. 1, 17, 60, 82).

[13] G. Shirane, C. W. Chen, P. A. Flinn, and R. Nathans, Phys. Rev. **131**, 183 (1963) 10.1103/PhysRev.131.183 (cit. on pp. 1, 2, 13, 17, 18, 41, 79, 82, 83, 86, 87, 102, 103, 107, 143).

[14] K. Sumiyama, M. Shiga, and Y. Nakamura, Phys. Status Solidi **13**, K75 (1972) 10.1002/pssa.2210130154 (cit. on pp. 1, 2, 17, 60, 116).

[15] G. Filoti, V. Kuncsea, E. Navarro, A. Hernando, and M. Rosenberg, J. Alloys Compd. **278**, 60 (1998) 10.1016/S0925-8388(98)00591-X (cit. on pp. 1, 2, 17, 60, 85, 116).

[16] A. Hernando, E. Navarro, M. Multigner, A. R. Yavari, D. Fiorani, M. Rosenberg, G. Filoti, and R. Caciuffo, Phys. Rev. B **58**, 5181 (1998) 10.1103/PhysRevB.58.5181 (cit. on pp. 1, 2, 17, 60, 86, 116).

[17] V. Kuncser, M. Rosenberg, G. Principi, U. Russo, A. Hernando, E. Navarro, and G. Filoti, J. Alloys Compd. **308**, 21 (2000) 10.1016/S0925-8388(00)00821-5 (cit. on pp. 1, 2, 17, 60, 116).

[18] Y. Ohtani, and I. Hatakeyama, J. Appl. Phys. **74**, 3328 (1993) 10.1063/1.354557 (cit. on p. 1).

[19] J. Ayoub, C. Gatel, C. Roucau, and M. Casanove, J. Cryst. Growth **314**, 336 (2011) 10.1016/j.jcrysgro.2010.11.127 (cit. on pp. 1, 17, 95, 97).

[20] M. Castiella, C. Gatel, J. F. Bobo, N. Ratel-Ramond, R. Tan, M. Respaud, and M. J. Casanove, Mater. Res. Express **2**, 086401 (2015) 10.1088/2053-1591/2/8/086401 (cit. on pp. 1, 17, 95, 97).

[21] E. C. Bain, Trans. Am. Insitute Min. Metall. Eng. **70**, 25 (1924) (cit. on pp. 2, 9).

[22] J. Buschbeck, I. Opahle, M. Richter, U. K. Rößler, P. Klaer, M. Kallmayer, H. J. Elmers, G. Jakob, L. Schultz, and S. Fähler, Phys. Rev. Lett. **103**, 216101 (2009) 10.1103/PhysRevLett.103.216101 (cit. on pp. 2, 6, 8–10, 30).

[23] S. Kauffmann-Weiss, M. E. Gruner, A. Backen, L. Schultz, P. Entel, and S. Fähler, Phys. Rev. Lett. **107**, 206105 (2011) 10.1103/PhysRevLett.107.206105 (cit. on pp. 2, 9, 11, 46, 50, 54, 64, 102, 111, 117).

[24] M. Takahashi, and R. Oshima, J. Phys. IV **05**, C8–491–C8 (1995) 10.1051/jp4:1995875 (cit. on pp. 2, 18).

[25] A. Hashimoto, Y. Kaneno, T. Matsui, Y. Saitoh, and A. Iwase, Trans. Mater. Res. Soc. Japan **38**, 329 (2013) 10.14723/tmrsj.38.329 (cit. on pp. 2, 17, 18).

[26] T. Fukuda, and T. Kakeshita, J. Alloys Compd. **563**, 192 (2013) 10.1016/j.jallcom.2013.02.029 (cit. on pp. 2, 18).

[27] S. Yuasa, H. Miyajima, Y. Otani, G. Masada, N. Wakabayashi, and K. Tajima, J. Phys. Soc. Japan **64**, 3153 (1995) 10.1143/JPSJ.64.3153 (cit. on pp. 2, 18).

[28] N. Takahara, M. Takahashi, and R. Oshima, J. Japan Inst. Met. **59**, 599 (1995), https://www.jstage.jst.go.jp/article/jinstmet1952/59/6/59%7B%5C_%7D6%7B%5C_%7D599/%7B%5C_%7Darticle (cit. on pp. 2, 18).

[29] J. Kudrnovský, V. Drchal, and I. Turek, Phys. Rev. B **91**, 014435 (2015) 10.1103/PhysRevB.91.014435 (cit. on pp. 2, 14–16, 42, 56, 57).

[30] L. M. Sandratskii, and P. Mavropoulos, Phys. Rev. B **83**, 174408 (2011) 10.1103/PhysRevB.83.174408 (cit. on pp. 2, 14, 56).

[31] J. C. Slater, Phys. Rev. **36**, 57 (1930) 10.1103/PhysRev.36.57 (cit. on p. 5).

[32] D. Fuchs, E. Arac, C. Pinta, S. Schuppler, R. Schneider, and H. V. Löhneysen, Phys. Rev. B - Condens. Matter Mater. Phys. **77**, 1 (2008) 10.1103/PhysRevB.77.014434 (cit. on pp. 6, 7).

[33] J. H. Lee, L. Fang, E. Vlahos, X. Ke, Y. W. Jung, L. F. Kourkoutis, J.-W. Kim, P. J. Ryan, T. Heeg, M. Roeckerath, V. Goian, M. Bernhagen, R. Uecker, P. C. Hammel, K. M. Rabe, S. Kamba, J. Schubert, J. W. Freeland, D. a. Muller, C. J. Fennie, P. Schiffer, V. Gopalan, E. Johnston-Halperin, and D. G. Schlom, Nature **466**, 954 (2010) 10.1038/nature09331 (cit. on p. 6).

[34] C. H. Lee, H. He, F. J. Lamelas, W. Vavra, C. Uher, and R. Clarke, Phys. Rev. B **42**, 1066 (1990) 10.1103/PhysRevB.42.1066 (cit. on p. 6).

[35] G. Andersson, T. Burkert, P. Warnicke, M. Björck, B. Sanyal, C. Chacon, C. Zlotea, L. Nordström, P. Nordblad, and O. Eriksson, Phys. Rev. Lett. **96**, 037205 (2006) 10.1103/PhysRevLett.96.037205 (cit. on p. 6).

[36] H. Wang, C. Du, P. C. Hammel, and F. Yang, Phys. Rev. B **89**, 134404 (2014) 10.1103/PhysRevB.89.134404 (cit. on p. 6).

[37] M. A. Herman, W. Richter, and H. Sitter, *Epitaxy*, Vol. 62, Springer Series in MATERIALS SCIENCE (Springer Berlin Heidelberg, Berlin, Heidelberg, 2004), 10.1007/978-3-662-07064-2 (cit. on p. 6).

[38] J. W. Matthews, J. Vac. Sci. Technol. **12**, 126 (1975) 10.1116/1.568741 (cit. on pp. 6, 7).

[39] J. H. Van Der Merwe, J. Appl. Phys. **34**, 123 (1963) 10.1063/1.1729051 (cit. on pp. 6, 7, 9).

[40] D. Sander, Reports Prog. Phys. **62**, 809 (1999) 10.1088/0034-4885/62/5/204 (cit. on p. 7).

[41] W. Wulfhekel, F. Zavaliche, R. Hertel, S. Bodea, G. Steierl, G. Liu, J. Kirschner, and H. Oepen, Phys. Rev. B **68**, 144416 (2003) 10.1103/PhysRevB.68.144416 (cit. on p. 7).

[42] J. A. del Alamo, Nature **479**, 317 (2011) 10.1038/nature10677 (cit. on p. 7).

[43] P. M. Leufke, A. K. Mishra, A. Beck, D. Wang, C. Kübel, R. Kruk, and H. Hahn, Thin Solid Films **520**, 5521 (2012) 10.1016/j.tsf.2012.04.064 (cit. on pp. 7, 30).

[44] W. Si, and X. X. Xi, Appl. Phys. Lett. **78**, 240 (2001) 10.1063/1.1338966 (cit. on p. 7).

[45] A. G. Khachaturyan, S. M. Shapiro, and S. Semenovskaya, Phys. Rev. B **43**, 10832 (1991) 10.1103/PhysRevB.43.10832 (cit. on pp. 11, 50).

[46] S. Kaufmann, U. K. Rößler, O. Heczko, M. Wuttig, J. Buschbeck, L. Schultz, and S. Fähler, Phys. Rev. Lett. **104**, 1 (2010) 10.1103/PhysRevLett.104.145702 (cit. on pp. 11, 46, 50, 64).

[47] A. Arabi-Hashemi, and S. G. Mayr, Phys. Rev. Lett. **109**, 195704 (2012) 10.1103/PhysRevLett.109.195704 (cit. on pp. 12, 18).

[48] A. Arabi-Hashemi, R. Witte, A. Lotnyk, R. A. Brand, A. Setzer, P. Esquinazi, H. Hahn, R. S. Averback, and S. G. Mayr, New J. Phys. **17**, 053029 (2015) 10.1088/1367-2630/17/5/053029 (cit. on pp. 12, 18).

[49] H. Okamoto, J. Phase Equilibria Diffus. **32**, 472 (2011) 10.1007/s11669-011-9934-6 (cit. on p. 13).

[50] A. Liechtenstein, M. Katsnelson, V. Antropov, and V. Gubanov, J. Magn. Magn. Mater. **67**, 65 (1987) 10.1016/0304-8853(87)90721-9 (cit. on pp. 14, 36, 56).

[51] R. Wayne, Phys. Rev. **170**, 523 (1968) 10.1103/PhysRev.170.523 (cit. on pp. 15, 41).

[52] K. Kamenev, Z. Arnold, J. Kamarád, and N. Baranov, J. Alloys Compd. **252**, 1 (1997) 10.1016/S0925-8388(96)02710-7 (cit. on p. 15).

[53] E. Stern-Taulats, A. Planes, P. Lloveras, M. Barrio, J.-L. Tamarit, S. Pramanick, S. Majumdar, C. Frontera, and L. Mañosa, Phys. Rev. B **89**, 214105 (2014) 10.1103/PhysRevB.89.214105 (cit. on p. 15).

[54] S. Maat, J.-U. Thiele, and E. E. Fullerton, Phys. Rev. B **72**, 214432 (2005) 10.1103/PhysRevB.72.214432 (cit. on pp. 15, 113).

[55] C. Bordel, J. Juraszek, D. W. Cooke, C. Baldasseroni, S. Mankovsky, J. Minár, H. Ebert, S. Moyerman, E. E. Fullerton, and F. Hellman, Phys. Rev. Lett. **109**, 117201 (2012) 10.1103/PhysRevLett.109.117201 (cit. on pp. 15, 113).

[56] J.-S. Lee, E. Vescovo, L. Plucinski, C. M. Schneider, and C.-C. Kao, Phys. Rev. B **82**, 224410 (2010) 10.1103/PhysRevB.82.224410 (cit. on p. 15).

[57] L. J. Swartzendruber, Bull. Alloy Phase Diagrams **5**, 456 (1984) 10.1007/BF02872896 (cit. on pp. 15, 16, 40, 41, 79, 82, 108).

[58] B. Predel, *V-W (Vanadium-Tungsten)*, edited by O. Madelung, Landolt-Börnstein - Group IV Physical Chemistry (Springer-Verlag, Berlin/Heidelberg, 1998), pp. 1–3, 10.1007/10551312_2869 (cit. on pp. 15, 30, 32).

[59] J. B. Staunton, R. Banerjee, M. dos Santos Dias, A. Deak, and L. Szunyogh, Phys. Rev. B **89**, 054427 (2014) 10.1103/PhysRevB.89.054427 (cit. on pp. 16, 107).

[60] Y. Kaneta, S. Ishino, Y. Chen, S. Iwata, and A. Iwase, Jpn. J. Appl. Phys. **50**, 105803 (2011) 10.1143/JJAP.50.105803 (cit. on p. 16).

[61] G. Shirane, D. E. Cox, and S. L. Ruby, Phys. Rev. **125**, 1158 (1962) 10.1103/PhysRev.125.1158 (cit. on p. 16).

[62] I. Ohnuma, T. Gendo, R. Kainuma, G. Inden, and K. Ishida, ISIJ Int. **49**, 1212 (2009) 10.2355/isijinternational.49.1212 (cit. on pp. 16, 17, 41, 42, 59, 60, 95, 108, 117).

[63] A. Heidarian, R. Bali, J. Grenzer, R. Wilhelm, R. Heller, O. Yildirim, J. Lindner, and K. Potzger, Nucl. Instruments Methods Phys. Res. Sect. B Beam Interact. with Mater. Atoms **358**, 251 (2015) 10.1016/j.nimb.2015.06.027 (cit. on p. 17).

[64] K. Aikoh, S. Kosugi, T. Matsui, and A. Iwase, J. Appl. Phys. **109**, 07E311 (2011) 10.1063/1.3549440 (cit. on pp. 17, 105).

[65] W. Lu, P. Huang, K. Li, and B. Yan, J. Mater. Res. **28**, 1042 (2013) 10.1557/jmr.2013.61 (cit. on pp. 17, 59, 60).

[66] J. M. Lommel, J. Appl. Phys. **38**, 1263 (1967) 10.1063/1.1709570 (cit. on p. 17).

[67] N. Fujita, S. Kosugi, Y. Saitoh, Y. Kaneta, K. Kume, T. Batchuluun, N. Ishikawa, T. Matsui, and A. Iwase, J. Appl. Phys. **107**, 09E302 (2010) 10.1063/1.3359440 (cit. on p. 17).

[68] J. A. Mydosh, Reports Prog. Phys. **78**, 052501 (2015) 10.1088/0034-4885/78/5/052501 (cit. on p. 17).

[69] R. Oshima, F. Hori, Y. Kibata, M. Komatsu, and M. Kiritani, Mater. Sci. Eng. A **350**, 139 (2003) 10.1016/S0921-5093(02)00715-3 (cit. on p. 18).

[70] C. D. N. Chan, *X-ray diffractometer: Eulerian cradle, or four circle diffractometer*, 2005, https://upload.wikimedia.org/wikipedia/commons/2/20/Diffractometre%7B%5C_%7Dberceau%7B%5C_%7DEuler.png (cit. on p. 20).

[71] M. Birkholz, *Thin Film Analysis by X-Ray Scattering* (Wiley-VCH Verlag GmbH & Co. KGaA, Weinheim, FRG, Oct. 2005), pp. 165–175, 10.1002/3527607595 (cit. on p. 20).

[72] A. Boulle, F. Conchon, and R. Guinebretière, J. Appl. Crystallogr. **42**, 85 (2009) 10.1107/S0021889808036406 (cit. on p. 21).

[73] Y. Igarashi, J. Appl. Phys. **52**, 7208 (1981) 10.1063/1.328745 (cit. on pp. 22, 30).

[74] H. Kimura, I. Petrov, F. Adibi, and J. Greene, J. Cryst. Growth **123**, 344 (1992) 10.1016/0022-0248(92)90594-9 (cit. on pp. 22, 30, 40).

[75] J. Clarke, and A. I. Braginski, eds., *The SQUID Handbook. Vol. I Fundamentals and Technology of SQUIDs and SQUID Systems*, Vol. 21, 5 (Wiley-VCH, Weinheim, Aug. 2004), pp. 583–583, ISBN: 3-527-40229-2 (cit. on p. 23).

[76] J. Orna, L. Morellón, P. A. Algarabel, J. M. De Teresa, A. Fernández-Pacheco, G. Simón, C. Magen, J. A. Pardo, and M. R. Ibarra, Adv. Sci. Technol. **67**, 82 (2010) 10.4028/www.scientific.net/AST.67.82 (cit. on p. 24).

[77] P. Gütlich, E. Bill, and A. X. Trautwein, *Mössbauer Spectroscopy and Transition Metal Chemistry* (Springer Berlin Heidelberg, Berlin, Heidelberg, Nov. 2011), 10.1007/978-3-540-88428-6 (cit. on pp. 24, 26, 72, 113).

[78] R. L. Mössbauer, Zeitschrift für Phys. **151**, 124 (1958) 10.1007/BF01344210 (cit. on p. 24).

[79] R. L. Mössbauer, Naturwissenschaften **45**, 538 (1958) (cit. on p. 24).

[80] O. C. Kistner, and A. W. Sunyar, Phys. Rev. Lett. **4**, 412 (1960) 10.1103/PhysRevLett.4.412 (cit. on p. 25).

[81] S. S. Hanna, J. Heberle, C. Littlejohn, G. J. Perlow, R. S. Preston, and D. H. Vincent, Phys. Rev. Lett. **4**, 177 (1960) 10.1103/PhysRevLett.4.177 (cit. on p. 25).

[82] M. Ohring, *The materials science of thin films* (Academic Press, Boston, 1992), p. 275, ISBN: 0-12-524990-X (cit. on p. 27).

[83] M. Mayer, AIP Conf. Proc. **475**, 541 (1999) 10.1063/1.59188 (cit. on p. 27).

[84] L. Vitos, A. Ruban, H. Skriver, and J. Kollár, Surf. Sci. **411**, 186 (1998) 10.1016/S0039-6028(98)00363-X (cit. on p. 29).

[85] T. C. Kaspar, M. E. Bowden, C. Wang, V. Shutthanandan, S. Manandhar, R. M. van Ginhoven, B. D. Wirth, and R. J. Kurtz, Thin Solid Films **550**, 1 (2014) 10.1016/j.tsf.2013.09.067 (cit. on pp. 30, 39, 118).

[86] O. Fruchart, A. Rousseau, D. Schmaus, A. L'Hoir, R. Haettel, and L. Ortega, Appl. Phys. Lett. **98**, 131906 (2011) 10.1063/1.3567793 (cit. on p. 30).

[87] S. Kauffmann-Weiss, S. Hamann, L. Reichel, A. Siegel, V. Alexandrakis, R. Heller, L. Schultz, A. Ludwig, and S. Fähler, Apl Mater. **2**, 046107 (2014) 10.1063/1.4870759 (cit. on pp. 30, 118).

[88] P. M. Leufke, R. Kruk, D. Wang, C. Kübel, and H. Hahn, AIP Adv. **2**, 032184 (2012) 10.1063/1.4756997 (cit. on p. 30).

[89] F. H. Featherston, and J. R. Neighbours, Phys. Rev. **130**, 1324 (1963) 10.1103/PhysRev.130.1324 (cit. on p. 32).

[90] G. A. Alers, Phys. Rev. **119**, 1532 (1960) 10.1103/PhysRev.119.1532 (cit. on p. 32).

[91] M. A. Tomaz, G. Harp, E. Mayo, D. Lederman, R. Wu, and W. L. O'Brien, J. Vac. Sci. Technol. A Vacuum, Surfaces, Film. **16**, 1336 (1998) 10.1116/1.581147 (cit. on pp. 35, 67).

[92] K. Hanisch, W. Keune, R. A. Brand, C. Binek, and W. Kleemann, J. Appl. Phys. **76**, 6528 (1994) 10.1063/1.358213 (cit. on pp. 35, 67).

[93] A. M. Begley, S. K. Kim, F. Jona, and P. M. Marcus, Phys. Rev. B **48**, 1786 (1993) 10.1103/PhysRevB.48.1786 (cit. on p. 35).

[94] J. A. Floro, and E. Chason, in *Situ real-time charact. thin film.* Edited by O. Auciello, and A. R. Krauss, (John Wiley & Sons, 2001) Chap. 7, p. 280, ISBN: 978-0-471-24141-6 (cit. on p. 35).

[95] R. Witte, R. Kruk, M. E. Gruner, R. A. Brand, D. Wang, S. Schlabach, A. Beck, V. Provenzano, R. Pentcheva, H. Wende, and H. Hahn, Phys. Rev. B **93**, 104416 (2016) 10.1103/PhysRevB.93.104416 (cit. on pp. 36–38, 41, 79, 99, 100, 102, 103, 111).

[96] A. Zunger, S.-H. Wei, L. G. Ferreira, and J. E. Bernard, Phys. Rev. Lett. **65**, 353 (1990) 10.1103/PhysRevLett.65.353 (cit. on p. 36).

[97] I. Opahle, K. Koepernik, U. Nitzsche, and M. Richter, Appl. Phys. Lett. **94**, 072508 (2009) 10.1063/1.3086878 (cit. on pp. 36, 62, 116, 135, 136).

[98] M. E. Gruner, and P. Entel, Phys. Rev. B **83**, 214415 (2011) 10.1103/PhysRevB.83.214415 (cit. on pp. 36, 62, 116).

[99] Z. W. Lu, S.-H. Wei, and A. Zunger, Phys. Rev. B **45**, 10314 (1992) 10.1103/PhysRevB.45.10314 (cit. on p. 36).

[100] M. Gutsche, H. Kraus, J. Jochum, B. Kemmather, and G. Gutekunst, Thin Solid Films **248**, 18 (1994) 10.1016/0040-6090(94)90204-6 (cit. on p. 39).

[101] G. Chiarotti, *Interaction of Radiation with Surfaces and Electron Tunneling*, edited by G. Chiarotti, Vol. 24D, Landolt-Börnstein - Group III Condensed Matter (Springer-Verlag, Berlin/Heidelberg, 1996), pp. 21–26, 10.1007/b51875 (cit. on p. 39).

[102] D. Pesquera, X. Marti, V. Holy, R. Bachelet, G. Herranz, and J. Fontcuberta, Appl. Phys. Lett. **99**, 221901 (2011) 10.1063/1.3663574 (cit. on p. 40).

[103] J. S. Kouvel, and C. C. Hartelius, J. Appl. Phys. **33**, 1343 (1962) 10.1063/1.1728721 (cit. on p. 41).

[104] J. S. Kouvel, J. Appl. Phys. **37**, 1257 (1966) 10.1063/1.1708424 (cit. on p. 41).

[105] C. Jiang, Acta Mater. **57**, 4716 (2009) 10.1016/j.actamat.2009.06.026 (cit. on p. 41).

[106] H. T. Stokes, and D. M. Hatch, J. Appl. Crystallogr. **38**, 237 (2005) 10.1107/S0021889804031528 (cit. on p. 44).

[107] H. Rotella, O. Copie, G. Steciuk, H. Ouerdane, P. Boullay, P. Roussel, M. Morales, A. David, A. Pautrat, B. Mercey, L. Lutterotti, D. Chateigner, and W. Prellier, J. Phys. Condens. Matter **27**, 175001 (2015) 10.1088/0953-8984/27/17/175001 (cit. on p. 46).

[108] H. Lipson, J. I. Langford, and H.-C. Hu, in *Int. tables crystallogr.* (International Union of Crystallography, Chester, England, Oct. 2006), pp. 596–598, 10.1107/97809553602060000601 (cit. on p. 47).

[109] M. I. Aroyo, J. M. Perez-Mato, C. Capillas, E. Kroumova, S. Ivantchev, G. Madariaga, A. Kirov, and H. Wondratschek, Zeitschrift für Krist. - Cryst. Mater. **221** (2006) 10.1524/zkri.2006.221.1.15 (cit. on pp. 48, 52).

[110] Z. Nishiyama, *Martensitic transformation*, Materials science and technology series (Academic Pr., New York, 1978), p. 74, ISBN: 0-12-519850-7 (cit. on p. 50).

[111] R. V. Krishnan, and L. C. Brown, Metall. Trans. **4**, 1017 (1973) 10.1007/BF02645604 (cit. on p. 50).

[112] J. Wang, and I. J. Beyerlein, Metall. Mater. Trans. A **43**, 3556 (2012) 10.1007/s11661-012-1177-6 (cit. on p. 54).

[113] G. Gottstein, "Kristallbaufehler", in (Springer Berlin Heidelberg, Berlin, Heidelberg, 2001) Chap. Kristallba, pp. 57–98, 10.1007/978-3-662-22296-6_3 (cit. on p. 54).

[114] T. Braisaz, P. Ruterana, G. Nouet, A. Serra, P. Komminou, T. Kehagias, and T. Karakostas, Philos. Mag. Lett. **74**, 331 (1996) 10.1080/095008396180056 (cit. on p. 55).

[115] J. A. Mydosh, Hyperfine Interact. **31**, 347 (1986) 10.1007/BF02401580 (cit. on p. 59).

[116] W. Kohn, Phys. Rev. Lett. **2**, 393 (1959) 10.1103/PhysRevLett.2.393 (cit. on pp. 63, 137).

[117] Y. Lee, J. Y. Rhee, and B. N. Harmon, Phys. Rev. B **66**, 054424 (2002) 10.1103/PhysRevB.66.054424 (cit. on pp. 63, 116).

[118] C. Bungaro, K. M. Rabe, and A. Dal Corso, Phys. Rev. B **68**, 134104 (2003) 10.1103/PhysRevB.68.134104 (cit. on pp. 63, 116).

[119] P. Entel, V. D. Buchelnikov, M. E. Gruner, A. Hucht, V. V. Khovailo, S. K. Nayak, and A. T. Zayak, Mater. Sci. Forum **583**, 21 (2008) 10.4028/www.scientific.net/MSF.583.21 (cit. on pp. 63, 116).

[120] C. P. Opeil, B. Mihaila, R. K. Schulze, L. Mañosa, A. Planes, W. L. Hults, R. A. Fisher, P. S. Riseborough, P. B. Littlewood, J. L. Smith, and J. C. Lashley, Phys. Rev. Lett. **100**, 165703 (2008) 10.1103/PhysRevLett.100.165703 (cit. on pp. 63, 116).

[121] T. D. Haynes, R. J. Watts, J. Laverock, Z. Major, M. A. Alam, J. W. Taylor, J. A. Duffy, and S. B. Dugdale, New J. Phys. **14**, 035020 (2012) 10.1088/1367-2630/14/3/035020 (cit. on pp. 63, 116).

[122] G. Grimvall, B. Magyari-Köpe, V. Ozoliņš, and K. A. Persson, Rev. Mod. Phys. **84**, 945 (2012) 10.1103/RevModPhys.84.945 (cit. on p. 75).

[123] L. Spieß, G. Teichert, R. Schwarzer, H. Behnken, and C. Genzel, *Moderne Röntgenbeugung* (Vieweg+Teubner, Wiesbaden, 2009), pp. 5–40, 10.1007/978-3-8349-9434-9 (cit. on p. 92).

[124] J. Ayers, S. Ghandhi, and L. Schowalter, J. Cryst. Growth **113**, 430 (1991) 10.1016/0022-0248(91)90077-I (cit. on p. 95).

[125] Y. K. Kim, H. Morioka, R. Ueno, S. Yokoyama, H. Funakubo, K. Lee, and S. Baik, Appl. Phys. Lett. **88**, 252904 (2006) 10.1063/1.2214169 (cit. on p. 95).

[126] K. S. Lee, and S. Baik, J. Appl. Phys. **87**, 8035 (2000) 10.1063/1.373493 (cit. on p. 95).

[127] L. Schowalter, E. Hall, N. Lewis, and Shin Hashimoto, Thin Solid Films **184**, 437 (1990) 10.1016/0040-6090(90)90442-G (cit. on p. 95).

[128] T. Urano, and T. Kanaji, J. Phys. Soc. Japan **57**, 3403 (1988) 10.1143/JPSJ.57.3403 (cit. on p. 97).

[129] C. Martinez Boubeta, J. L. Costa-Kraemer, and A. Cebollada, J. Phys. Condens. Matter **15**, R1123 (2003) 10.1088/0953-8984/15/25/202 (cit. on p. 97).

[130] A. Scherz, H. Wende, P. Poulopoulos, J. Lindner, K. Baberschke, P. Blomquist, R. Wäppling, F. Wilhelm, and N. B. Brookes, Phys. Rev. B **64**, 180407 (2001) 10.1103/PhysRevB.64.180407 (cit. on p. 99).

[131] E. Nordström, B. Kalska, L. Häggström, P. Blomqvist, and R. Wäppling, J. Alloys Compd. **348**, 208 (2003) 10.1016/S0925-8388(02)00835-6 (cit. on p. 99).

[132] A. Scherz, P. Poulopoulos, H. Wende, G. Ceballos, K. Baberschke, and F. Wilhelm, J. Appl. Phys. **91**, 8760 (2002) 10.1063/1.1447206 (cit. on p. 99).

[133] M. Hÿtch, E. Snoeck, and R. Kilaas, Ultramicroscopy **74**, 131 (1998) 10.1016/S0304-3991(98)00035-7 (cit. on p. 106).

[134] K. Uebayashi, H. Shimizu, and H. Yamada, Mater. Trans. **47**, 456 (2006) 10.2320/matertrans.47.456 (cit. on pp. 109, 110).

[135] L. J. Swartzendruber, Bull. Alloy Phase Diagrams **5**, 134 (1984) 10.1007/BF02868944 (cit. on p. 115).

[136] L. J. Swartzendruber, and B. Sundman, Bull. Alloy Phase Diagrams **4**, 155 (1983) 10.1007/BF02884862 (cit. on p. 115).

[137] B. Predel, *Co-Rh (Cobalt-Rhodium)*, edited by O. Madelung, (Springer-Verlag, Berlin/Heidelberg, 1993) Chap. 5C, pp. 1–2, 10.1007/10086082_943 (cit. on p. 115).

[138] M. Venkatraman, and J. P. Neumann, J. Phase Equilibria **8**, 107 (1987) 10.1007/BF02873188 (cit. on p. 115).

[139] H. Béa, B. Dupé, S. Fusil, R. Mattana, E. Jacquet, B. Warot-Fonrose, F. Wilhelm, A. Rogalev, S. Petit, V. Cros, A. Anane, F. Petroff, K. Bouzehouane, G. Geneste, B. Dkhil, S. Lisenkov, I. Ponomareva, L. Bellaiche, M. Bibes, and A. Barthélémy, Phys. Rev. Lett. **102**, 217603 (2009) 10.1103/PhysRevLett.102.217603 (cit. on p. 116).

[140] B. Dupé, I. C. Infante, G. Geneste, P.-E. Janolin, M. Bibes, A. Barthélémy, S. Lisenkov, L. Bellaiche, S. Ravy, and B. Dkhil, Phys. Rev. B **81**, 144128 (2010) 10.1103/PhysRevB.81.144128 (cit. on p. 116).

[141] Y. Liu, K.-K. Wang, L.-H. Ni, Z.-H. Ren, G. Xu, C.-L. Song, and G.-R. Han, Phys. Lett. A **376**, 3303 (2012) 10.1016/j.physleta.2012.07.011 (cit. on p. 116).

[142] R. Niemann, U. K. Rößler, M. E. Gruner, O. Heczko, L. Schultz, and S. Fähler, Adv. Eng. Mater. **14**, 562 (2012) 10.1002/adem.201200058 (cit. on p. 135).

[143] J. Labbé, and J. Friedel, J. Phys. **27**, 153 (1966) 10.1051/jphys:01966002703-4015300 (cit. on p. 135).

[144] M. Gruner, P. Entel, J. Minár, S. Polesya, S. Mankovsky, and H. Ebert, J. Magn. Magn. Mater. **324**, 3524 (2012) 10.1016/j.jmmm.2012.02.081 (cit. on p. 136).

[145] P. J. Brown, A. Y. Bargawi, J. Crangle, K.-U. Neumann, and K. R. A. Ziebeck, J. Phys. Condens. Matter **11**, 4715 (1999) 10.1088/0953-8984/11/24/312 (cit. on p. 136).

[146] M. E. Gruner, W. A. Adeagbo, A. T. Zayak, A. Hucht, and P. Entel, Phys. Rev. B **81**, 064109 (2010) 10.1103/PhysRevB.81.064109 (cit. on p. 137).

[147] K. Tajima, Y. Endoh, Y. Ishikawa, and W. G. Stirling, Phys. Rev. Lett. **37**, 519 (1976) 10.1103/PhysRevLett.37.519 (cit. on p. 137).

[148] B. N. Brockhouse, K. R. Rao, and A. D. B. Woods, Phys. Rev. Lett. **7**, 93 (1961) 10.1103/PhysRevLett.7.93 (cit. on p. 137).

[149] V. Aksenov, Y. Nikitenko, V. Proglyado, M. Andreeva, B. Kalska, L. Häggström, and R. Wäppling, J. Magn. Magn. Mater. **258-259**, 332 (2003) 10.1016/S0304-8853(02)01042-9 (cit. on p. 142).

Appendices

A Supplementary material

A.1 Scientific Background

A.1.1 Band-Jahn-Teller effect and Fermi surface nesting

DFT calculations presented in Chap. 4 identified the triggering mechanism of the strain-induced transformation from the bct to the orthorhombic phase in the electronic structure. A band-Jahn-Teller like effect was proposed. The experimental observation of a specific shuffling of atomic planes during the transition together with the shape of the calculated Fermi surface of the parental bct structure suggests a certain electron-phonon coupling, so-called Fermi surface nesting. These effects that have been linked to structural and martensitic transformations in various metals and metal alloys are briefly introduced in the following. Although both phenomena occur often along with martensitic transformations they do not constitute a necessary condition, as has been pointed out by Niemann *et al.* [142], however they are considered to trigger or initiate the transitions and are sometimes brought in relation with pre-martensitic transformations.

The band-Jahn-Teller effect was initially proposed by Labbé and Friedel to explain a low temperature structural transition in V_3Si [143]. Similar to the normal Jahn-Teller effect it lifts the degeneracy of certain electronic states along with a distortion of the lattice. If these electronic states are located close to or at the E_F, they will shift to energy values above and below the E_F and the total energy of the system will decrease due to the created occupied low energy states. Hence, a crucial prerequisite for the occurrence of a band-Jahn-Teller effect is a high DOS at E_F.

This has been illustratively shown by Opahle *et al.*, who calculated the DOS and electronic band structure for disordered $Fe_{80}Pd_{20}$ in fcc and face-centered-tetragonal (fct) structures [97]. Fig. A.1(a) reprints the spin-resolved total and Fe-partial DOS for both states. The pronounced peak in the minority-spin DOS visible in the fcc phase, originating from Fe $3d$ states, splits in the fct phase and the corresponding electronic states are shifted above and below E_F, effectively reducing total energy and thus stabilizing the distorted fct phase. The spectral density of the minority states is plotted in Fig. A.1(b). A splitting of the band at the Γ point at the E_F

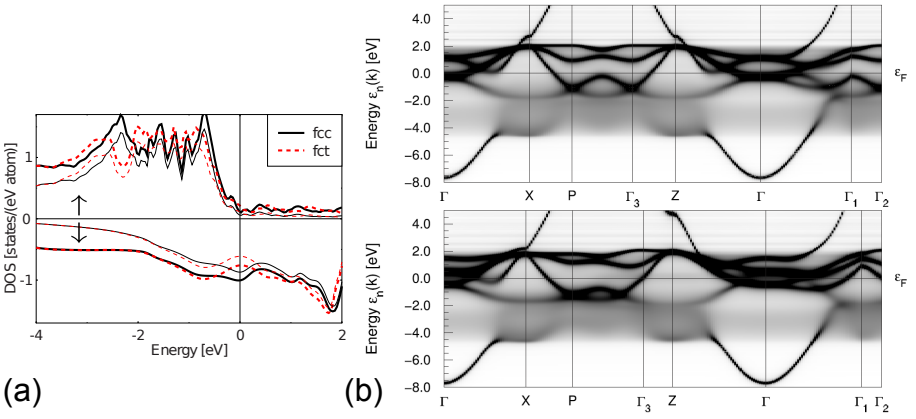

Figure A.1.: Electronic structure of $Fe_{80}Pd_{20}$. (a) Spin-resolved DOS of fcc and fct $Fe_{80}Pd_{20}$. The minority Fe-DOS of the fcc phase presents a peak at the E_F, which is redistributed in the fct phase. (b) Spectral density of the minority states, again for fct (lower panel) and fcc (upper panel). The states situated close to the E_F at the Γ point shift above and below E_F, eventually resulting in a total band energy gain of the system. (*Reprinted with permission from* [97]. ©2009, American Institute of Physics)

level is visible in the fct phase, which illustrates the lifted degeneracy of electronic states in the fcc phase. Similar results were presented by Gruner *et al.*, who showed in addition the dependency of this electronic feature on the elemental composition, influencing the position of E_F but also the shape of the DOS [144]. A similar band-Jahn-Teller mechanism was also identified in the prototype magnetic shape memory alloy Ni_2MnGa [145].

Another phenomenon frequently connected to a peak or maximum in the DOS at the E_F is the so-called Fermi surface nesting. It occurs if the Fermi surface of a metal, hence the surface formed in reciprocal space by the highest occupied electronic states, exhibits large parallel areas which can be connected with one single wave vector, the so-called nesting vector. The large number of states directly at the E_F makes the system susceptible for structural deformation, as a rearrangement of the ionic cores of the lattice may change the charge distribution and the band structure and thus may lead to an energy gain, by shifting unoccupied states up and occupied states down. This displays a sort of electron-lattice coupling, which also affects the dynamics of the lattice. The coupling results in a strong decrease of the phonon energy at a frequency corresponding to the nesting vector (at a certain

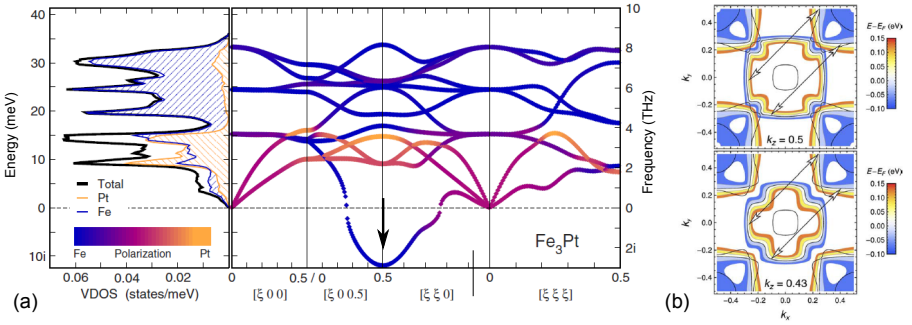

Figure A.2.: Electronic and vibrational properties of $L1_0$ Fe_3Pt. (a) Calculated vibrational-DOS (left panel) and phonon dispersion curves (right panel), the arrow indicates the soft phonon mode at $[\frac{1}{2},\frac{1}{2},0]$. (b) Cross-sections through the Fermi surface at two different positions. The arrows represent the nesting vectors between parallel planes of the Fermi surface. (*Reprinted with permission from* [146]. ©2010, American Physical Society)

temperature), which is referred to as condensation of a soft phonon mode or a soft mode transition, eventually leading to a static distortion of the lattice.

An example is the $L1_0$ ordered Fe_3Pt alloy, which exhibits a soft mode transition below 100 K [147]. Gruner *et al.* conducted a thorough theoretical investigation, calculating vibrational and electronic properties of the system [146]. Fig. A.2(a) presents the calculated phonon dispersion curve, representing the experimentally found softening of the transversal acoustic branch around $[\frac{1}{2},\frac{1}{2},0]$, marked by the arrow. Cross-sections through the Fermi surface in reciprocal space presented in Fig. A.2 (b), show large parallel planes, which can be connected with a nesting vector (arrow), being virtually identical to the wave vector of the phonon anomaly $(\frac{1}{2},\frac{1}{2},0)$. The authors conclude that this electron-phonon coupling is responsible for the soft mode transition and the structural changes in $L1_0$ ordered Fe_3Pt alloy at low temperatures, which is also referred to as a Kohn-anomaly [116, 148].

A.2 Materials and methods

A.2.1 Sputter targets and evaporation materials

The elemental and alloy buffer layer were deposited from commercially available elemental targets, which are listed in Tab. A.1. Due to the good thermal conductivity of the metals and mechanical stability a further bonding was not necessary.

Table A.1.: List of sputter targets employed for the W-V buffer layer deposition. Both targets have a diameter of 76.2 mm (3 ") and a thickness of 6 mm.

material	purity	supplier	part/lot number
W	99.9%	Haines & Maasen	7-1726
V	99.9%	Mateck	0905262

The evaporation materials used in the electron beam evaporators were rods with 3 mm diameter in case of Rh and Fe with natural abundance, both purchased from Goodfellow with 99.9% elemental purity. The use of 3 mm rods instead of 2 mm (as proposed by the manufacturer) offered a longer period of stable evaporation conditions and thus the interval between refilling the sources could be increased. The enriched ^{57}Fe (>95%) was in form of a thin foil purchased from Cyclotron. Small pieces were loaded into an alumina crucible held by a W liner, which was then heated from the side with the electron beam.

A.2.2 MgO substrates

Single crystal MgO substrates of 10x5x0.5 mm^3 dimensions were purchased from SurfaceNet with an epi-polished surface. The substrate surface was oriented parallel to the MgO(001) planes, while the edges of the substrate were parallel to [110] directions. In that way a Reflection High Energy Electron Diffraction (RHEED) pattern of the [100] direction of the bcc metal lattices could be achieved (45° rotation), as the samples were mounted with their long side parallel to the electron beam axis. From each substrate batch several example substrates were checked with Atomic Force Microscopy (AFM) to confirm sufficient surface quality. Additionally one pristine substrate of each was measured in the Superconductive

Quantum Interference Device (SQUID) as reference for the background subtraction in the magnetic measurements. Attempts to obtain cleaner substrates with less magnetic impurities from another supplier were not successful. Also the use of thinner substrates was explored, in order to suppress the spurious magnetic signal. Unfortunately, due to the fragility of the thin substrates this was as well not beneficial. Apart from the annealing in oxygen atmosphere in the system prior to film deposition (see Chao, 3.6.2 on page 29), no other substrate treatment was performed. The substrates were glued to the stainless steel sample holders using conductive silver paste *G3692* from ACHESON, which was found to produce no non-linear magnetic signal in the SQUID. Nevertheless it was removed from the substrate backside as thoroughly as possible.

A.3 Results

A.3.1 Complete set of RSMs

In Chap. 4 already some essential orthorhombic reflections measured in RSMs have been presented together with a complete list of reflections of the $Cmcm$ phase. Fig. A.3 shows the remaining asymmetric reflections, measured in coplanar and non-coplanar geometry.

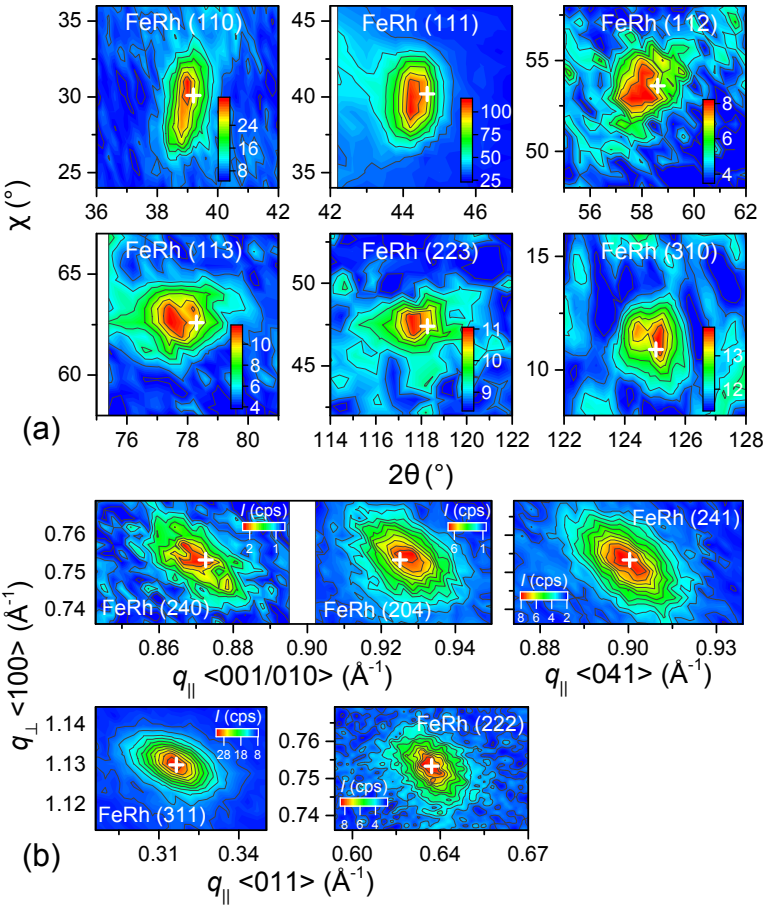

Figure A.3.: RSMs of all measured reflections, which are not shown in the main body of the thesis. (a) Six non-coplanar reflections plotted in χ-2θ space. (b) Five coplanar reflections plotted in reciprocal space along the given directions. The white cross indicates the theoretical position of the reflections.

A.3.2 Thin FeRh films on W-V alloy buffer layers

The initial experiments that investigated the influence of the W-V buffer layer lattice constant on the structural and magnetic properties of the FeRh films were conducted with thinner FeRh films (3 nm), prepared employing the monolayer (ML)-by-ML deposition method II at 300 °C. This was meant to provide good comparability between the samples, owing to the better deposition control. Yet, the occurring and finally understood phase separation behavior was not directly evident from this sample series. However with the help of Mössbauer spectroscopy it was possible to unravel the two-phase state in the samples, which then motivated the more illustrative experiments with the thicker samples. This is briefly discussed in the following.

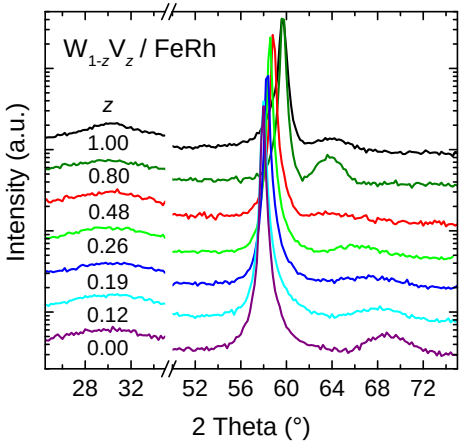

Figure A.4.: HRXRD pattern showing the (002) reflections of the $W_{1-x}V_x$ and FeRh layers. The FeRh reflection is shifting with the change in lattice constant of the buffer layer. For $0.2 \leq x \geq 0.5$ the FeRh reflection broadens extensively.

Figure A.4 shows the High-Resolution X-ray Diffraction (HRXRD) patterns of the bilayer samples deposited on buffer layers from pure W to pure V. The phase separation smears out the reflections to an extent that they cannot be clearly identified in the intermediate lattice constant region, due to the phase separation and the low thickness of the films. Yet the *in situ* growth monitoring with RHEED (not shown) yielded for all samples a well-defined streak pattern, which is evidence for epitaxial growth and represented on the first view a contradiction. The reflection then reappears at even smaller in-plane lattice constants ($y = 0.80$). For the

thin film deposited on pure V again a broadening is observed, which is related to interdiffusion [149] of both layers, owing to the elevated deposition temperature.

Results of the investigation with magnetometry are presented in Fig. A.5: (a) Field Cooling (FC) curves measured in an applied magnetic field $\mu_0 H$ of 50 mT and (b) hysteresis measurements as function of the magnetic field at 30 K. Both measurements show a continuous increase of the magnetization values, with increasing V content, leading to the initial conclusion that the saturation magnetization of the material is changing with strain. The FeRh/V bilayer sample shows again a reduced magnetization, possibly due to the intermixing and alloying with the underlying V layer.

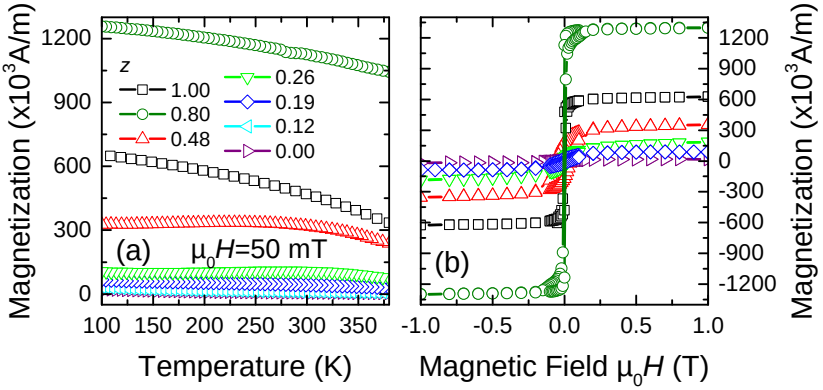

Figure A.5.: Magnetic characterization with SQUID magnetometry. (a) Field-cooling curves measured in a constant magnetic field $\mu_0 H = 50$ mT in a temperature range 380 - 100 K. (b) Hysteresis measurements $M(\mu_0 H)$ at 30 K. The legend in (a) applies for both graphs.

Further insights into the structural and magnetic state of a FeRh thin film in the transition region ($z = 0.66$) can be obtained by ^{57}Fe conversion Mössbauer spectroscopy which is presented in Fig. A.6. The spectrum measured at RT can be represented with a singlet only and does not show evidence for a six-line magnetic splitting. This is in contradiction to the above presented FC-curves that feature a non-zero magnetization at RT. However, one needs to keep in mind that CEMS is a zero-field method, while in the above SQUID measurement a sizable external field is applied. Therefore ZFC-FC curves were measured in a small field of $\mu_0 H = 5$ mT, shown in the inset. The data clearly depict the features of superparamagnetic behavior with a blocking temperature of ≈ 150 K and a distinctly reduced magnetization at RT. Hence, in zero-field and at RT the fluctuation of the magnetic clusters in the

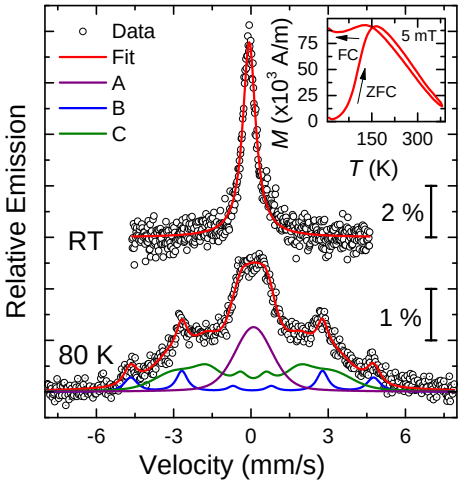

Figure A.6.: CEMS investigation of a 3 nm ^{57}FeRh thin film on a $W_{0.66}V_{0.34}$ buffer at RT and at 80 K. The RT spectrum is fitted with a quadrupole doublet only. The 80 K spectrum reveals magnetic splitting. In addition to the doublet A, two sextets B and C are needed to represent the data. Please, see text for details. The inset shows a ZFC/FC measurement in $\mu_0 H = 5$ mT, proving the superparamagnetic nature of the observed magnetism.

film are faster then the characteristic time of the Mössbauer measurement, which results in the observation of the dynamic singlet spectrum.

The spectrum measured at 80 K, so below the blocking temperature, is presented in the lower part of the graph. Here, additional to the single line, a magnetic splitting is observed. The spectrum can be reproduced with three subcomponents: **A** is a singlet which represents parts of the sample which are not magnetically ordered. **B** is a relatively narrow and defined sextet with a magnetic hyperfine field $B_{\mathrm{HF}} = 29$ T corresponding to partially ordered equiatomic FeRh [13]. **C** is a very broad magnetic sextet, which can be most probably attributed to magnetic clusters that are still fluctuating on the timescale of the measurement at 80 K. This result represents first evidence for a two-phase state in the FeRh thin films, which was then underpinned and proven by the combined diffraction and spectroscopy experiments carried out for thicker FeRh layer that are presented in the main body of the thesis (Chap. 7.2).

However, two additional and important conclusions can be drawn from this initial sample series. First, it shows that the spontaneous phase separation is not a function

of the film thickness, but rather a stress relaxation mechanism that happens from the bottom of the FeRh film acting throughout the thickness in support of the HRTEM results in Chap. 7.2. Second, the evolution of the ratio magnetic phase with the decreasing in-plane lattice constant illustrates that the phase-ratio can be controlled with the in-plane lattice spacing. This is finally summarized in the main body of the thesis Fig. 7.12 on page 109 where the results of both sample series are plotted together. The continuous increase of the average magnetization with decreasing lattice constant clearly shows the relation for both thickness regimes.

B Personal data

B.1 Curriculum vitae (Lebenslauf)

Name:	Ralf Witte
Geburtsdatum:	14.03.1984
Geburtsort:	Ludwigsburg

Schulbildung

27. Juni 2003	Goethe Gymnasium Ludwigsburg, Allgemeine Hochschulreife

Studium

Oktober 2004 – Juli 2010	Studium der Materialwissenschaft, Technische Universität Darmstadt (TUD), Diplomarbeit am Institut für Nanotechnolgie (INT) am Karlsruher Institut für Technologie (KIT): Magnetic phenomena in Fe-Sc nanoglasses
September 2007 – August 2008	Erasmus Aufenthalt: Ecole Centrale de Lyon, Frankreich Diplôme d'Etudes Supérieures d'Option, Option: Micro-Nano-Biotechnologie
Januar 2011 – Juni 2016	Promotionsstudent an der TUD, Fachbereich Material- und Geowissenschaften

Berufstätigkeit

November 2010 – November 2013	Wissenschaftlicher Mitarbeiter im Gemeinschaftslabor Nanomaterialien TUD/KIT
November 2013 –	Wissenschaftlicher Mitarbeiter am INT/KIT

B.2 Publications

B.2.1 Journal articles

* Publications relevant to this thesis.

14. *Tailoring magnetic frustration in strained epitaxial FeRh films
R. Witte, R. Kruk, M. E. Gruner, R. A. Brand, D. Wang, S. Schlabach, A. Beck, V. Provenzano, R. Pentcheva, H. Wende, and H. Hahn, *Physical Review B* **93**, 104416, 10.1103/PhysRevB.93.104416 (2016).

13. Development of a water based process for stable conversion cathodes on the basis of FeF_3
A. H. Pohl, M. Faraz, A. Schröder, M. Baunach, W. Schabel, A. Guda, V. Shapovalov, A. Soldatov, V. S. K. Chakravadhanula, C. Kübel, R. Witte, H. Hahn, T. Diemant, R. J. Behm, H. Emerich, and M. Fichtner, *Journal of Power Sources* **313**, 213, 10.1016/j.jpowsour.2016.02.080 (2016).

12. Synthesis, structural characterisation and proton conduction of two new hydrated phases of barium ferrite $BaFeO_{2.5-x}(OH)_{2x}$
P. L. Knöchel, P. J. Keenan, C. Loho, C. Reitz, R. Witte, K. S. Knight, A. J. Wright, H. Hahn, P. R. Slater, and O. Clemens, *Journal of Materials Chemistry A* **4**, 3415, 10.1039/C5TA06383C (2016).

11. Identifying the redox activity of cation-disordered Li–Fe–V–Ti oxide cathodes for Li-ion batteries
R. Chen, R. Witte, R. Heinzmann, S. Ren, S. Mangold, H. Hahn, R. Hempelmann, H. Ehrenberg, and S. Indris, *Physical Chemistry Chemical Physics* **18**, 7695, 10.1039/C6CP00131A (2016).

10. Mechanical Milling Assisted Synthesis and Electrochemical Performance of High Capacity $LiFeBO_3$ for Lithium Batteries
M. A. Cambaz, M. A. Reddy, B. P. Vinayan, R. Witte, A. H. Pohl, X. Mu, V. S. K. Chakravadhanula, C. Kübel, and M. Fichtner, *ACS Applied Materials & Interfaces* **8**, 2166, 10.1021/acsami.5b10747 (2016).

9. Electric field-controlled magnetization switching in Co/Pt thin-film ferromagnets
A. Siddique, S. Gu, R. Witte, M. Ghahremani, C. A. Nwokoye, A. Aslani, R. Kruk, V. Provenzano, L. H. Bennett, and E. Della Torre, *Cogent Physics* **3**, 1139435, 10.1080/23311940.2016.1139435 (2016).

8. Nanoscale spinel $LiFeTiO_4$ for intercalation pseudocapacitive Li^+ storage
R. Chen, M. Knapp, M. Yavuz, S. Ren, R. Witte, R. Heinzmann, H. Hahn, H. Ehrenberg, and S. Indris, *Physical Chemistry Chemical Physics* **17**, 1482, 10.1039/C4CP04655B (2015).

7. *Ion-irradiation-assisted tuning of phase transformations and physical properties in single crystalline Fe_7Pd_3 ferromagnetic shape memory alloy thin films
A. Arabi-Hashemi, R. Witte, A. Lotnyk, R. A. Brand, A. Setzer, P. Esquinazi, H. Hahn, R. S. Averback, and S. G. Mayr, *New Journal of Physics* **17**, 053029, 10.1088/1367-2630/17/5/053029 (2015).

6. Crystallographic and Magnetic Structure of the Perovskite-Type Compound $BaFeO_{2.5}$: Unrivaled Complexity in Oxygen Vacancy Ordering
O. Clemens, M. Gröting, R. Witte, J. M. Perez-Mato, C. Loho, F. J. Berry, R. Kruk, K. S. Knight, A. J. Wright, H. Hahn, and P. R. Slater, *Inorganic Chemistry* **53**, 5911, 10.1021/ic402988y (2014).

5. Oxidation state and local structure of a high-capacity $LiF/Fe(V_2O_5)$ conversion cathode for Li-ion batteries
A. H. Pohl, A. A. Guda, V. V. Shapovalov, R. Witte, B. Das, F. Scheiba, J. Rothe, A. V. Soldatov, and M. Fichtner, *Acta Materialia* **68**, 179, 10.1016/j.actamat.2014.01.016 (2014).

4. The mechanically induced structural disorder in barium hexaferrite, $BaFe_{12}O_{19}$, and its impact on magnetism
V. Šepelák, M. Myndyk, R. Witte, J. Röder, D. Menzel, R. H. Schuster, H. Hahn, P. Heitjans, and K.-D. Becker, *Faraday Discussions* **113**, 033913, 10.1039/C3FD00137G (2014).

3. Evidence for enhanced ferromagnetism in an iron-based nanoglass
R. Witte, T. Feng, J. X. Fang, A. Fischer, M. Ghafari, R. Kruk, R. A. Brand, D. Wang, H. Hahn, and H. Gleiter, *Applied Physics Letters* **103**, 073106, 10.1063/1.4818493 (2013).

2. A novel Ti-based nanoglass composite with submicron– nanometer-sized hierarchical structures to modulate osteoblast behaviors
N. Chen, X. Shi, R. Witte, K. S. Nakayama, K. Ohmura, H. Wu, A. Takeuchi, H. Hahn, M. Esashi, H. Gleiter, A. Inoue, and D. V. Louzguine, *Journal of Materials Chemistry B* **1**, 2568, 10.1039/c3tb20153h (2013).

1. Structural investigations of interfaces in $Fe_{90}Sc_{10}$ nanoglasses using high-energy x-ray diffraction
   M. Ghafari, S. Kohara, H. Hahn, H. Gleiter, T. Feng, R. Witte, and S. Kamali, *Applied Physics Letters* **100**, 133111, 10.1063/1.3699228 (2012).

Publications in preparation

*Epitaxial strain-engineered self-assembly of magnetic nanostructures in FeRh thin films
R. Witte, R. Kruk, A. Molinari, D. Wang, S. Schlabach, R. A. Brand, V. Provenzano, and H. Hahn.

*Compositional limit of the strain-induced martensitic transformation in epitaxial FeRh thin films
R. Witte, R. Kruk, M. E. Gruner, R. A. Brand, H. Wende, and H. Hahn.

B.2.2 Conference contributions

* Presenting author

Magnetic and structural properties of epitaxial FeRh films on various metallic underlayers studied by CEMS
R. Witte, R. A. Brand*, R. Kruk, and H. Hahn, 33rd International Conference on the Applications of the Mössbauer Effect (ICAME), September 13–18, 2015, *Hamburg*.

Synthesis and properties of ultrathin B2 ordered FeRh films
R. Witte*, R. A. Brand, R. Kruk, and H. Hahn, Frühjahrstagung DPG, Sektion Kondensierte Materie, Fachverband Magnetismus, March 30–April 4, 2014, *Dresden*.

Synthesis and properties of ultrathin, epitaxial, B2 ordered FeRh thin films
R. Witte*, R. A. Brand, R. Kruk, and H. Hahn, 5th Seeheim Conference on Magnetism (SCM2013), September 29th – October 3rd, 2013, *Frankfurt*

Mössbauer studies of nanocrystalline and nonequilibrium ferrites
V. Šepelák*, R. Witte, M. Ghafari, H. Hahn, and K. D. Becker, 32nd International Conference on the Applications of the Mössbauer Effect (ICAME), September 1–6, 2013, *Opatija, Croatia*.

Synthesis and properties of ultrathin, epitaxial, B2 ordered FeRh thin films
R. Witte*, R. A. Brand, R. Kruk, and H. Hahn, Frühjahrstagung DPG, Sektion Kondensierte Materie, Fachverband Magnetismus, March 10–15, 2013, *Regensburg*.

Enhanced ferromagnetism in $Fe_{90}Sc_{10}$ nanoglass studied by Mössbauer spectroscopy
R. Witte*, T. Feng, M. Ghafari, R. Kruk, R. A. Brand, H. Gleiter, and H. Hahn, Workshop on Structure and Properties of Nonequilibrium and Nanocrystalline Materials, February 12–March 2, 2013, *Stara Lesna, Slovakia*.

Enhanced magnetism in a nanostructured metallic glass
R. Witte*, T. Feng, M. Ghafari, R. Kruk, R. A. Brand, H. Gleiter, and H. Hahn, Material Science and Engineering (MSE), September 25–27, 2012, *Darmstadt*.

Enhanced Ferromagnetism in Nanometallic Glass studied by Mössbauer spectroscopy
R. Witte*, T. Feng, M. Ghafari, R. Kruk, R. A. Brand, H. Gleiter, and H. Hahn, Frühjahrstagung DPG, Sektion Kondensierte Materie, Fachverband Metalphysik, March 25–30, 2012, *Berlin*.

Room temperature ferromagnetism in amorphous $Fe_{90}Sc_{10}$ investigated by ^{57}Fe Mössbauer spectroscopy
R. Witte*, J. Fang, M. Ghafari, R. Kruk, R. A. Brand, H. Hahn, and H. Gleiter, 7$^{\text{th}}$ Seeheim Workshop on Mössbauer Spectroscopy, June 13–17, 2011, *Frankfurt*.

$Fe_{90}Sc_{10}$ Nanoglass investigated by ^{57}Fe Mössbauer spectroscopy
R. Witte, M. Ghafari*, R. Kruk, R. A. Brand, H. Hahn, and H. Gleiter, 31$^{\text{st}}$ International Conference on the Applications of the Mössbauer Effect (ICAME), September 22–25, 2011, *Tokyo, Japan*.

Magnetic properties of $Fe_{90}Sc_{10}$ nanoglass
R. Witte*, J. Fang, M. Ghafari, R. Kruk, R. A. Brand, H. Hahn, and H. Gleiter, European Congress and Exhibition on Advanced Materials and Processes (Euromat), September 12–15, 2011, *Montpellier, France*

Magnetic properties of $Fe_{90}Sc_{10}$ nanoglass
R. Witte*, J. Fang, M. Ghafari, R. Kruk, R. A. Brand, H. Hahn, and H. Gleiter, Frühjahrstagung der Deutschen Physikalischen Gesellschaft, Fachverband Magnetismus, March 13–18, 2011, *Dresden*.

Acknowledgments

I would like to thank everybody who directly contributed to the success of my doctoral thesis and likewise everyone who supported me throughout my doctorate.

I am grateful to my thesis supervisor Horst Hahn for his confidence in me and my scientific work. He was always interested in any scientific problem that needed discussion and his guidance and experience were of true importance for the progress and final success of my work.

I thank Heiko Wende for kindly taking over the position of Co-referee for my dissertation.

Robert Kruk was a constantly present scientific mentor, who guided and supported me from the early days of leak-testing to the most complicated scientific problems. Together we discussed and understood many scientific issues, well, nature was more consistent than we thought.

I owe much to Richard Brand, it was most reassuring to have his expert knowledge in Mössbauer spectroscopy and magnetism always at hand. His deep comprehension of physics and his ability to contribute to every scientific discussion is an example for me.

I benefited often from the support offered by my colleagues in the Hahn group, which I highly appreciate. Especially the members of the tunable materials group: Arne Fischer, who introduced me to the many aspects of practical (UHV)-lab work and CAD drawing. The numerous scientific and technical discussions with him were always helpful and the working atmosphere we had in both our lab and office was constantly good. Philipp Leufke who explained me many things already during my diploma thesis, and who showed, as senior PhD student, constant interest in my progress. His Latex document will be valuable for many PhD students to come. Christian Reitz, was always willing to venture into a heated discussion about the details of a scientific problem, moreover he kept alive our SQUID magnetometer. Alan Molinari, introduced me to the magnetron sputtering device and together we deposited the first refractory metal buffer layers. I thank Martin Limbach for his valuable assistance with setting up the new Mini-MBE system. Vladimir Šepelák was constantly interested in my work and encouraged and supported me to participate at several conferences and workshops.

I am very thankful for the administrative support from Birgit Limmer and Renate Hernichel.

I acknowledge the critical proof-reading of the manuscript by Richard Brand, Robert Kruk, Christian Reitz and Wolfram Witte.

The TEM group at the INT, Sabine Schlabach, Di Wang, Houari Amari, Torsten Scherer and Christian Kübel contributed significantly to the success of my work, their effort is highly appreciated.

I acknowledge the services of André Beck, who performed RBS measurements at the Institute of Solid State Physics at KIT.

I would like to thank my collaborators from the University of Duisburg-Essen for fruitful discussions, Rossitza Pentcheva, Petel Entel, Werner Keune and especially Heiko Wende and Markus Gruner, who both showed immediate interest in my results about the strained FeRh films. Markus Gruners DFT calculations and expertise was most helpful in understanding the structural relaxation processes taking place in my samples. I acknowledge the measurement of low temperature CEMS data expertly performed by Ulrich v. Hörsten.

I acknowledge the discussions with our collaborators at George Washington University, Edward Della Torre, Lawrence Bennett and Virgil Provenzano. Virgils continuous interest in my progress and his hands on support during his frequent visits at INT was always encouraging.

Financial support from the DFG via Contract No. HA1344/28-1 is gratefully acknowledged.

The encouragement of my entire family during my doctorate was invaluable and motivated me to finally complete it. I am most grateful to Carmen for her constant moral support and her confidence in me whenever I needed it most.